

Scaling, stability range, magnetic excitations and light-induced effects in Cu_2OSeO_3

Author:

Sauceda Flores, Jorge

Publication Date:

2022

DOI:

<https://doi.org/10.26190/unsworks/24137>

License:

<https://creativecommons.org/licenses/by/4.0/>

Link to license to see what you are allowed to do with this resource.

Downloaded from <http://hdl.handle.net/1959.4/100430> in <https://unsworks.unsw.edu.au> on 2024-05-05



UNSW
SYDNEY

**Scaling, stability range, magnetic excitations and
light-induced effects in Cu_2OSeO_3**

JORGE ARTURO SAUCEDA FLORES

A thesis submitted in fulfilment of the requirements
for the degree of Doctor of Philosophy

School of Physics, Faculty of Science
The University of New South Wales

January 2022

Scaling, stability range, magnetic excitations and
light-induced effects in Cu_2OSeO_3

JORGE ARTURO SAUCEDA FLORES

born in Tegucigalpa, Honduras

Supervisor: A/Prof. Clemens Ulrich

Co-supervisors: Prof. Jan Seidel

Dr. Oleg Tretiakov

Prof. Tilo Soehnel

Submitted in Sydney, Australia (31.01.2022)

Abstract

The delicate energetic balance between the competing symmetric and asymmetric magnetic interactions found in magnetic skyrmion materials provides an interesting framework to investigate the fundamental properties of novel spin textures and the potential technological applications of topological spin vortices. The projects in this thesis take advantage of a set of complementary techniques, namely, elastic magnetic neutron scattering, inelastic photon scattering and SQUID magnetisation, that enable us to investigate the effect of changes in the atomic lattice and external stimuli upon correlated electron systems such as the multiferroic skyrmion material Cu_2OSeO_3 .

Small angle neutron scattering has been extensively used to investigate the emergence of magnetic skyrmion long range magnetic ordering in different materials since the distance between these magnetic vortices usually lies between 10 and 200 nm, which is within the resolution of this technique. Moreover, the reciprocal space resolution and intense neutron flux of the state-of-the-art small angle neutron scattering instruments at the Australian Centre for Neutron Scattering has proved to be comparable to the best neutron instruments around the world and sensitive to small variations in magnetic neutron scattering patterns from small single crystals. Additionally, the Raman scattering setup at the Ulrich laboratories in the School of Physics of UNSW allows us to investigate the spin dynamics of small samples under different sample environments with excellent energy resolution.

Furthermore, the extensive sample growth and characterisation experience of our collaborators in the Tilo Soehnel group at the University of Auckland has enabled us to investigate the role of different thermal protocols, sample orientations, and light illumination on the stability of the long-range magnetic ordering of pristine and atomically substituted single crystals of Cu_2OSeO_3 . The combined projects have unveiled the role of thermal fluctuations, magnetic anisotropies, thermal protocols, and internal pressure in the transition from non-topological to topological spin states of matter.

Table of Contents

Abstract	i
List of Abbreviations	vii
List of Figures	ix
List of Tables	xiv
Acknowledgements	xvii
Originality, copyright and authenticity	xix
Inclusion of Publications	xxi
1 Background	1
1.1 Introduction to magnetic skyrmions	1
1.1.1 What is a skyrmion?	1
1.1.2 Magnetic interactions	4
1.1.3 Quantum topological effects	8
1.2 The material: Cu_2OSeO_3	10
1.2.1 Cu_2OSeO_3 : A Multiferroic Transition Metal Oxide	10
1.2.2 Crystal structure	12
1.2.3 Magnetic phases	13

1.2.4	Lorentz Imaging in Cu_2OSeO_3	14
1.2.5	Latest developments	15
1.3	Stabilisation of magnetic skyrmion lattices	19
1.3.1	Classical and topological phase transitions	20
1.4	Potential applications of Magnetic Skyrmions	23
1.4.1	Skyrmion racetrack memories	24
1.4.2	Skyrmion logic devices	25
1.4.3	Skyrmion magnonic and radio-frequency devices	26
2	Experimental methods	27
2.1	Sample preparation	27
2.1.1	Sample characterisation	29
2.2	Neutrons scattering	31
2.2.1	Neutron sources	31
2.2.2	Neutron detectors	33
2.2.3	Neutron optics	33
2.2.4	Nuclear and magnetic scattering of neutrons	35
2.2.5	QUOKKA: the Small Angle Neutron Scattering instrument	45
2.3	Sample alignment	49
2.4	Raman scattering	52
2.4.1	Raman scattering theory: Semi-classical approach	52
2.4.2	Quantum mechanical approach	55
2.5	Experimental setup	58
2.6	SQUID magnetometry	60
2.6.1	SQUID magnetisation in skyrmion systems	60
3	Scaling behaviour and stability of skyrmions in Cu_2OSeO_3	63
3.1	Data collection, reduction and analysis protocols	63
3.2	Randomly orientated Cu_2OSeO_3	66
3.3	Axially orientated Cu_2OSeO_3	76
3.3.1	$\langle 100 \rangle$ sample orientation	76
3.3.2	$\langle 110 \rangle$ sample orientation	87
3.4	Conclusions	92

4	Light induced effects, tellurium doping, and magnetic stability	93
4.1	Light-induced magnetic effects in Cu_2OSeO_3	93
4.2	SANS on tellurium-doped Cu_2OSeO_3	103
4.3	Time evolution of skyrmions and spin helices	108
4.4	Conclusions	116
5	Raman scattering in Cu_2OSeO_3	119
5.1	Precedents	119
5.2	Experimental results and discussion	123
5.3	Conclusions	131
5.4	Perspective of future experiments	132
	Bibliography	133

List of Abbreviations

AC	Alternating Current
ACNS	Australian Centre for Neutron Science
AFM	Antiferromagnetic
ANSTO	Australian Nuclear Science and Technology Organisation
BNL	Brookhaven National Laboratories
CCD	Charged Coupled Device
CMR	Colossal Magnetoresistance
CVT	Chemical Vapour Transport
DC	Direct Current
DMI	Dzyaloshinskii-Moriya interaction
EDX	Energy Dispersive X-ray Spectroscopy
FC	Field Cooling
FH	Field Heating
FM	Ferromagnetic
FWHM	Full Width at Half Maximum
HDF	Hierarchical Data Format
HTSC	High Temperature Superconductor
HWHM	Half Width at Half Maximum
HZB	Helmholtz-Zentrum Berlin
ILL	Institute Laue-Langevin
INS	Inelastic Neutron Scattering

KTHNY	Kosterlitz, Thouless, Halperin, Nelson and Young
Matlab [®]	Matrix Laboratory (registered trademark)
MPI	Max Planck Institute
MPMS	Magnetic Property Measurement System
NIST	National Institute of Standards and Technology
OPAL	Open Pool Australian Lightwater reactor
PM	Paramagnetic
PSI	Paul Scherrer Institute
QPT	Quantum Phase Transition
RKKY	Ruderman, Kittel, Kasuya, and Yosida interaction
SANS	Small Angle Neutron Scattering
SAXS	Small Angle X-ray Scattering
SICS	SINQ Instrument Control Software
SkL	Skyrmion lattice
SOC	Spin-Orbit Coupling
SQUID	Superconducting Quantum Interference Device
TEM	Transmission Electron Microscopy
TMO	Transition Metal Oxide
USANS	Ultra-Small Angle Neutron Scattering
VSM	Vibrating Sample Magnetometer
XRD	X-Rays Diffraction
ZFC	Zero Field Cooling
ZFH	Zero Field Heating

List of Figures

1.1	Illustration of a single spherical skyrmion and a skyrmion lattice	2
1.2	Illustration of 2D Néel- and Bloch-type skyrmions	4
1.3	Schematic representation of direct, indirect and RKKY interactions	6
1.4	Illustration of the double exchange magnetic interaction	6
1.5	Schematic representation of the Dzyaloshinskii Moriya interaction	8
1.6	The topological Hall effect and its relation with magnetic skyrmions	10
1.7	Crystallographic unit cell of Cu_2OSeO_3	12
1.8	Magnetic phase diagram of bulk and thin film Cu_2OSeO_3	13
1.9	Lorentz TEM detection of skyrmions in thin Cu_2OSeO_3	15
1.10	Relative rotations of the skyrmion lattice in different regions of the magnetic phase diagram of Cu_2OSeO_3	17
1.11	Stability of low-temperature skyrmions in the phase diagram of Cu_2OSeO_3	18
1.12	The order parameter in first- and second-order phase transitions	21
1.13	Diagram of a skyrmion-based racetrack memory	24
1.14	Concept of a skyrmion-based transistor in a ferromagnetic track	25
1.15	Concept of skyrmion based spintronic devices	26
2.1	Illustration of the Chemical Vapour Transport principle	28
2.2	Neutron Laue diffraction on single crystal Cu_2OSeO_3 as a proof of crystallographic symmetry and alignment	30

2.3	Geometry of the setup of a neutron beam, sample and detector . . .	35
2.4	Diagram of neutron scattering from a fixed nucleus	36
2.5	First small angle neutron scattering observation of skyrmions . . .	38
2.6	The instrument QUOKKA at ANSTO	46
2.7	Example of the result of reducing raw neutron data using cus- tom annular and radial integration protocols in Igor Pro with the ANSTO macros enabled	48
2.8	Setup of the neutron Laue instrument JOEY at ANSTO	49
2.9	Example of neutron Laue Bragg peak indexing with Orient Express	51
2.10	Typical Raman spectrum with Stokes and Anti-Stokes modes	54
2.11	Temperature dependence in the anharmonic decay model	57
2.12	Evolution of the Fano profile with q	58
2.13	Raman setup at the School of Physics UNSW	59
2.14	AC magnetisation of Cu_2OSeO_3 as a tool to determine the critical field value for magnetic phase transitions	61
2.15	AC magnetisation hallmark of the skyrmion phases of Cu_2OSeO_3 .	62
3.1	Example of detector mask used for neutron data analysis	64
3.2	Sample holder and thermal protocols used at the instrument QUOKKA at ANSTO	66
3.3	Neutron Laue diffraction of randomly orientated Cu_2OSeO_3 at room temperature	67
3.4	Selected reduced SANS diffraction patterns from randomly orien- tated Cu_2OSeO_3 in different magnetic phases	68
3.5	Lorentz TEM images of the spin-helical and skyrmion phases of Cu_2OSeO_3 measured by our collaborators at Brookhaven National Laboratories	70
3.6	Magnetic phase diagram of randomly orientated Cu_2OSeO_3 from SANS	70
3.7	Scattering intensity and scattering vector of selected temperature scans from randomly orientated Cu_2OSeO_3	71
3.8	Scattering intensity and scattering vector of selected field scans from randomly orientated Cu_2OSeO_3	72

3.9	Magnetic phase diagram from second randomly orientation of Cu_2OSeO_3	74
3.10	Selected temperature scans at constant field from second random orientation of Cu_2OSeO_3	75
3.11	Selected field scans at constant temperature from second random orientation of Cu_2OSeO_3	75
3.12	Selected SANS diffraction patterns from Zero Field Cooled $\langle 100 \rangle$ -aligned Cu_2OSeO_3	76
3.13	ZFC Magnetic phase diagrams and $ \vec{Q} $ for Cu_2OSeO_3 along $\langle 100 \rangle$.	78
3.14	Selected SANS patterns from Field Cooled $\langle 100 \rangle$ -aligned Cu_2OSeO_3	79
3.15	ZFC vs FC magnetic phase diagrams and $ \vec{Q} $ for Cu_2OSeO_3 along $\langle 100 \rangle$	80
3.16	Temperature dependence of the SANS spectra of Cu_2OSeO_3 at fixed magnetic fields along $\langle 100 \rangle$	82
3.17	Temperature dependence of the intensity of higher-order Bragg peaks from Cu_2OSeO_3 along $\langle 100 \rangle$	85
3.18	Temperature dependence of the $ \vec{Q} $ magnitude of higher-order Bragg peaks from Cu_2OSeO_3 along $\langle 100 \rangle$	86
3.19	Selected SANS patterns from ZFC and FC Temperature scans on $\langle 110 \rangle$ -aligned Cu_2OSeO_3	88
3.20	Selected SANS patterns from FC/FH Field scans on $\langle 110 \rangle$ -aligned Cu_2OSeO_3	89
3.21	FC Magnetic phase diagram and $ Q $ for $\langle 110 \rangle$ -orientated Cu_2OSeO_3	90
3.22	Temperature dependence of the SANS spectra of Cu_2OSeO_3 at fixed magnetic fields along $\langle 110 \rangle$	91
4.1	Optical setup used in our SANS experiments	95
4.2	Normalised light spectra used in our SANS experiments	97
4.3	Magnetic phase diagrams and $ \vec{Q} $ from our SANS experiments performed with and without white light illumination	98
4.4	Wavelength effect on the scattering intensity and $ \vec{Q} $ from selected temperature scans	100

4.5	Wavelength effect on the scattering intensity and $ \vec{Q} $ at fixed temperature and field	101
4.6	Effect of changing light intensity on the scattering intensity and $ \vec{Q} $ at fixed temperature and field	102
4.7	Magnetic phase diagrams of Te-doped Cu_2OSeO_3 single crystals from SANS measured upon ZFC/FH	106
4.8	Contour plots of the scattering vector of the magnetic Bragg peaks from Te-doped Cu_2OSeO_3 single crystals observed through SANS upon ZFC/FH	107
4.9	Time evolution of the SANS spectra from orientated Cu_2OSeO_3 at $T = 55.6$ K and $H = 20$ mT	109
4.10	Time evolution of the SANS spectra from orientated Cu_2OSeO_3 at $T = 55.0$ K and $H = 20$ mT	112
4.11	Time evolution of the SANS spectra from orientated Cu_2OSeO_3 at $T = 56.3$ K and $H = 20$ mT	112
4.12	Arrhenius plot of the skyrmion time-effects in Cu_2OSeO_3 as a function of temperature	114
4.13	Arrhenius plot of the skyrmion time-effects in Cu_2OSeO_3 as a function of magnetic field	115
5.1	First Raman spectrum of Cu_2OSeO_3	121
5.2	Dispersion relation of the magnetic excitations of Cu_2OSeO_3 in the helical phase from its INS spectrum	122
5.3	Raman scattering from selected doping levels of $\text{Cu}_2\text{OSe}_{1-x}\text{Te}_x\text{O}_3$ single crystals at a constant temperature of 85 K	125
5.4	Selected Raman scattering of pristine Cu_2OSeO_3 at different temperatures	126
5.5	Raman spectrum of 5 % Te-doped Cu_2OSeO_3 at selected temperatures	127
5.6	Raman spectrum of 10 % Te-doped Cu_2OSeO_3 at selected temperatures	128
5.7	Temperature dependence analysis of the 428.4 cm^{-1} magnon line in Te-doped Cu_2OSeO_3	129

5.8	Temperature dependence analysis of the 291.1 cm^{-1} phonon line in Te-doped Cu_2OSeO_3	130
5.9	Temperature dependence analysis of the 587.9 cm^{-1} phonon line in Te-doped Cu_2OSeO_3	131

List of Tables

1.1	Comparison of skyrmion lattices in different materials	3
2.1	Parameters of the unit cell of Cu_2OSeO_3 in our samples and in the literature	29
2.2	Energy requirements for scattering with elementary particles	31
2.3	Example parameters to build SANS data reduction protocols in Igor	47
4.1	Parameters and integrated power of the light spectra used in our SANS experiments	96
4.2	Lattice parameters of the Te-doped Cu_2OSeO_3 series used in our experiments	104
5.1	Effective Te-content of the $\text{Cu}_2\text{OSe}_{1-x}\text{Te}_x\text{O}_3$ single crystals from Raman scattering	124

Acknowledgements

I hereby thank my supervisors and colleagues at the University of New South Wales: Clemens Ulrich, Oleg Tretiakov, Jan Seidel, Samuel Yick, Firoz Pervez, Joel O'Brien; at the University of Auckland: Tilo Soehnel, Rosanna Rov, Luis Camacho, Martin Spasovski; and at ANSTO: Elliot Gilbert and Norman Booth. Their scientific support and guidance were crucial throughout this doctoral thesis project.

In particular, this project depended on the high-quality samples grown by Rosanna Rov and Luis Camacho at the University of Auckland under the supervision of Tilo Soehnel, and the active participation of Rosanna Rov and Martin Spasovski in the data acquisition process during most of the neutron experiments reported in this thesis.

I must also mention my dearly-beloved relatives and friends in Honduras, Brazil, Spain and Germany; the community at Warrane College UNSW: Gerald Fogarty, Arturo Escamilla, Alex Perrottet, Tony Shannon, Craig Smith, David Curran, Fr. Paul, Fr. John, and my fellow residents; at the Maternal Heart of Mary Catholic Church: John-Paul, Bridget, Fr. Wong, Fr. Sypher, Fr. Gilbride. *Ad majorem Dei gloriam*, this thesis would have been impossible without their personal direction, dearest support, care and affection.

Finally, this research was supported by an AINSE Ltd. Postgraduate Research Award (PGRA).

Thesis submission for the degree of Doctor of Philosophy

Thesis Title and Abstract

Declarations

Inclusion of Publications
Statement

Corrected Thesis and
Responses

ORIGINALITY STATEMENT

I hereby declare that this submission is my own work and to the best of my knowledge it contains no materials previously published or written by another person, or substantial proportions of material which have been accepted for the award of any other degree or diploma at UNSW or any other educational institution, except where due acknowledgement is made in the thesis. Any contribution made to the research by others, with whom I have worked at UNSW or elsewhere, is explicitly acknowledged in the thesis. I also declare that the intellectual content of this thesis is the product of my own work, except to the extent that assistance from others in the project's design and conception or in style, presentation and linguistic expression is acknowledged.

COPYRIGHT STATEMENT

I hereby grant the University of New South Wales or its agents a non-exclusive licence to archive and to make available (including to members of the public) my thesis or dissertation in whole or part in the University libraries in all forms of media, now or here after known. I acknowledge that I retain all intellectual property rights which subsist in my thesis or dissertation, such as copyright and patent rights, subject to applicable law. I also retain the right to use all or part of my thesis or dissertation in future works (such as articles or books).

For any substantial portions of copyright material used in this thesis, written permission for use has been obtained, or the copyright material is removed from the final public version of the thesis.

AUTHENTICITY STATEMENT

I certify that the Library deposit digital copy is a direct equivalent of the final officially approved version of my thesis.

Thesis submission for the degree of Doctor of Philosophy

[Thesis Title and Abstract](#)

[Declarations](#)

[Inclusion of Publications
Statement](#)

[Corrected Thesis and
Responses](#)

UNSW is supportive of candidates publishing their research results during their candidature as detailed in the UNSW Thesis Examination Procedure.

Publications can be used in the candidate's thesis in lieu of a Chapter provided:

- The candidate contributed **greater than 50%** of the content in the publication and are the "primary author", i.e. they were responsible primarily for the planning, execution and preparation of the work for publication.
- The candidate has obtained approval to include the publication in their thesis in lieu of a Chapter from their Supervisor and Postgraduate Coordinator.
- The publication is not subject to any obligations or contractual agreements with a third party that would constrain its inclusion in the thesis.

The candidate has declared that **their thesis contains no publications, either published or submitted for publication.**

Candidate's Declaration



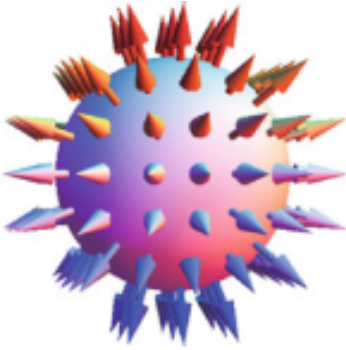
I declare that I have complied with the Thesis Examination Procedure.

1.1 Introduction to magnetic skyrmions

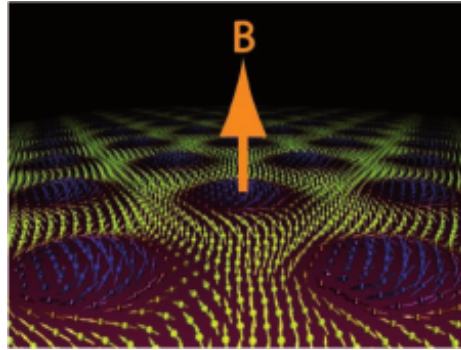
1.1.1 What is a skyrmion?

T. H. R. Skyrme proposed non-linear point-singularity particles – which are commonly referred to as skyrmions – as a model for hadrons in the context of field theory [1]. This model has been extended to different branches of physics such as the study of black hole solutions in cosmology, electric polarisation and magnetic ordering in transition metal oxides [2–5]. My Ph.D. project focuses on magnetic skyrmions: topological stable particle-like objects comparable to a spin vortex at the nanometre scale. An individual skyrmion is a set of rotating coplanar spins that usually form structures with a radius between 10-100 nm. Moreover, a long-range skyrmion order consists of several individual skyrmions forming a magnetic lattice and their most common symmetry is hexagonal across a plane normal to the direction of application of an external magnetic field (see figure 1.1, and table 1.1) [6].

Skyrmion lattices can appear in non-centrosymmetric chiral lattices as consequence of competing symmetric ferromagnetic exchange and antisymmetric Dzyaloshinskii-Moriya interactions. This competition may also induce a helical



(a) Schematic of a Hedgehog spin configuration (figure taken from [7])



(b) A 2D skyrmion lattice normal to an applied \vec{B} (figure taken from [8])

Figure 1.1: a) Illustration of a single spherical skyrmion, where each arrow represents the direction of the magnetic moment of a single ion pointing outwards and b) a lattice of 2D magnetic skyrmions parallel to an applied magnetic field.

magnetic ground state and field-induced conical states [6]. Moreover, the dynamics of magnetic skyrmions resemble the behaviour of flux line vortices found in high-temperature superconductors. Most skyrmion systems discovered are metallic, e.g. MnSi, FeGe and the room temperature skyrmion host $\text{Co}_8\text{Zn}_8\text{Mn}_4$ [9]. However, Cu_2OSeO_3 is – to the best of our knowledge – the only magneto-electric multiferroic skyrmion host, which opens avenues for the manipulation of magnetic skyrmions through applied electric fields [10]. Notice that investigating skyrmion dynamics could serve as an avenue to investigating the fundamental properties of the Higgs Boson and Abrikosov vortices in type-II superconductors [11]. For the experimental investigation of magnetic skyrmions, real-space techniques (*e.g.* Lorentz TEM, atomic force microscopy, and scalar magnetic X-ray tomography [12]), and reciprocal-space techniques (*e.g.* SANS and SAXS) provide detailed information on the formation of the skyrmion lattice, while inelastic neutron scattering and Raman scattering can probe the related spin- and lattice- excitations in the magnetic phases of Cu_2OSeO_3 and their energy scales (see sections 2.2, 2.4, and 1.2.4). Thus, our experiments aim help unveiling the complex quantum mechanical mechanisms behind the formation and stabilization of skyrmion lattices.

[†] $\text{BaFe}_{11.79}\text{Sc}_{0.16}\text{Mg}_{0.05}\text{O}_{19}$

[†] $\text{La}_{1.37}\text{Sr}_{1.63}\text{Mn}_2\text{O}_7$

Category	Symmetry	Material	T_C (K)	λ (nm)	Conduction
Chiral lattice FM	6-fold	MnSi [9, 13]	30	18	Metal
		$\text{Fe}_{1-x}\text{Co}_x\text{Si}$ [14, 15]	< 36	40 - 230	Semimetal
		MnGe [16]	170	3	Metal
		FeGe [17]	278	70	Metal
		Cu_2OSeO_3 [5, 18]	58	62	Insulator
Centro- symmetric FM		$\text{Y}_3\text{Fe}_5\text{O}_{12}$ [19]	560	> 500	Insulator
		RFeO_3 [19]	> 600	> 10^6	Insulator
		BFSMO* [20]	> 300	200	Insulator
		LSMO [†] [21]	100	160	Insulator
Interface	4-fold	Fe(hcp)/Ir(111) [22]	> 300	1	Metal
		FePd/Ir(111) [23]	> 300	7	Metal
		$\text{Co}_8\text{Zn}_8\text{Mn}_4$ [24]	> 300	~ 120	Metal
		$\text{Fe}_{2-x}\text{Pd}_x\text{Mo}_3\text{N}$	100	60	Metal

Table 1.1: Comparison of the temperature, field and symmetry conditions in which different materials host magnetic skyrmion lattices. The differences can be explained in terms of the balance of the magnetic interactions involved (see Sections 1.1.2, 1.3), the dimensionality of the samples, as well as the shape and size of the overlapping electron orbitals. Data extracted from [7, 24–26].

Types of skyrmions

The different symmetries of the magnetic interactions (see section 1.1.2) under the appropriate balance may give rise to two different kinds of two-dimensional magnetic skyrmions usually referred to as Néel- and Bloch-skyrmions. In the so called Bloch-type skyrmions, the direction of the spin vectors are tilted both in the radial (from the outer border to the center) and tangential components, while in the case of Néel-type skyrmions the spin vectors only rotate in the radial component (see figure 1.2). The different spin rotations represented by Néel- and Bloch-skyrmions can emerge from the relation between the crystalline symmetries and the lattice sites of the magnetic ions or the presence of crystallographic defects such as an interface, heterostructures, or magnetic domain walls [27].

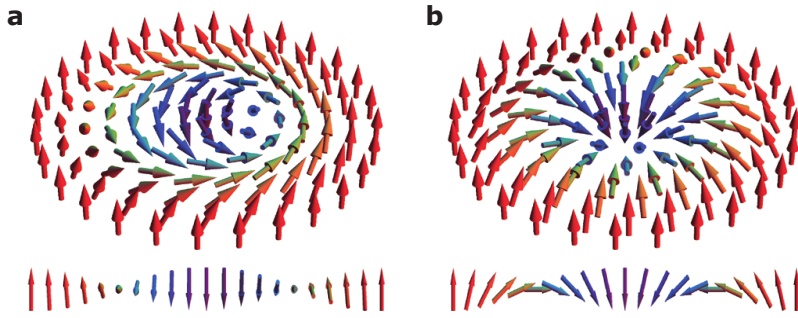


Figure 1.2: The spin configuration of 2D skyrmions responds to the underlying crystalline and spin-spin interaction symmetries, which can result in a) Bloch- and b) Néel-type skyrmions. The lower part of both a) and b) illustrate the cross section for the depicted configurations (image taken from [27]).

1.1.2 Magnetic interactions

Although magnetic phenomena have been known since the times in which Plato and Aristotle mentioned permanent magnets made of magnetite (Fe_3O_4) and written records of the use of magnetic compasses date back to ~ 1040 A.D., humanity had to wait until the nineteenth century to develop the classical theory of magnetism from the hands of Oersted, Biot, Savart, Ampere, and Maxwell, among others. However, the classical theory of magnetism fails to predict the onset of a macroscopic magnetisation in solids, for example, in ferromagnets. Thus, the existence of the intrinsic spin magnetic moment of electrons explained by the quantum exchange interaction is crucial in explaining macroscopic magnetic phenomena. Moreover, the origin of the relation between electricity and magnetism is of relativistic nature. [28–30].

Non-centrosymmetric spin environments such as the unit cell of Cu_2OSeO_3 host spin exchange interactions that can be separated into two terms: a symmetric term known as the ferromagnetic exchange interaction and the antisymmetric Dzyaloshinskii-Moriya interaction. In principle, magnetic exchange interactions arise as a consequence of the asymmetry of the total wave function of a fermionic system imposed by Pauli's exclusion principle, which yields an energy difference between symmetric and antisymmetric electron spin configurations [31, 32]. In the following paragraphs we will introduce the mechanisms behind magnetic ordering in solids.

Direct exchange

When the ions carrying a magnetic moment are nearest neighbours, the overlap between the relevant orbitals might be enough to enable direct exchange interactions, as in the case of ferromagnetic compounds containing $3d$ transition metal ions of iron, nickel and cobalt. Werner Heisenberg proposed a model for well localised magnetic moments, in which we assume that the orbital magnetic moment does not contribute, and the spins interact through the exchange interaction. Thus, the exchange energy of the Heisenberg Model is expressed by equation 1.1. Here, J_{ij} stands for the exchange constant between spins at lattice sites i and j and contains the energy effects of exchanging particles, and \vec{S}_i and \vec{S}_j represent the spin vectors for two neighbouring ions.

$$\hat{H}_{ex} = - \sum_{ij} J_{ij} \vec{S}_i \cdot \vec{S}_j \quad (1.1)$$

Notice, this interaction is usually very short-ranged due to the spatial dependence of the exchange constant. Generally, the solutions of the Heisenberg model are complicated, but $J < 0$ usually leads to ferromagnetic ground states while antiferromagnetism is the consequence of $J > 0$. Moreover, the assumption of well localised magnetic moments is a reasonable approximation for heavy ions such as $4f$ transition metals, but is not accurate describing the interactions between $3d$ ions even if we take into consideration additional terms stemming from the orbital magnetic moment [33].

Superexchange interaction

Low temperature antiferromagnetism has been observed in oxides in which the magnetic ions have no direct orbital overlap. In order to explain this, we must consider some kind of indirect exchange. In the case of transition metal oxides, fluorides and many other solids, the indirect exchange interaction between two magnetic ions takes place through the overlap with an intermediate non-magnetic ion (see figure 1.3). Usually, this interaction favours the formation of antiferromagnetic ground states [34].

Since this interaction involves two different orbital overlaps, it is a second-

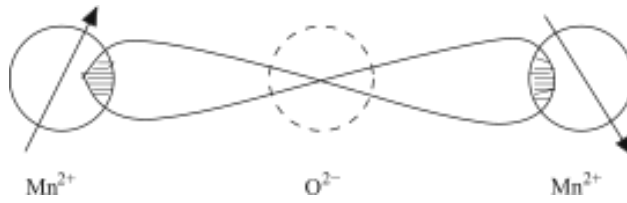


Figure 1.3: Illustration of the electron orbital overlaps involved in the superexchange interactions along a $\text{Mn}^{2+} - \text{O} - \text{Mn}^{2+}$ bond (image adapted from [35]).

order process that can be described using second-order perturbation theory in a tight binding model. This approach reveals that the exchange constant is directly proportional to the square of the transition matrix – dominated by the hopping integral t – and inversely proportional to the energy required to reach the excited electron state, which is determined by the Coulomb energy U . Ergo, the superexchange interaction is often described by a coupling constant of the type $J_{SE} \sim -t^2/U$, with the contribution of the direct exchange interaction being negligible. Moreover, due to the role of the intermediate ion, the strength of this interaction depends on the metal-oxygen-metal bond distance and angles.

Double exchange

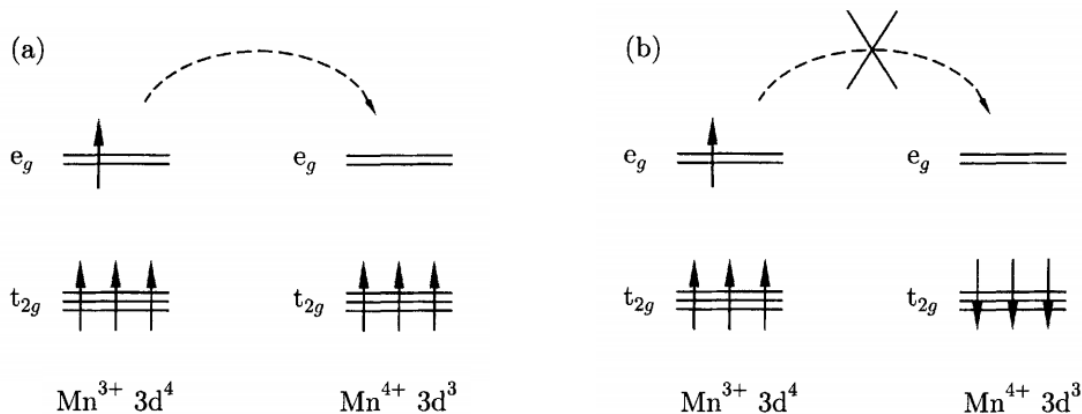


Figure 1.4: Illustration of the double exchange interaction mechanism. Two different scenarios are considered: a) an electron in the e_g state can easily jump into a vacancy on another lattice site if the spins of the electrons in the destination are parallel to the spin of the hopping electron, b) the same e_g cannot jump into another lattice site if a spin-flip is necessary (image taken from [34]).

A different kind of indirect exchange interaction, which may take place between the outermost electrons of mixed valency magnetic ions, that is, ions of the same element but with different state of oxidation. For instance, let us consider the ferromagnetic state of metallic 17.5% Sr-doped LaMnO_3 , which contains ions of both Mn^{3+} and Mn^{4+} in different lattice sites. In this case, it is energetically favourable that the e_g electrons hop from one lattice site to a neighbouring lattice site if a e_g vacancy in which the t_{2g} spins are aligned parallel to the spin orientation of the hopping e_g electron, i.e. the electron hops without flipping its spin orientation, hence, electron hopping favours the onset of a ferromagnetic state (see figure 1.4 (a)). Notice, that a spin flip of the hopping electron increases the kinetic energy since it entails that the e_g electron undergoes a strong in-site exchange interaction with the electrons in the t_{2g} energy state at the e_g vacancy site (see figure 1.4 (b)).

Anisotropic exchange or Dzyaloshinskii-Moriya interaction (DMI)

Until now, we have disregarded the effects of orbital magnetic moments, which we consider in this interaction. Dzyaloshinskii and Moriya suggested that the coupling between the spin and orbital degrees of freedom of electrons, which is known as spin-orbit coupling and whose energy is proportional to the product of both spin and orbital moments $\hat{L} \cdot \hat{S}$, can induce an electronic excited state in one of the neighbour ions. The exchange interaction between an excited ion and a neighbour in its ground state is modelled through equation 1.2 [36–38].

$$\hat{H}_{DMI} = \vec{D} \cdot \vec{S}_i \times \vec{S}_j, \quad |\vec{D}| \sim \lambda \vec{x} \times \vec{r}_{ij} \quad (1.2)$$

where \vec{S}_i and \vec{S}_j represent the spin vectors for the neighbouring ions; \vec{D} is a vector that depends on the symmetry of the crystallographic unit cell, and its magnitude is proportional to the strength of the spin-orbit coupling of the ground-state electrons, λ , and the ion displacements \vec{r}_{ij} and \vec{x} . The magnitude of \vec{D} becomes zero when the bond between the interacting ions has an inversion center, and acquires a finite value in non-centrosymmetric environments. Moreover, the direction of \vec{D} will be either parallel or perpendicular to the relative displacement \vec{x} of the magnetic ions depending on the crystallographic symmetries. In order

to minimize the energy of the spins, they tend to align 90° away from each other across a plane perpendicular to the \vec{D} vector (see figure 1.2). Consequently, if $\vec{D} \neq 0$, the magnetic moments tend to be tilted. A possible consequence of this spin canting is a small macroscopic magnetisation observed in antiferromagnets with no inversion centre in their unit cell, which is known as weak ferromagnetism as in the cases of LaCu_2O_4 , CoCO_3 , MnCO_3 and alpha iron oxide.

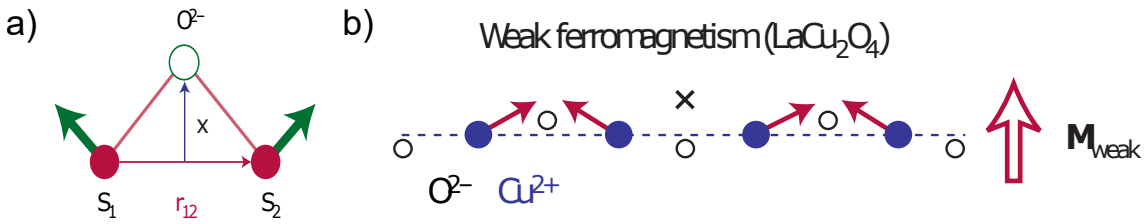


Figure 1.5: a) The Dzyaloshinskii-Moriya interaction induces a canting of the magnetic moments (green arrows) of two ions – one in its ground state and the other in an excited state – sitting on lattice sites 1 and 2. This canting is perpendicular to the relative displacement vectors \vec{r}_{12} and \vec{x} . Panel b) illustrates a canted configuration (vertical plane) of the Copper spins in LaCu_2O_4 , in which the Dzyaloshinskii-Moriya interaction gives rise to a weak ferromagnetic moment (image adapted from [39]).

1.1.3 Quantum topological effects

Topological protection

Skyrme proposed particles described by an integer topological number that can not be changed unless an abrupt change takes place in the quantum field describing these particles, i.e. there is no continuous deformation that could transform a non-topological state into a topological one, this phenomenon is known as topological protection of particles [1]. In other words, once the conditions to form skyrmions are met, a great amount of energy (for more information see [40]) is required to dissolve these vortices [6, 41]. This is a non-trivial characteristic since the topological nature of skyrmions governs most of their properties.

The topological number that describes skyrmions is a measure of the winding around a unit sphere of localised magnetic moments, which in the limit of two

dimensional magnetic skyrmions is defined by equation 1.3, where N is the topological winding number and \vec{S} represents the direction of the spins within the (x, y) plane [‡] [41].

$$N = \frac{1}{4\pi} \int \vec{S} \cdot (\partial_x \vec{S} \times \partial_y \vec{S}) dx dy = \pm 1 \quad (1.3)$$

Topological Hall effect

In the classical Hall effect, an applied current, j_x , induces an electric field, E_y , which is characterised by the Hall resistivity, $\rho_{xy} = E - y/j_x$. Additional contributions to the Hall resistivity may arise, for example, proportional to the magnetisation of ferromagnets as in the anomalous Hall effect, or due to Berry phase effects in topological spin textures [43–48].

The electromagnetic field that emerges from the chiral spin configuration of magnetic skyrmions produces topological phenomena such as the topological Hall effect on conduction electrons in metals. It has been experimentally observed that the translational movement of magnetic skyrmions across a lattice generates an electromagnetic induction that deviates the trajectory of conduction electrons through a Lorentz force as described by the Boltzmann equation [6]:

$$\partial_t f + \vec{v} \cdot \vec{\nabla}_r f - e \left[(\vec{E} + \vec{e}) + \vec{v} \times (\vec{B} + \vec{b}) \right] \cdot \vec{\nabla}_k f = -\frac{1}{\tau} (f - f_0) \quad (1.4)$$

where $f(\vec{r}, \vec{k}, t)$ is the distribution function of the conduction electrons at time t , \vec{E} and \vec{B} are the electric and magnetic fields applied to the sample, \vec{e} and \vec{b} represent the emergent electric and magnetic fields, and the conduction electrons are characterised by a wavelength \vec{k} , velocity \vec{v} , mean free time τ , equilibrium distribution f_0 and charge $-e$. Additionally, moving skyrmions deviate their trajectories by virtue of the emergent electromagnetic field in the so-called skyrmion Hall effect originated by the Lorentz force expressed in the third term on the left hand side of equation 1.4 (see figure 1.6). Moreover, the induced electromagnetic field leads to a torque upon the spin of the conduction electrons that fulfils the Landau-Lifshitz-Gilbert model [6]:

[‡]Topological structures different from skyrmions are described by $N \neq \pm 1$ [25, 42].

$$\partial_t \vec{S} + (\vec{j} \cdot \vec{\nabla}) \vec{S} = -\vec{S} \times \partial_{\vec{S}} H_s + \vec{S} \times [\alpha_G \partial_t \vec{S} + \beta (\vec{j} \cdot \vec{\nabla}) \vec{S}] \quad (1.5)$$

in which, \vec{S} represents the direction of the spins within the (x, y) plane, \vec{j} is the conduction electrons current density, the spin Hamiltonian is given by H_s , α_G stands for the Gilbert damping constant and non-adiabatic effects are contained in β . As a consequence of the magnitude of these effects, experimental measurements of the giant topological Hall effect enable the detection of the formation of magnetic skyrmions in metallic materials [49–52].

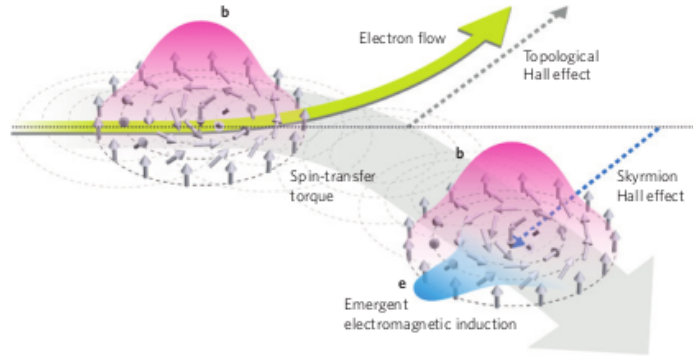


Figure 1.6: Illustration of the topological Hall effect. The chiral arrangement of magnetic moments of skyrmions create an emergent electric (magnetic) field represented in blue (pink) and denoted by the letter e (b). The yellow arrow illustrates the trajectory of the conduction electrons through the lattice and the grey arrow the trajectory of moving skyrmions (image taken from [6]).

1.2 The material: Cu_2OSeO_3

1.2.1 Cu_2OSeO_3 : A Multiferroic Transition Metal Oxide

Transition Metal Oxides

It has been extensively proven that Transition Metal Oxides (TMOs) can host exotic physical phenomena such as Mott insulating states, High Temperature Superconductivity (HTSC) and Colossal Magnetoresistance (CMR) [39]. The interplay

between the quantum degrees of freedom of the constituent particles of a solid determines the resulting structure and properties of the material. These quantum mechanical interactions in bulk, thin films and TMOs heterostructures, give rise to a plethora of electronic and magnetic scenarios, ranging from simple metallic to insulating behaviour or exotic quantum mechanical ground states. The magnetic, electronic and mechanical observables in TMOs can exhibit spontaneous macroscopic orders such as ferro- or antiferromagnetism, ferroelectricity and ferroelasticity [53].

The novel properties of TMOs originate on the nature of the partially filled outer d -electron shells of the transition metal ions. Most stoichiometric $3d$ TMOs with half filled bands exhibit antiferromagnetic (AFM) Mott insulating phases, as modelled by the accepted theoretical framework, which states that the localized $3d$ states produce strongly correlated bands with a large on-site Coulomb repulsion (U) and a small bandwidth (W) [54]. Moreover, the Coulomb repulsion between anisotropic electron orbitals plays a major role in our understanding of metal-insulator transitions and the properties of TMOs [55]. My research project focuses on the magneto-optic phenomena of the single $3d$ transition metal oxide Cu_2OSeO_3 , whose intriguing properties are introduced in the following sections.

Multiferroics

Multiple ferroic orders can coexist in multiferroic materials. For instance, magnetic multiferroics simultaneously break the time- and translation-reversal symmetries and allow the coexistence of magnetic and electric polarizations. In some materials, the magnetic and electric polarisations are coupled to each other, a condition known as the magnetoelectric coupling, which entails that a change in the electric polarisation drives a change in the magnetisation or vice versa. Two noticeable examples of magnetoelectric coupling are given by TbMnO_3 and the room temperature multiferroic BiFeO_3 . Additionally, multiferroics can be classified according to their underlying mechanisms as type I and type II multiferroics. In type I multiferroics, the magnetic and electric order arise from mechanisms that are mostly independent from each other, which manifests in different onset temperatures for both orderings, as in the case of BiFeO_3 . Whereas, in type II

multiferroics, the onset of magnetic ordering causes an electric polarisation in the material as an effect of a strong magnetoelectric coupling, which is the case of TbMnO_3 [39, 56–62].

Multiferroic systems open avenues for fundamental research and future technological applications where the coexistence of both charge and spin components can be exploited, and one polarisation could be used to drive the other, such as in data storage and processing, communication and sensor devices [39, 63–65]. Moreover, the manipulation of magnetic components in memory storage devices through applied electric fields would improve both the speed of data storage and retrieval processes. This possibilities make of Cu_2OSeO_3 an interesting skyrmion host, in which magnetic and electric spontaneous polarisations emerge below $T_C \approx 58$ K and prevail in the skyrmion phase [66, 67] (see section 1.4).

1.2.2 Crystal structure

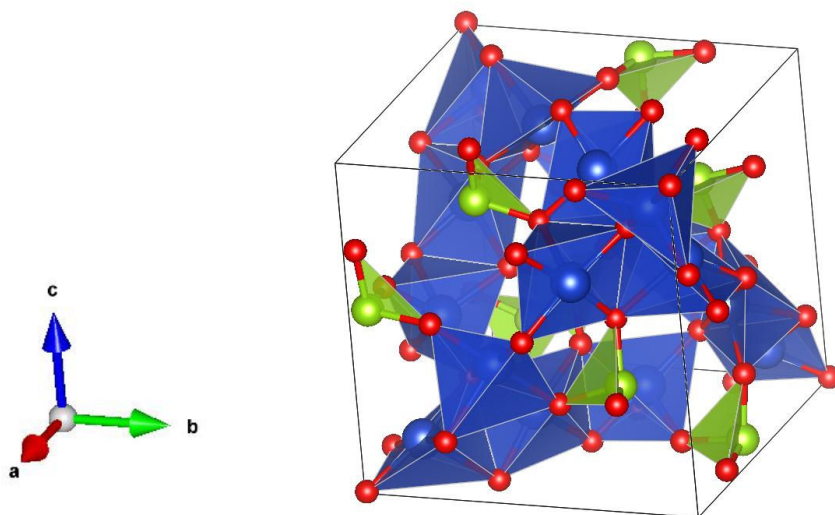


Figure 1.7: The unit cell of Cu_2OSeO_3 is described by the $P2_13$ space group (number 198 in [68]) together with the B20 alloys. Here, the Copper ions sit inside trigonal pyramids (green shapes) and square pyramids (blue shapes) in a 1 to 3 ratio that induces a dominant ferrimagnetic term. Red, green, and blue spheres represent the Oxygen, Selenium and Copper ions, respectively. Image generated using the crystal visualisation software VESTA [69].

Single crystals and powder samples of Cu_2OSeO_3 were first grown via chemical

vapour transport in the context of the study of selenites and tellurites of iron group ions. X-rays characterisation unveil its unit cell is cubic with $\approx 8.924 \text{ \AA}$ per side at room temperature and belongs to the $P2_13$ space group (number 198) [70–72]. This crystalline structure contains two different oxygen environments around the copper ions given by three square pyramids and trigonal pyramid of oxygen bonds per unit cell (see figure 1.7).

1.2.3 Magnetic phases

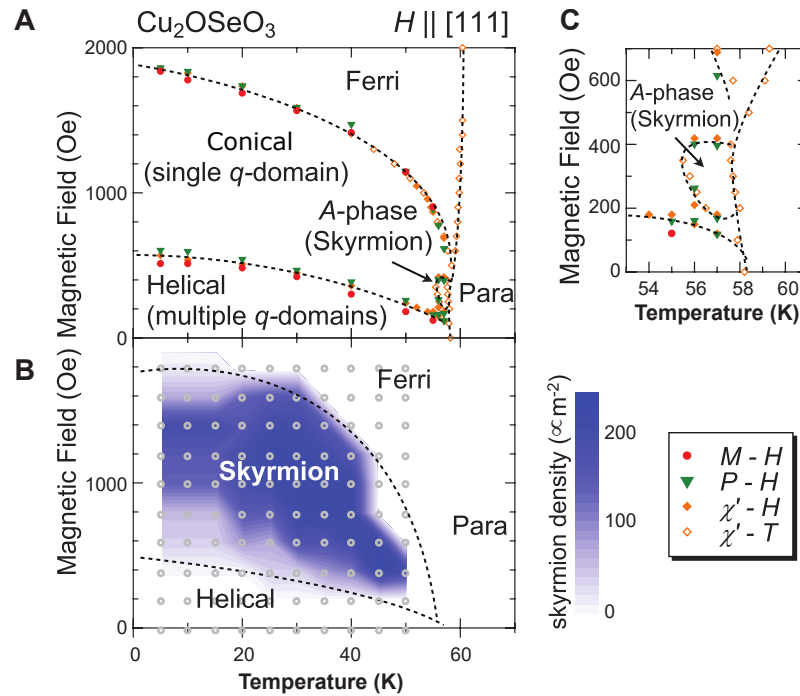


Figure 1.8: Magnetic phase diagram of Cu_2OSeO_3 a) single crystals and b) thin films determined by magnetisation (M), electric polarisation (P) and ac magnetic susceptibility measurements (χ'). The small region where a skyrmion lattice forms on a) bulk samples is shown in greater detail in panel c) and panel b) shows how the A-phase grows both in temperature and field range when the bulk samples are cut into thin slabs (image adapted from [5]).

Initially, researchers thought Cu_2OSeO_3 was a diamond-type superstructure with 3 of the Cu^{2+} spins up and 1 spin down yielding a ferrimagnetic ground state [73]. However, more systematic and sensitive studies reveal a richer magnetic phase diagram upon zero-field cooling (see figure 1.8), where the DMI induces a spin canting that leads to a multi-domain helical magnetic ground state

in which the spins rotate within planes normal to the propagation vector of the helices. A distortion of the helical phase known as the conical phase occurs upon application of weak external magnetic fields, in which the spin helices within a domain acquire a small magnetisation component parallel to the applied field. Eventually, the spins are completely parallel or antiparallel to the applied field and the magnetisation saturates in a ferrimagnet. Additionally, hexagonal skyrmions lattices have been observed in single crystals of Cu_2OSeO_3 at a narrow temperature and tiny magnetic field region – known as the A-phase – close to the magnetic phase transition temperature ($T_C \sim 58$ K). However, it has been reported the area of the A-phase grows when the bulk samples are reduced to a thin-film [5].

1.2.4 Lorentz Imaging in Cu_2OSeO_3

Max Knoll and Ernst Ruska (Physics Nobel prize 1986) developed the Transmission Electron Microscopy (TEM) in 1931. In a TEM instrument, a high energy electrons (100-1000 keV) is focus on a thin film ($\lesssim 100$ nm) with greater resolution than optical microscopes due to the small electron wavelength. As the beam passes through the material, the electrons with velocity \vec{v} interact electromagnetically with the atoms of the sample and deflect due to a Lorentz force, \vec{F} , induced by a transversal magnetic field, \vec{B} [74]:

$$\vec{F} = e(\vec{v} \times \vec{B}) \quad (1.6)$$

As a result of this force, the number of transmitted electrons and their quantum mechanical phase change according to the transport of intensity equation 1.7. This expression derives from the probability current through the sample and the continuity equation for a beam of partially coherent electrons propagating along the z direction with momentum p [75]:

$$\frac{\delta T(\vec{r})}{\delta z} = -\frac{\hbar}{p} \vec{\nabla} \cdot \left(T(\vec{r}) \vec{\nabla} \phi(\vec{r}) \right) \quad (1.7)$$

where $T(\vec{r})$ is the transmitted intensity at position \vec{r} , ϕ is the phase change and $\delta_z T(\vec{r})$ is the longitudinal probability gradient that can be measured by over

and under focusing the microscope along the z direction. Equation 1.7 can be uniquely solved for ϕ once T and $\delta_z T$ are known. Moreover, ϕ contains information about the transversal magnetic environment of the ions in the sample.

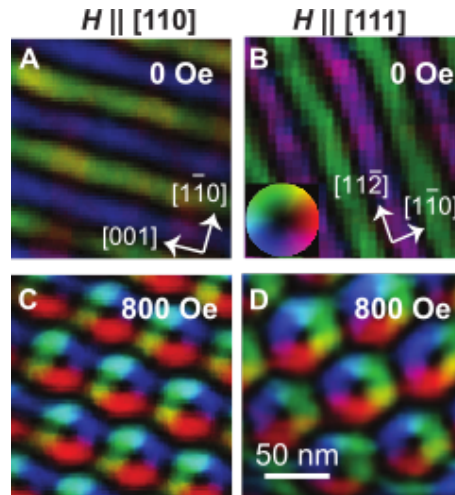


Figure 1.9: Lorentz TEM colour map of the in-plane magnetisation texture of a thin slab of Cu_2OSeO_3 in the a,b) helical and c,d) skyrmion phases with an applied magnetic field normal to the $[110]$ and $[111]$ axes on the left and right hand sides. The hue on panel b) uses the colour and opacity to indicate the orientation and magnitude of the lateral magnetic moments (image extracted from [5]).

This over- and under-focusing method is known as Lorentz TEM imaging and enables investigating magnetic textures with great resolution. For example, the real space distribution and orientation of the magnetic moments in a skyrmion lattice have been measured on thin slabs of pristine Cu_2OSeO_3 by Tokura *et al.* [5], Han *et al.* [76] and confirmed the hexagonal arrangement of these pseudo-particles within the skyrmion phase (see figure 1.9).

1.2.5 Latest developments

Skyrmion subphases at high temperature

Tokura, Keimer *et al.* found rotations of the skyrmion lattice using small angle neutron scattering around the region of the magnetic phase diagram where they also found anomalies in the real part of the ac susceptibility [10]. These rotations of the magnetic lattice manifest as changes in the polar angle of the propagation

vector, q , of the magnetic Bragg reflections (see also 2.2) [9]. This team accumulated diffraction patterns with the incident neutron beam normal to the plane containing the $\langle 110 \rangle$ and $\langle 001 \rangle$ crystallographic axes, and applied a magnetic field in the $[110]$ direction. The measurements reveal two different regions inside the A-phase (see figure 1.10); these subphases differ from each other by a sudden rotation of the Bragg peaks. Around $T = 57$ K and $H = 250$ Oe, one of the three propagation vectors is parallel to the $\langle 110 \rangle$ vector. However, the skyrmion lattice undertakes a rotation of 30 degrees that tilts the q vectors so that one of them points towards the $\langle 001 \rangle$ direction around $T = 57.5$ K and $H = 150$ Oe. At the border between these regions, a mixed skyrmion orientation state was observed although this rotation is not characterised by any ac susceptibility or integrated neutron scattering intensity anomaly. Interestingly, such rotations of q did not appear along the helical phase upon different temperature and magnetic field conditions. A semi empirical Ginzburg-Landau study suggests that the preferred orientation of the q vectors is influenced by high order magnetic anisotropy terms given by $\sum_q (q_x^6 + q_y^6 + q_z^6) |\vec{m}_q|^2$ and $\sum_q (q_x^4 q_y^2 + q_y^4 q_z^2 + q_z^4 q_x^2) |\vec{m}_q|^2$ with \vec{m}_q representing the Fourier transform of the microscopic magnetisation $\vec{M}(\vec{r})$; these two sums tend to orient the q vectors parallel to $\langle 110 \rangle$ or $\langle 001 \rangle$ respectively. The observed skyrmion lattice rotations suggest the magnetic anisotropies are weak, but further theoretical analysis is required.

Second skyrmion phase at low temperature

The recent discovery of a low temperature skyrmion phase stands out among the extensive research on Cu_2OSeO_3 since the previous observations of the A-phase in skyrmion materials strongly suggest this skyrmion lattice is stabilised by thermal fluctuations close to the magnetic transition temperature, T_C . Thus, the appearance of a long-range skyrmion order at lower temperatures suggests additional interactions could play the role of thermal fluctuations in this thermal regime [77].

In a recent Nature Physics publication, Pfleiderer *et al.* reported the observation of a second skyrmion phase that is thermodynamically disconnected from

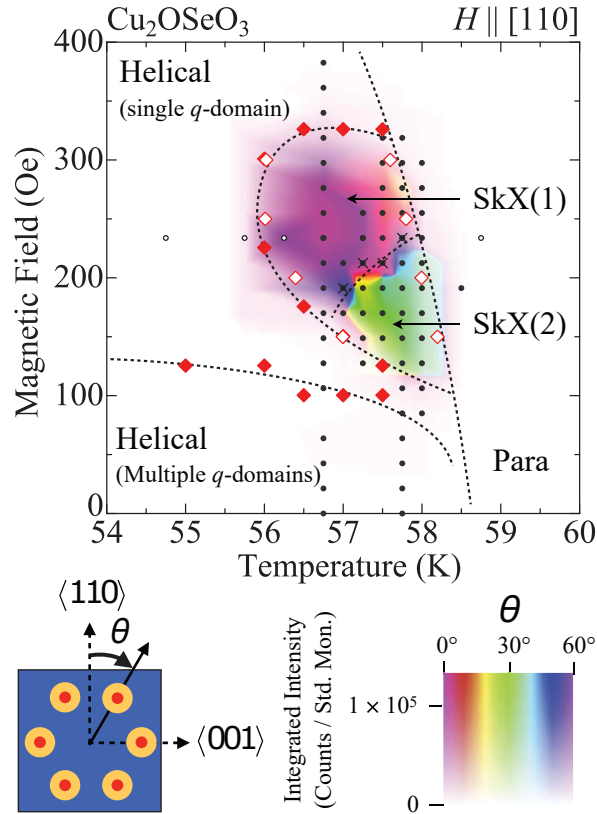


Figure 1.10: The systematic phase diagram (top) of Cu_2OSeO_3 measured with small angle neutron scattering reveals a rotation of the propagation vectors quantified by the angle θ with respect to the $\langle 110 \rangle$ axis (lower left panel). The background colour (lower right panel) indicates the value of this angle. The solid (open) diamonds indicate the appearance of ac susceptibility anomalies and the black (open) circles represent the conditions used during the field (temperature) neutron scattering scans (image taken from [10]).

the small pocket in the magnetic phase diagram located just below T_C [78]. The small angle neutron scattering measurements performed on undoped Cu_2OSeO_3 single crystals generated different phase diagrams depending on the cooling conditions and the orientation of the sample with respect to the applied magnetic field and the neutron beam (see figure 1.11). Noticeably, the low temperature skyrmion phase was observed only upon field cooling with the crystallographic $[001]$ axis of the sample aligned parallel to both the applied magnetic field and the incoming neutron beam. Furthermore, the temperature and field range of this new phase is highly influenced by the intensity of the magnetic field applied during the cooling phase. These neutron scattering observations together with

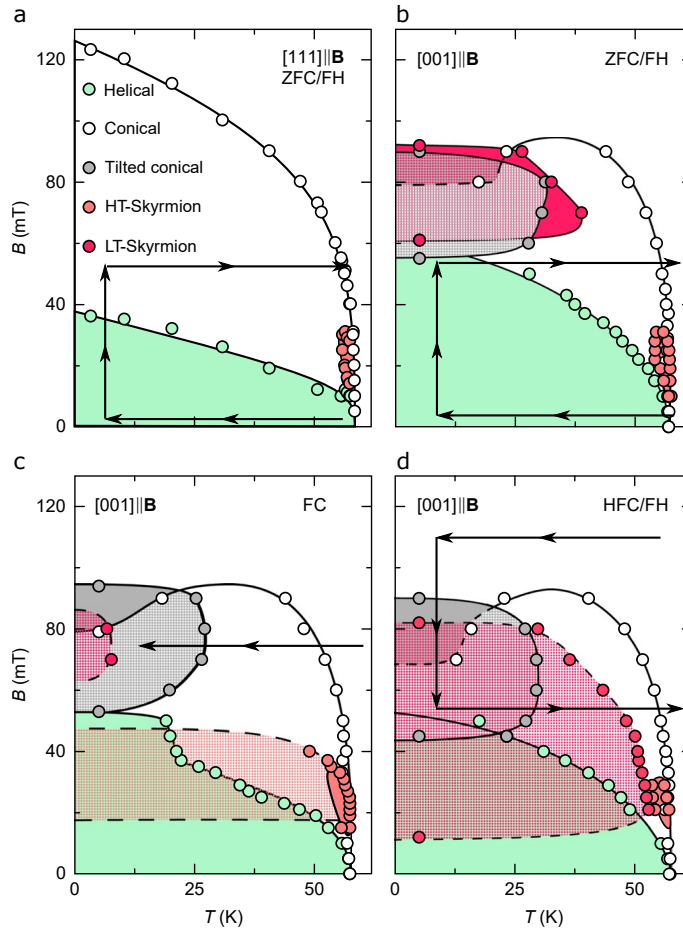


Figure 1.11: Magnetic phase diagram of Cu_2OSeO_3 reported by Pfleiderer *et al.* upon a) zero field cooling - field heating with the beam along the $[111]$ axis, b) zero-field cooling - field heating along the $[001]$ direction, c) field cooling along $[001]$ and d) high field cooling - field heating along the $[001]$ axis. The bold black arrows represent the thermodynamic path used during the measurements. (image taken from [78])

specific heat, magnetisation and ac susceptibility features [79] led them to conclude that cubic magnetic anisotropies are responsible for the stabilisation of this low temperature phase.

Mostovoy *et al.* have extended the observation of the formation of low temperature skyrmions normal to the $\langle 001 \rangle$, $\langle 110 \rangle$ and the $\langle 111 \rangle$ crystallographic axes during small angle neutron scattering and magnetometry experiments upon magnetic field cooling [77, 80]. This group claims robust skyrmions can emerge at low temperatures along all crystallographic directions thanks to competing cubic and exchange anisotropies. Moreover, they observed no gap between the low

and high temperature skyrmion regions of the phase diagram, which could point at a smooth transition between stabilisation mechanisms.

1.3 Stabilisation of magnetic skyrmion lattices

Stable magnetic skyrmions lattices may form upon an applied magnetic field as a result of a balance between different magnetic interactions: a) long range dipole-dipole interactions that favour in-plane ordering in thin films, b) DMI in magnets with no center of symmetry in their unit cell, c) frustrated magnetic exchange interactions, and d) 4-spin exchange [6]. My research focuses on skyrmions in magnetic materials lacking a symmetry center, also known as non-centrosymmetric. In these helimagnetic materials, the antisymmetric DMI stabilises a long-range spin canting and may result in the formation of individual skyrmions that form lattices perpendicular to the applied field within a narrow region in the temperature-magnetic field phase diagram close to the paramagnetic transition temperature (see figure 1.10), as it has been experimentally observed in manganese MnSi, $\text{Fe}_{1-x}\text{Co}_x\text{Si}$, FeGe and Cu_2OSeO_3 . Nevertheless, helical, conical and skyrmion lattice modulated phases compete to settle down in these materials and the energetic differences between them are small. Thus, the energy balance can be tuned by weak interactions such as thermal or magnetic fluctuations, magnetic anisotropies, dipolar interactions or the softening of the magnetic modulus. Consequently, external excitations such as applied electric or magnetic fields, and external or chemical pressure can modify the pocket of the phase diagram in which skyrmion lattices stabilise [81, 82]. In particular, thermal fluctuations are deemed as the main energetic contributions driving the spin-cycloid to skyrmion phase transition in DMI chiral magnets [83, 84].

In addition, it has been reported that the competition between magnetic dipolar interactions and easy-axis anisotropies generate stable skyrmion lattices in thin film samples [6]. Although dipolar interactions tend to induce an in-plane magnetisation and perpendicular anisotropies favour an out-of-plane ordered state, their competition renders a ground state described by magnetic stripes that turns into a skyrmion lattice upon the application of an external magnetic field. Fur-

thermore, it has been proposed that frustrated exchange interactions and four-spin exchange interactions can yield to a skyrmion ordered state in frustrated magnets and atomically layered thin films, respectively.

On the other hand, metastable skyrmion lattices can originate outside their stable region of the phase diagram; these metastable lattices originate upon ultrafast FC across the skyrmion phase from the topological protection of skyrmions that grants them a long lifetime. The lifetime of these particles makes them persistent at low temperatures upon fast FC (they linger for a week or longer in the case of MnSi), but increasing thermal fluctuations reduce their lifetime [85].

Moreover, experimental and theoretical evidence suggest that a skyrmion is strictly protected by its topology only in a continuum, whereas the topological protection is only partial in the presence of a discrete atomic lattice [86–89]. Consequently, magnetic skyrmions in real materials have a finite lifetime and the skyrmion collapse rate is related to the Arrhenius law at fixed homogeneous temperatures:

$$1/\tau = k(T)\exp\left(-\frac{E_g}{k_B T}\right) \quad (1.8)$$

where τ indicates the expected lifetime of quasi-equilibrium skyrmions, $k(T)$ is the Arrhenius prefactor, E_g is the energy gap between the initial skyrmion state and the final magnetic state, k_B is the Boltzmann constant and T the temperature of the sample.

1.3.1 Classical and topological phase transitions

The stability of a given phase of condensed matter is determined by those conditions that minimise either the thermodynamic Helmholtz free energy given by $F = E - TS$ (where E is the internal energy of a system with temperature T and entropy S), or a minimised Gibbs free energy, $\Phi = F + PV$ (where P and V represent the pressure and volume of the system). From these expressions, we can infer that a disordered state is favoured by an increasing temperature. Conversely, a reduction of the temperature of a system will increase the plausibility of reaching an ordered state. Usually, this order will manifest through the symmetry of

the crystallographic lattice, electric or magnetic polarisation or some macroscopic variable also known as the order parameter, η [38, 90].

In general, the order parameter will be a function of external factors that can be controlled in a laboratory setting. From this dependence, two different types of phase transitions emerge: discontinuous phase parameters define first-order phase transitions and continuous changes of the phase parameter are known as second-order phase transitions (see figure 1.12).

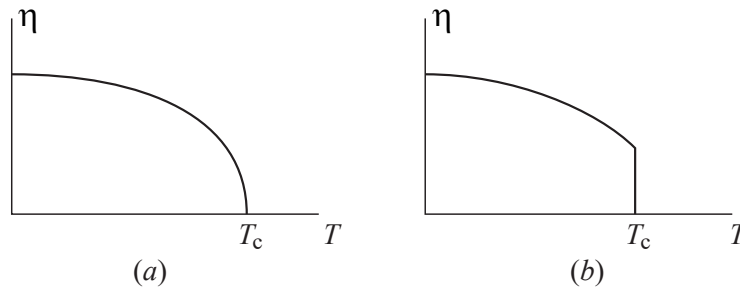


Figure 1.12: The continuity of the curve of the order parameter as a function of an external variable will determine if the phase transition is of (a) second order or first order (image taken from [90]).

The Landau model

Landau modelled the Gibbs free energy, $\Phi(P, T, \eta)$, as a Taylor series to study second order phase transitions close to the phase transition temperature, T_C , since the order parameter takes small values in the vicinity of T_C :

$$\Phi = \Phi_0 + \alpha\eta + A\eta^2 + C\eta^3 + B\eta^4 + \dots \quad (1.9)$$

where the coefficients will be determined by the conditions that minimise Φ . Since the phase transition occurs when $\eta = 0$, we obtain $\alpha = 0$. Additionally, the coefficient $A(P, T)$ should be positive for $T > T_C$ and negative below T_C to quench the order parameter above the transition and produce finite positive values of η at lower temperatures. Hence $A(P, T) = a(T - T_C)$. Furthermore, we can use a similar argument to obtain $C = 0$. Therefore, the Gibbs free energy is usually expressed as

$$\Phi = \Phi_0 + a(T - T_C)\eta^2 + B\eta^4, \quad (1.10)$$

which leads to a stable state when $\partial_\eta \Phi = 0$. In the case of first order phase transitions, the coefficient $C \neq 0$ may yield to situations in which a second local minimum arises and manifests either as a metastable state or a new absolute minimum. If a new absolute minimum value of the free energy appears at a given T_C^I , the system could abruptly change state and a discontinuous order parameter.

In the case of an inhomogeneous order parameter, $\eta(\vec{r})$, an energy cost is associated with the variation of space. Thus, the free energy is calculated using the Ginzburg-Landau functional (which is often used in the context of magnetic domain walls):

$$\Phi = \int \left(A\eta^2(\vec{r}) + B\eta^4(\vec{r}) + G(\vec{\nabla}\eta(\vec{r}))^2 \right) d^3\vec{r} \quad (1.11)$$

Superconducting phase transitions

In this context, the order parameter is interpreted as the wavefunction of the superconducting pair of electrons, ψ , and we obtain the Ginzburg-Landau equation of superconductors:

$$\frac{1}{2m} \left(-i\hbar\vec{\nabla} - \frac{2e}{c}\vec{A} \right)^2 \psi + A\psi + 2B|\psi|^2\psi = 0 \quad (1.12)$$

Here the magnetic vector potential \vec{A} and m is the mass of the superconducting pair of electrons. Notice, this equation is not a complete analogous to the Schroedinger equation since it contains a term proportional to ψ^3 . Nonetheless, the equation can be linearised close to the phase transition, at which ψ tends to zero. In the context of ferromagnets or magnetic domain walls, we arrive to a similar equation also known as the Landau-Lifshitz equation. Moreover, the Ginzburg-Landau formalism has been used to investigate the emergence of magnetic spin spirals and skyrmion lattices [9, 91, 92]. In the case of these spin spirals and magnetic skyrmions, the Ginzburg-Landau functional is written in terms of the magnetisation, \vec{M} , in the mean-field approximation as:

$$\Phi(\vec{M}) = \int \left(r_0\vec{M}^2 + J(\nabla\vec{M})^2 + 2D\vec{M} \cdot (\vec{\nabla} \times \vec{M}) + U\vec{M}^4 - \vec{B} \cdot \vec{M} \right) d^3\vec{r} \quad (1.13)$$

where the third term takes into account the energetic contribution of the relativistic Dzyaloshinskii-Moriya interaction and the last term considers the coupling between the external magnetic field and the magnetisation vector.

Quantum phase transitions

So far, we have considered the case in which phase transitions take place at a finite temperature. Nevertheless, in some cases the transition temperature can be reduced to zero through the application of another control parameter, g , such as external pressure, electric or magnetic fields or through atomic substitution. Simultaneous to the reduction of the temperature of the system, quantum effects start playing a more significant role. In such systems quantum fluctuations keep the system in a disordered state unless an additional control parameter reaches a critical value also known as a quantum critical point ($T = 0, g = g_C$).

It has been argued that the phase transition from the tilted spin spiral state (also known as conical phase) and the skyrmion phase is a Quantum Phase Transition (QPT) of the first order due to the discontinuous behaviour of the magnetic susceptibility and of the neutron scattering intensity measured with small-angle neutron scattering (see Sections 1.2.3 and 2.2) [9, 93, 94]. However, the quantum nature of the transition might not be enough to call this process a QPT since a topological phase transition takes place between the skyrmion phase characterised by a quantised winding number and the non-topological magnetic phases next to it, which could be modelled by the melting theory developed by Kosterlitz, Thouless, Halperin, Nelson and Young (KTHNY), which is a corollary of the theory of topological phase transitions in two-dimensional systems awarded with the Nobel Prize in Physics on 2016, and consists on a two-step phase transition governed by the emergence of topological defects [95–99].

1.4 Potential applications of Magnetic Skyrmions

Magnetic skyrmion materials offer broad perspectives for consumer magnetic nanotechnology applications due to their topological protection and emergence close to room temperature as in the cases of $\text{Co}_8\text{Zn}_8\text{Mn}_4$, FeGe thin films and syn-

thetic antiferromagnetic layers of Pt/Co/Ru [17, 24, 87]. So far, different research groups have demonstrated the capabilities for skyrmion-based data storage and processing: writing, reading and processing through the creation, annihilation, displacement and detection of individual skyrmions. Although the current advances in skyrmion electronic devices offer higher data density capabilities than traditional hard drives and low energy consumption based on dissipation-less skyrmion manipulation, further advances such as full functionality at room temperature are required to compete with current computing technologies [2, 41, 65, 100, 101]. In the next paragraphs, we will introduce some of the conceptual and prototype electronic components based on magnetic skyrmions.

1.4.1 Skyrmion racetrack memories

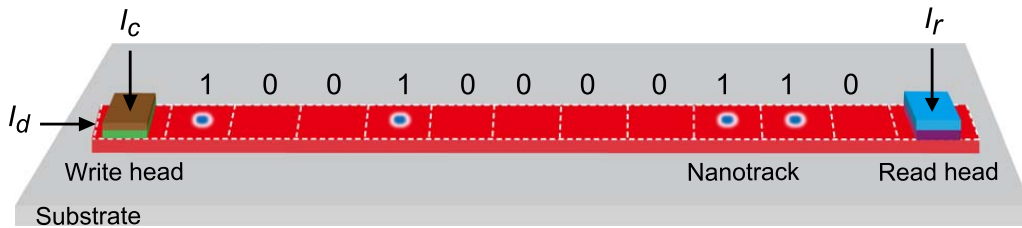


Figure 1.13: Schematic of a skyrmion racetrack memory composed of a write head that induces individual skyrmions through an applied creation current, I_c , a nano track that hosts the movement of a sequence of individual skyrmions through a driving current, I_d , and a read head that detects skyrmions through a reading current, I_r . These currents are generated by additional circuits attached to the racetrack memory (image taken from [65]).

Thin films and nanowires have been engineered as room-temperature data storage devices usually referred to as magnetic racetracks [102–104]. Magnetic skyrmions have been successfully used to encode information along racetrack memories in a similar way to domain wall memories. In these devices, individual skyrmions are created at one end of the racetrack and their dynamics is controlled through an applied electric current. To confine the motion of the skyrmions, the thickness of the magnetic track is smaller than the diameter of a single skyrmion in bulk. Moreover, the spacing between single skyrmions in

a sequence can match the diameter of single skyrmions, which increases the density of data within these devices (see figure 1.13) [41, 101, 102].

1.4.2 Skyrmion logic devices

A possible extension of the racetrack memory is a skyrmion-based transistor that controls the propagation of each single skyrmion along the track depending on the value of an applied electric field at a gate on top of the nano track. To this end, ferromagnetic racetracks on top of a heavy metal substrate have been proposed. In this case, the gate would locally modify the magnetic anisotropy or the intensity of the Dzyaloshinskii-Moriya interactions (see figure 1.14) [41].

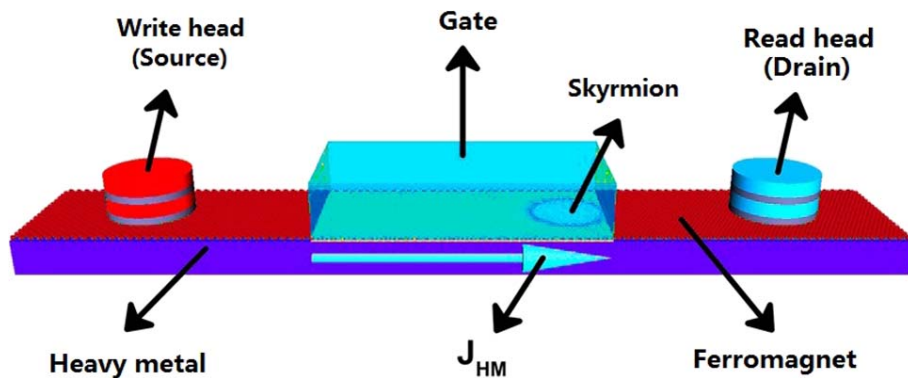


Figure 1.14: A conceptual skyrmion-based transistor design has been proposed, in which the skyrmions are injected by a source into a ferromagnetic track. An electric current that flows along the heavy metal substrate, J_{HM} , would induce the movement of the individual skyrmions along the track until they reach the gate. Depending on the voltage at the gate, the skyrmions could be annihilated or reach the drain where they would be detected (image taken from [65]).

Moreover, it has been proposed to use the quasi-particle topological properties of individual skyrmions and the development of skyrmion-based transistors to craft logical AND, OR and NOT gates that would provide a complete set of instructions for a computer architecture based on these magnetic vortices. Additionally, it has been proposed that quantum information can be encoded in the degree of helicity of magnetic skyrmions and this could be manipulated through applied electric and magnetic fields in skyrmion qubits for quantum computing [105].

1.4.3 Skyrmion magnonic and radio-frequency devices

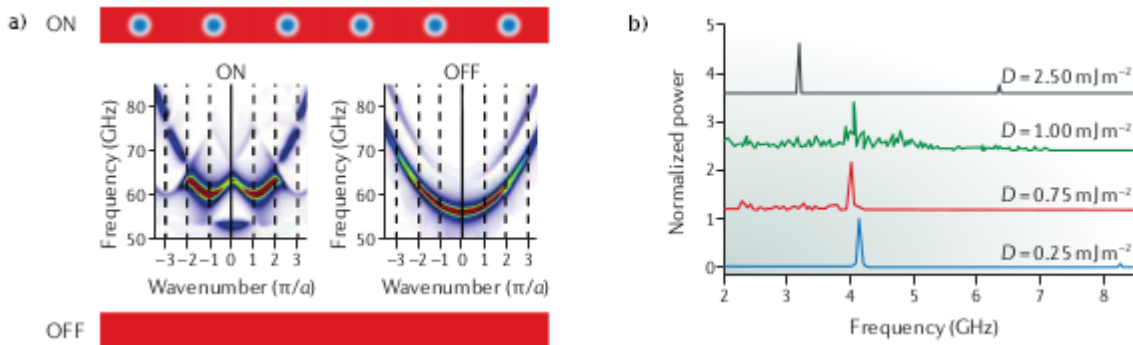


Figure 1.15: a) A simulated periodic skyrmion lattice (top) can work as a magnonic device and induce gaps in the dispersion relation of magnons (center left) at frequencies that match the periodicity of the skyrmion lattice. These gaps can be turned off (center right) when the skyrmion lattice is cleared (bottom). b) The simulated frequency spectra of magnetic skyrmions can display different normal modes when the intensity of the DMI is engineered by external stimuli, thus acting as a frequency filter (Both panels were taken from [41]).

The capability to create and annihilate individual skyrmions opens the door for the creation of periodical skyrmion lattices that could be used to control the propagation of spin waves along a wave guide. This spintronic application of skyrmions could be achieved at a smaller length scale than the currently available wave guides fabricated via lithographic techniques (see figure 1.15a).

Additionally, the low frequency magnetic excitations (the so called breathing modes) within single skyrmions could be used to emit radio frequency signals from individual skyrmions sitting on a magnetic site of a magnetoresistive device. These devices could be used as frequency filters or detectors in the microwave range (see figure 1.15b).

In this chapter, we will briefly introduce the experimental methods used to detect skyrmions in real and reciprocal space to gain insight into their behaviour. A deeper discussion about the techniques used as part of my thesis will be provided in the following chapter.

2.1 Sample preparation

In this section we explain how our collaborators at the University of Auckland (Rosanna Rov, Luis Camacho and Tilo Soehnel) prepared the samples using the Chemical Vapour Transport (CVT) method briefly introduced in section 1.2.2. Let us now delve deeper into CVT, its results, and the characterisation of the samples used in this thesis project.

In Chemical Vapour Transport, popularized by Schäfer [106], the solid phase of two or more precursors are subjected to increased temperatures until they become volatile and susceptible to react and diffuse in the gaseous state. Usually, a mix of the precursors in the shape of polycrystalline powder is placed inside one extreme of a quartz tube in which the air content has been replaced with a vapour transport agent at low pressure and carefully sealed; these quartz tubes

are introduced into a horizontal tubular furnace with decoupled heating heads that induce a temperature gradient with the higher temperature at the end of the tube containing the precursors (see figure 2.1). Once the precursors evaporate, they are transported to the cold head of the quartz tube and nucleate at the surface close to the cold end of tube in the case of endothermic reactions (as in Cu_2OSeO_3) or viceversa if the chemical reaction is exothermic. In order to optimise the size and quality of the samples, one must tune the temperature at both ends of the tube, the time length of the heating and cooling process, the pressure of the gaseous transport agent and the size of the quartz tube [107].

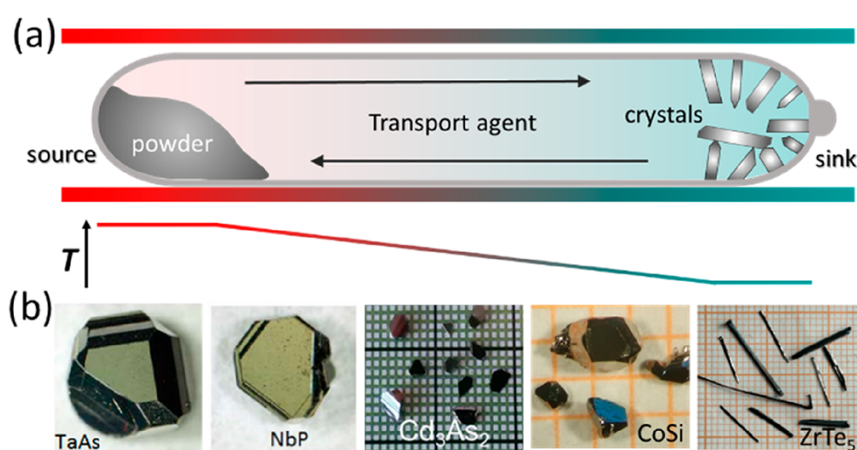


Figure 2.1: a) Illustration of the Chemical Vapour Transport principle consisting on a temperature gradient applied upon a sealed quartz tube containing mixed precursors, a gaseous transport agent and a nucleation site at the sink, and b) typical samples obtained using this method (image taken from [107]).

As early as in 1976, the CVT method was utilised by Meunier to synthesise single crystals of the $\text{Cu}_x\text{O}(\text{SeO}_3)_{x-1}$ family of compounds, starting with Cu_2OSeO_3 powder synthesised by a solid state reaction of CuO and SeO_2 in a 2:1 molar ratio, and with a final outcome depending strongly on the temperatures imposed to the ends of the quartz tube [70–72, 108]. In order to avoid polycrystalline samples and increase the size of the Cu_2OSeO_3 single crystals, Panela *et al.* added seed crystals at the sink side of the quartz tube to induce the nucleation of crystals [109]. The samples used in this thesis project were grown by our collaborators at the School of Chemistry of the University of Auckland mixing 0.511 g of CuO (Achtung Chempur 99.99%), 0.489 g of SeO_2 (Sigma Aldrich 99.99%) and 0.030 g

of NH_4Cl (Analar BDH 99.5%) as transport agent into a quartz tube of approximately 10 cm of length evacuated and sealed with an H_2/O_2 flame, and baking the mix the mix at a source temperature of 883.15 K and a sink temperature of 813.15 K. As a result, we obtained a batch of single crystals that were rinsed with ethanol and deionised water.

2.1.1 Sample characterisation

Symmetry	Space group	Lattice constant (\AA)	T (K)	Reference
Cubic	$P2_13$	8.925	300	[110]
Cubic	$P2_13$	8.92082(17)	300.0(1)	[76]
Cubic	$P2_13$ or $P4_232$	8.928(3)	~ 300	[70]
Cubic	$P2_13$	8.925	~ 300	[71]
Cubic	$P2_13$	8.91113(1)	10	[72]

Table 2.1: A comparison of the parameters of the unit cell of the single crystal Cu_2OSeO_3 samples used in this thesis (first two lines), which were grown by R. Rov, L. Camacho and T. Soehnel at the U. of Auckland (Rietveld refinement details in [110] and [76]) with data from different studies confirms the cubic structure with space group $P2_13$ (number 198 in [68]) and shows a strong agreement on the lattice parameter at room temperature.

Since different crystallographic phases of a CuO-SeO_2 system may appear upon Chemical Vapour Transport, it is essential to distinguish CuOSe_3 , Cu_2OSeO_3 and $\text{Cu}_4\text{O}(\text{SeO}_3)_3$, which result from CuO-SeO_2 molar ratios of 1:1, 2:1, and 4/3:1, respectively. A careful selection of the temperature settings at both ends of the furnace followed by X-ray Diffraction (XRD) of single crystals crushed to powder has allowed the identification of the sink temperatures at which the different phases appear: Cu_2OSeO_3 is stable for $T_{\text{sink}} \leq 854.65$ K, $\text{Cu}_4\text{O}(\text{SeO}_3)_3$ below 800.45 K, and CuSeO_3 below 774.85 K [109]. The lattice parameters obtained from the X-rays analysis of Cu_2OSeO_3 are summarised in table 2.1.

Moreover, we performed neutron Laue diffraction to confirm the space group of the selected samples (more about neutron Laue diffraction in section 2.3). figure

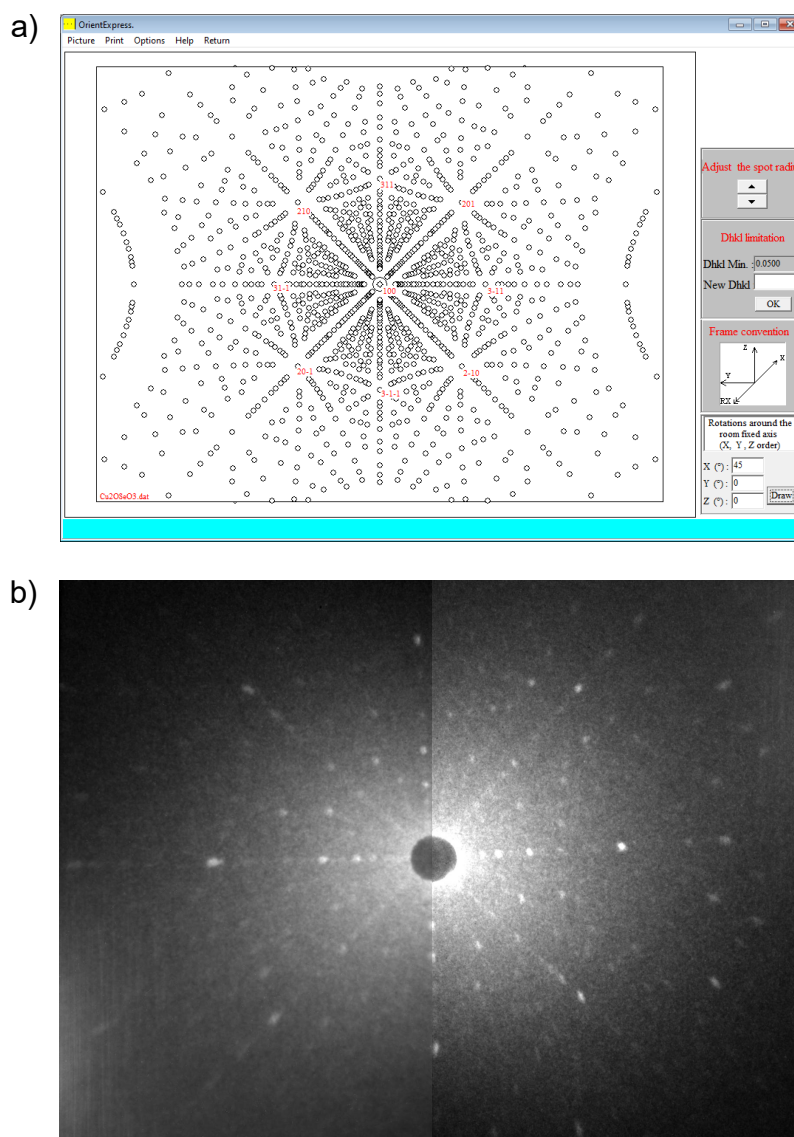


Figure 2.2: Neutron Laue diffraction on single crystal Cu_2OSeO_3 as a proof of crystallographic symmetry and alignment. Panel a) shows a pattern simulated using the space symmetry group $P2_13$ as the input of Orient Express[®] with the neutron beam parallel to the crystallographic $\langle 100 \rangle$ axis, and Panel b) shows the experimental pattern acquired with JOEY at ANSTO [111].

2.2 shows (top panel) a selected diffraction pattern acquired at room temperature and (bottom panel) a pattern simulated by the Orient Express[®] 3.4 software package using the crystallographic unit cell data as an input [111]. The agreement between the measured and predicted patterns confirms the lattices parameters of the Cu_2OSeO_3 single crystal used for our studies, although small differences arise from limitations in the software in a) calculating the scattering intensities of the

observed Bragg peaks based on the scattering length of the elements in the unit cell at well known coordinates, b) considering the geometry of the crystal used, which distorts the size of the observed peaks, and c) to consider the three dimensional geometry of the neutron detector.

2.2 Neutrons scattering

Given the wave-like properties of neutrons, electrons and photons, these particles can be used for scattering applications, in particular when their wavelengths are similar to the spacial interatomic distance in solids [31, 112–115]. This requirement will set constrains to the range of kinetic energies desired for a beam of these elementary particles (see table 2.2). In the following paragraphs, the concepts of neutron sources, detectors and optical equipment, magnetic and non-magnetic small angle neutron scattering instrumentation, data collection and data treatment will be discussed in greater detail.

Property	Neutrons	Electrons	Photons
Wavelength λ (nm)	$0.028/\sqrt{E(\text{eV})}$	$1.2/\sqrt{E(\text{eV})}$	$1240/\sqrt{E(\text{eV})}$
Energy for $\lambda = 1$ nm	10 meV	1.5 eV	1.24 KeV
Wavelength for 26 meV	0.17 nm	50 nm	100 μm
Speed for 26 meV	2.2×10^3 m/s	9.56×10^5 m/s	3×10^8 m/s
Energy resolution	5×10^{-2}	5×10^{-2}	$\times 10^{-5}$

Table 2.2: Energy requirements for scattering experiments with beams of neutrons, electrons and photons. A kinetic energy of 26 meV is chosen since it is characteristic of neutrons close to room temperature (values extracted from [116]).

2.2.1 Neutron sources

Neutrons are commonly found in nature bound to an atomic nucleus and a considerable effort must be undertaken to produce a substantial beam of neutrons since the lifetime of free neutrons is below 15 minutes. The neutron sources available can be classified in three main types: natural radioactive sources, nuclear

fission reactors and spallation sources.

1. Natural sources of radioactivity were used by Chadwick to isolate the neutron and demonstrate its existence as proposed by Rutherford [117–119]. This experiment used (α, n) reactions, and the radioactive decay of Polonium 210 into an α -particle (a Helium 4 nucleus) with a kinetic energy of 5.3 MeV and an atom of Lead 206, to bombard alpha particles onto Beryllium 9 leading to the production of Carbon 12 and free neutrons. The energy of these free neutrons follows a distribution similar to that of fission sources and is usually utilised for testing neutron detectors. Furthermore, (γ, n) sources emit neutrons upon absorption of γ -rays by a natural radioactive source.
2. Fission sources use Uranium 235, which reacts to thermal neutrons ($E = 5$ -100 meV, equivalent to a neutron temperature of 60-1000 K) by emitting 180 MeV of energy, two smaller atoms and 2.5 fast neutrons ($E = 1$ -2 MeV, equivalent to 1000-6000 K) [116, 120]. Here, the reaction rate can be controlled by inserting neutron absorbing control rods usually containing Boron. Moreover, the resulting spectrum follows a Maxwellian distribution and contains: cold ($E = 0.1$ -10 meV, equivalent to 1-120 K), thermal and fast neutrons, where the flux distribution can be tuned using a moderating material (usually liquid deuterium or hot graphite to maximise the flux of cold or hot neutrons, respectively) inside the reactor [121–123].
3. Particle accelerator sources can produce a beam of continuous or pulsed neutrons by exciting a target with highly energetic particles. The most common methods are based on the deuterium-tritium (D,T) fusion, bremsstrahlung radiation (Bremsstrahlung) of electrons, and accelerated protons at spallation neutron sources. In (D,T) fusion sources, positively charged deuterium ions are accelerated to bombard tritium-enriched targets that produce a continuous neutron beam with a kinetic energy of 14.1 MeV; these sources are usually used in small laboratory setups. Electron accelerators may be used to shoot electrons at targets in which the binding energy of the innermost neutron is lower than the energy of the γ -rays produced by the deceleration

of electrons hitting the target; these sources usually yield pulsed neutron beams with an energy of ~ 150 MeV and a frequency of 25-250 Hz. At spallation sources, a beam of protons with an energy of 5-15 MeV (although different beams could also induce spallation processes) impacts heavy atom targets and starts an inter-nuclear cascade followed by the release of low energy neutrons during the evaporation process; these sources usually produce 20-30 neutrons per proton in a pulsed beam dominated by fast neutrons [124, 125].

2.2.2 Neutron detectors

Neutron detectors rely on nuclear reactions that release ionising radiation or charged particles and their conversion into an electric current. Here, we focus on ^3He and scintillation cameras since these are the technologies used at ANSTO. Nonetheless, a wider range of options exist [126].

1. Gas detectors consist of ionisation chambers with ^3He or $^{10}\text{BF}_3$ between two metallic plates that creates a small electric current per neutron absorbed. For example, ^3He detectors absorb a thermal neutron and produce a ^3H atom and a proton ($^3\text{He} + n \rightarrow ^3\text{H} + p + 764 \text{ KeV}$). Alternatively, proportional counters confine the gas within small cylindrical tubes with an anode along its symmetry axis, which creates a currents proportional to the number of neutrons absorbed and allow detecting single neutrons. Moreover, multi-wire proportional chambers and micro-pattern gas counters increase spacial precision [127–129].
2. Scintillator detectors contain photon-emitting neutron absorbing elements. Here the light is focused and detected through optical lenses and mirrors. Often photomultipliers or sensitive gas counters of photons, and photographic films or CCDs convert the photons into an electric pulse [130–133].

2.2.3 Neutron optics

refers to methods for focusing a neutron beam along entire facilities and individual instrument by considering the wavelike properties of neutrons (for more

information read reference [120] or section 4.4.2 of the International Tables for Crystallography [68]).

Collimators control the direction and reduce the divergence of a beam of neutrons along a narrow path. They may consist of two pinholes carved in absorbing materials and separated by a distance defined by the edges of the sample environment. Collimators are frequently used in SANS experiments with pinholes drilled from Cadmium or Gadolinium thin foils that quench parasitic scattering induced by diffraction at the edge of the slits [134–136].

Monochromators take advantage of Bragg's law to select a narrow region of neutron energies from a polychromatic neutron flux diffracted from either mosaic or high quality single crystals, with single crystals preferred for greater energy-selection precision. The most common used monochromators are made of pyrolytic Graphite, Copper, Silicon and Germanium [137, 138].

Neutron mirrors are usually used as neutron guides to distribute the neutron flux in large facilities. Non-magnetic materials with a smooth surface may enable the total internal reflection of neutron waves below a critical angle. For example, Nickel with a critical angle of 0.1 degrees usually leads to neutron mirrors with a long focal length on grazing incidence mode [139].

Neutron filters suppress high energy neutrons or gamma radiation from the primary beam, and remove neutrons affected by high order diffraction from the secondary beam. Hence, neutron filters are selected taking into consideration the energy dependence of the neutron scattering cross section, which can be divided in an absorption term, a temperature dependent term and a third term that depends on the orientation of the crystalline structure of the filter. The most frequently used filter materials are Beryllium and pyrolytic Graphite [140, 141].

Neutron choppers and velocity selectors select neutrons depending on their speed, with pulsed and continuous beams coming out of neutron choppers and velocity selectors, respectively. In both, neutron absorbing parts rotate parallel to

the direction of the primary neutron beam, with neutron choppers consisting of rotating disks and velocity selectors made of curved layers [142–145].

2.2.4 Nuclear and magnetic scattering of neutrons

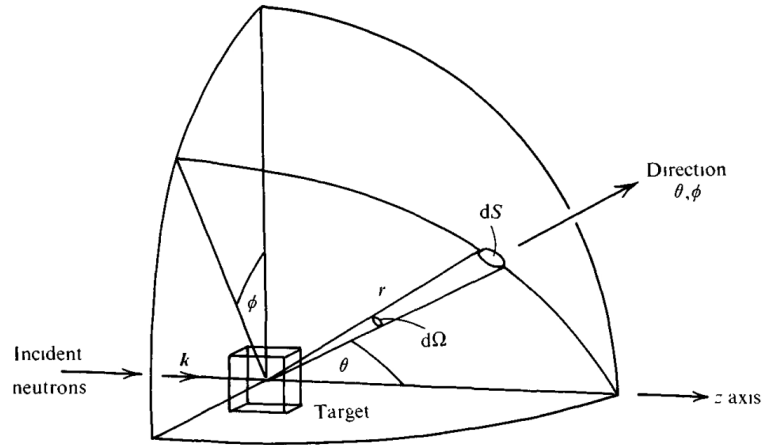


Figure 2.3: Typical neutron scattering geometry (image taken from [122]).

Neutrons interact with matter through two channels: (1) with atomic nuclei via the strong force in the fm length scale, and (2) with magnetic moments via dipolar interactions. When a neutron beam hits a target, they can pass through (transmission), merge with an ion (absorption) or deflect (scattering). The scattering geometry is defined in terms of polar spherical coordinates (see figure 2.3) with the target sample at the origin, the incident neutron beam parallel to the z -axis, and a small neutron detector with an area dS placed at a distance r away from the sample at a polar angle θ , an azimuthal angle ϕ , and solid angle $d\Omega$. Here, the incident flux of neutrons, Φ , is given by the number of neutrons per second passing through an unit area perpendicular to the z -axis. Thus, the partial differential scattering cross section is determined by eq. 2.1:

$$\frac{\partial^2 \sigma}{\partial \Omega \partial E'} = \frac{\text{neutrons detected per second with an energy } E' < E < E + dE'}{\Phi \partial \Omega \partial E'} \quad (2.1)$$

We can integrate over the entire range of energies in eq. 2.1 to obtain the differential cross-section, $d\sigma/d\Omega$:

$$\frac{d\sigma}{d\Omega} = \int_0^\infty \left(\frac{\partial^2 \sigma}{\partial \Omega \partial E'} \right) dE' = \frac{\text{neutrons detected per second}}{\Phi d\Omega} \quad (2.2)$$

$d\sigma/d\Omega$ can also be integrated along all angles to count all the scattered neutrons detected per second, which defines the total scattering cross section, σ_{tot} :

$$\sigma_{tot} = \int_{\text{all directions}} \frac{d\sigma}{d\Omega} d\Omega \quad (2.3)$$

Let us consider monochromatic neutron beam described by a free particle wave-function along the z -axis ($\psi_{inc} = \exp(ikz)$, with magnitude of the wave-vector, k) irradiates a single fixed nucleus (see figure 2.4). A fixed target exchanges no kinetic energy with a beam of thermal neutrons since the beam energy is not enough to excite the target. Moreover, the incident beam consists of plane waves since the wavelength of thermal neutrons is much larger than the range of action of the strong nuclear force, and the wave-function of the scattered neutrons is $\psi_{sc} = -(b/r)\exp(ikr)$, where the neutron scattering length, b , is a complex scalar. The imaginary component of b describes an isotope's neutron absorption. For simplicity, we will focus on isotopes with a small $\text{Im}(b)$ that allows us to treat it as a real with well tabulated values for each atomic isotope [122].

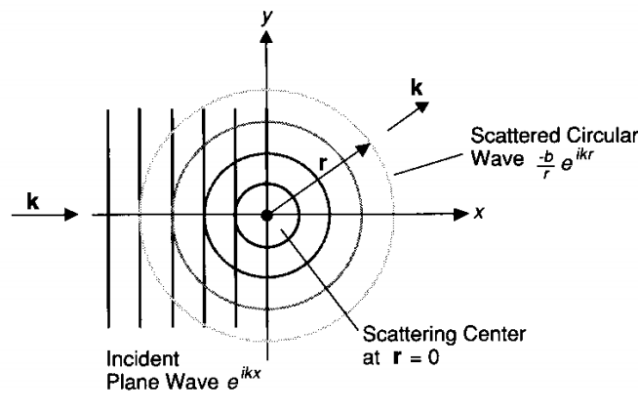


Figure 2.4: Schematic of the scattering of an incident neutron plane wave from a single fixed nucleus (image taken from [146]).

Let v be the velocity of the neutrons, then the number of neutrons detected in the area dS per second is

$$vdS|\psi_{sc}|^2 = vb^2\frac{dS}{r^2} = vb^2d\Omega \quad (2.4)$$

Using equations 2.2 to 2.3 we obtain:

$$\frac{d\sigma}{d\Omega} = \frac{vb^2d\Omega}{\Phi d\Omega} = b^2, \quad \sigma_{tot} = 4\pi b^2 \quad (2.5)$$

Nuclear neutron scattering from solids

For a single atom, the scattering cross section, σ , is the effective area in which every incident neutron would be scattered, and measures the strength of the neutron-nucleus interaction [146]. In the case of solid targets, neutrons can scatter without changing their energy in what we call elastic neutron scattering, or they can gain/loss energy via inelastic neutron scattering [147]. Since SANS was the main experimental technique used throughout this thesis, we will focus on elastic neutron scattering. In elastic neutron scattering (diffraction), the conservation of energy relates the neutron wavelength, λ , the scattering angle with respect to the incident beam, 2θ , and the scattering vector, \vec{Q} , as follows [122]:

$$|\vec{Q}| = 4\pi\frac{\sin\theta}{\lambda} \quad (2.6)$$

Moreover, scattered neutrons behave as waves and can interfere constructively or destructively; in other words, the scattered neutrons will be detected when they are in phase. Bragg's law gives the condition for constructive interference:

$$n\lambda = 2d\sin\theta \quad (2.7)$$

where n is gives the order of the observed scattering peaks, d is the periodic distance between atomic planes. Consequently, the lattice geometry defines the diffraction pattern and its symmetries. Furthermore, the intensity of the Bragg peaks can be used to locate individual elements within the unit cell.

Neutron scattering on periodic magnetic lattices can produce Bragg peaks [5, 9, 148–152]. As in the case of nuclear scattering of neutrons, the magnetic diffraction patterns provide information about the periodicity and geometry of the modulations of the magnetic moment of unpaired electrons. Small Angle Neutron

Scattering (SANS) instruments minimise the scattering angles and maximise the neutron wavelength to study structures such as magnetically ordered states with a periodicity of 1-100 Å, such as spin density waves or skyrmions, which were first observed with SANS in MnSi (see figure 2.5) [9].

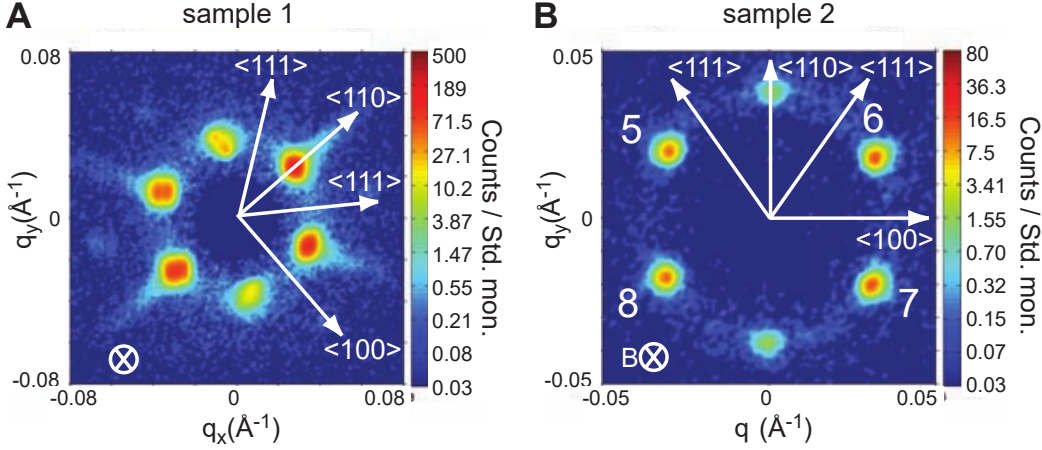


Figure 2.5: First SANS spectra from a skyrmion lattice by Müelbauer *et al.* [9]. The patterns acquired of a) sample 1 and b) sample 2 exhibit the 6-fold symmetry of a 2D hexagonal skyrmions lattice (image taken from [9]).

Let us define the differential scattering cross section of equation 2.1 in terms of the incident neutrons flux, Φ , which has units of number of neutrons per unit area per second. Here, the detector has solid angle of $\partial\Omega$, an efficiency, η , and detects neutrons at a rate, C , within a given energy range $\partial E'$, from a sample with N identical atoms. Thus [153]:

$$\frac{\partial^2\sigma}{\partial\Omega\partial E'} = \frac{C}{\eta\Phi N\partial\Omega\partial E'} \quad (2.8)$$

where, N relates to individual atoms in the case of nuclear neutron scattering or the unpaired spin of magnetic ions in the case of magnetic neutron scattering. Moreover, using equations 2.2 and 2.8, we get the total number of neutrons scattered through a solid angle $d\Omega$:

$$\frac{d\sigma}{d\Omega} = \frac{C}{\eta\Phi N\partial\Omega} \quad (2.9)$$

Likewise, the number of neutrons scattered from a solid at all angles, σ_{tot} is:

$$\sigma_{tot} = \frac{C}{\eta\Phi N} \quad (2.10)$$

In equations 2.8, 2.9, and 2.10, the count rate C is of great experimental relevance and can also be estimated from first principles. Hence, let us define the neutron scattering cross section $(d\sigma/d\Omega)|_{\vec{k}_0, \vec{\sigma}_0, \lambda_0 \rightarrow \vec{k}_1, \vec{\sigma}_1, \lambda_1}$ for neutrons with an initial state characterised by a wave vector \vec{k}_0 and spin polarisation $\vec{\sigma}_0$, and a final state with wave vector \vec{k}_1 and polarisation $\vec{\sigma}_1$, while the sample makes a transition from a state λ_0 to a state λ_1 [122, 154–156]:

$$\frac{d\sigma}{d\Omega} \Big|_{\vec{k}_0, \vec{\sigma}_0, \lambda_0 \rightarrow \vec{k}_1, \vec{\sigma}_1, \lambda_1} = \frac{1}{N\Phi d\Omega} \sum_{k_1} W_{\vec{k}_0, \vec{\sigma}_0, \lambda_0 \rightarrow \vec{k}_1, \vec{\sigma}_1, \lambda_1} \quad (2.11)$$

where $W_{\vec{k}_0, \vec{\sigma}_0, \lambda_0 \rightarrow \vec{k}_1, \vec{\sigma}_1, \lambda_1}$ describes the transition rate of the neutron-sample system from the initial state $\vec{k}_0, \vec{\sigma}_0, \lambda_0$ to $\vec{k}_1, \vec{\sigma}_1, \lambda_1$, and the sum is constrained to those propagation vectors \vec{k}_1 that point towards the detector solid angle $d\Omega$. To evaluate the right-hand side of equation 2.11, we introduce Fermi's golden rule, which defines the probability of a transition due to a periodic perturbation using first order time-dependent perturbation theory [157–160]:

$$W_{\vec{k}_0, \vec{\sigma}_0, \lambda_0 \rightarrow \vec{k}_1, \vec{\sigma}_1, \lambda_1} = \frac{2\pi}{\hbar} \left| \langle \vec{k}_1, \vec{\sigma}_1, \lambda_1 | \hat{V} | \vec{k}_0, \vec{\sigma}_0, \lambda_0 \rangle \right|^2 \rho_{\vec{k}_1, \vec{\sigma}_1} \quad (2.12)$$

with \hat{V} as the neutron-sample interaction potential, and $\rho_{\vec{k}_1, \vec{\sigma}_1, \lambda_1}$ as the density of scattered states with an energy E_1 . To calculate the right hand side of equation 2.12, we approximate the incident and scattered neutron wave-functions to plane waves assuming their wavelength is greater than the scattering length of the interaction, and a finite sample volume V_0 . Therefore:

$$|\vec{k}_0, \vec{\sigma}_0\rangle = V_0^{-1/2} e^{i\vec{k}_0 \cdot \vec{r}} |\vec{\sigma}_0\rangle, \quad |\vec{k}_1, \vec{\sigma}_1\rangle = V_0^{-1/2} e^{i\vec{k}_1 \cdot \vec{r}} |\vec{\sigma}_1\rangle \quad (2.13)$$

Furthermore, the energy of a plane wave particle of mass m and wave-vector \vec{k}_1 is given by $E_1 = \hbar^2 k_1^2 / 2m$, which can be differentiated on both sides to obtain an expression the energy range $dE_1 = \hbar^2 k_1 dk_1 / m$. Moreover, the product $\rho_{\vec{k}_1, \vec{\sigma}_1} dE_1$ is defined as the number of scattered neutron states contained in the solid angle $d\Omega$ with kinetic energy between E_1 and $E_1 + dE_1$, which equates to the amount of wave-vectors $k_1^2 dk_1 d\Omega$, *i.e.*:

$$\rho_{\vec{k}_1, \vec{\sigma}_1} dE_1 = \frac{V_0}{(2\pi)^3} k_1^2 dk_1 d\Omega \quad (2.14)$$

if we now divide equation 2.14 by dE_1 , we obtain:

$$\rho_{\vec{k}_1, \vec{\sigma}_1} = \frac{V_0}{(2\pi)^3} \frac{k_1 m}{\hbar^2} d\Omega \quad (2.15)$$

Considering that the flux of incident neutrons is $\Phi = v/V_0 = \hbar k_0/mV_0$, we may utilise equations 2.12, 2.13, and 2.15 into equation 2.11 to write:

$$\frac{d\sigma}{d\Omega} \Big|_{\vec{k}_0, \vec{\sigma}_0, \lambda_0 \rightarrow \vec{k}_1, \vec{\sigma}_1, \lambda_1} = \frac{1}{N} \frac{k_1}{k_0} \left(\frac{m}{2\pi\hbar^2} \right)^2 \left| \langle \vec{k}_1 \vec{\sigma}_1 \lambda_1 | \hat{V} | \vec{k}_0 \vec{\sigma}_0 \lambda_0 \rangle \right|^2 \quad (2.16)$$

which is independent of the sample size, V_0 . Moreover, the conservation of energy of the system formed by the neutrons and the sample imposes a constrain on equation 2.16. Let the initial and final energies of the sample be E_{λ_0} and E_{λ_1} , respectively, then $E = E_0 - E_1 = E_{\lambda_1} - E_{\lambda_0}$ must be fulfilled, which we model using a Dirac delta function that preserves the magnitude of the cross-section since its integrated magnitude equals one [161–164]. Thus, the neutron partial differential cross section becomes:

$$\frac{\partial^2 \sigma}{\partial \Omega \partial E} \Big|_{\vec{k}_0, \vec{\sigma}_0, \lambda_0 \rightarrow \vec{k}_1, \vec{\sigma}_1, \lambda_1} = \frac{1}{N} \frac{k_1}{k_0} \left(\frac{m}{2\pi\hbar^2} \right)^2 \left| \langle \vec{k}_1 \vec{\sigma}_1 \lambda_1 | \hat{V} | \vec{k}_0 \vec{\sigma}_0 \lambda_0 \rangle \right|^2 \delta(E + E_{\lambda_0} - E_{\lambda_1}) \quad (2.17)$$

if we now integrate over all the possible final states of the sample, λ_1 , disregard the final neutron polarisation, $\vec{\sigma}_1$, and take the average across all the possible states λ_0 and $\vec{\sigma}_0$ with probabilities p_{λ_0} and $p_{\vec{\sigma}_0}$, respectively, then:

$$\begin{aligned} \frac{\partial^2 \sigma}{\partial \Omega \partial E} \Big|_{\vec{k}_0 \rightarrow \vec{k}_1} = & \\ \frac{1}{N} \frac{k_1}{k_0} \left(\frac{m}{2\pi\hbar^2} \right)^2 \sum_{\lambda_0, \vec{\sigma}_0} p_{\lambda_0} p_{\vec{\sigma}_0} \sum_{\lambda_1, \vec{\sigma}_1} & \left| \langle \vec{k}_1 \vec{\sigma}_1 \lambda_1 | \hat{V} | \vec{k}_0 \vec{\sigma}_0 \lambda_0 \rangle \right|^2 \delta(E + E_{\lambda_0} - E_{\lambda_1}) \end{aligned} \quad (2.18)$$

which is known as the master equation for neutron scattering. Notice that all the physics is contained within the matrix element in equation 2.18. Additionally, the potential energy \hat{V} can emanate either from nuclear or magnetic interactions of the neutron with the sample. This matrix element can be expanded as:

$$\begin{aligned}
\langle \vec{k}_1 \vec{\sigma}_1 \lambda_1 | \hat{V} | \vec{k}_0 \vec{\sigma}_0 \lambda_0 \rangle &= \int \int \int \psi_{\vec{k}_1}^* \chi_{\vec{\sigma}_1}^* \phi_{\lambda_1}^* \hat{V} \psi_{\vec{k}_0} \chi_{\vec{\sigma}_0} \phi_{\lambda_0} d\lambda d\vec{R} d\vec{r} \\
&= \frac{1}{V_0} \int \int \int e^{-i\vec{k}_1 \cdot \vec{r}} \chi_{\vec{\sigma}_1}^* \phi_{\lambda_1}^* \hat{V} e^{i\vec{k}_0 \cdot \vec{r}} \chi_{\vec{\sigma}_0} \phi_{\lambda_0} d\lambda d\vec{R} d\vec{r} \\
&= \frac{1}{V_0} \int \int \int \left(\chi_{\vec{\sigma}_1}^* \phi_{\lambda_1}^* \hat{V} \chi_{\vec{\sigma}_0} \phi_{\lambda_0} \right) e^{i\vec{k} \cdot \vec{r}} d\vec{R} d\vec{r}, \quad \vec{k} = \vec{k}_0 - \vec{k}_1
\end{aligned} \tag{2.19}$$

where $d\vec{R} = \prod_{i=1}^N d\vec{R}_i$ is the product of differential volumes for each nucleus in the sample, $d\vec{r}$ is the neutron element of volume, $d\lambda$ is used to integrate over sample states, $\psi_{\vec{k}_i} \chi_{\vec{\sigma}_i}$ is a neutron wave-function, \vec{k} is the momentum transfer vector, and ϕ_{λ_i} the wave-function of a scattering element (nucleus for nuclear neutron scattering or spin of unpaired electrons for magnetic neutron scattering). Notice, equation 2.19 is the Fourier transform of $\langle \chi_{\vec{\sigma}_1} \phi_{\lambda_1} | \hat{V} | \chi_{\vec{\sigma}_0} \phi_{\lambda_0} \rangle$, hence the neutron detector provides information in reciprocal space.

Magnetic neutron scattering

The magnetic moment of electrons, $\vec{\mu}_e$, and neutrons, $\vec{\mu}_n$, are given by [35, 165–167]:

$$\begin{aligned}
\vec{\mu}_e &= -2\mu_B \vec{s}, & \mu_B &= \frac{e\hbar}{2m_e} \\
\vec{\mu}_n &= -\gamma\mu_N \vec{\sigma}, & \mu_N &= \frac{e\hbar}{2m_p}
\end{aligned} \tag{2.20}$$

where μ_B and μ_N are the Bohr- and nuclear-magneton, respectively; $\gamma = 1.913$ is a constant; m_n and m_p are the rest mass of the neutron and the proton; and the Pauli spin operators are represented by $\vec{\sigma}$ and \vec{s} . Let us consider the magnetic interaction between a neutron and an electron with momentum \vec{p} . The contribution of the magnetic moment of the electron, \vec{s} , to the total magnetic field experienced by a neutron at a displacement \vec{R} is given by

$$\vec{B}_S = \vec{\nabla} \times \vec{A}, \quad \vec{A} = \frac{\mu_0}{4\pi} \frac{\vec{\mu}_e \times \hat{R}}{R^2}, \quad \vec{R} = R\hat{R} \tag{2.21}$$

whilst the moment of the electron creates a differential current, $I d\vec{l}$, that fulfils

$$I d\vec{l} = -\frac{e\vec{p}}{m_e} = -\frac{2\mu_B \vec{p}}{\hbar} \tag{2.22}$$

which according to the Biot-Savart law induces a field

$$\vec{B}_L = \frac{\mu_0 I}{4\pi} \frac{d\vec{l} \times \hat{R}}{R^2}, \quad (2.23)$$

with some algebra we arrive to the total magnetic field:

$$\vec{B} = \vec{B}_S + \vec{B}_L = \frac{\mu_0}{4\pi} \left[\vec{\nabla} \times \left(\frac{\vec{\mu}_e \times \hat{R}}{R^2} \right) - \frac{2\mu_B}{\hbar} \frac{\vec{p} \times \hat{R}}{R^2} \right] \quad (2.24)$$

and therefore, the potential energy of a neutron in this magnetic field is

$$\hat{V} = -\vec{\mu}_n \cdot \vec{B} = \frac{\mu_0}{4\pi} \gamma \mu_N 2\mu_B \vec{\sigma} \cdot \left[\underbrace{\vec{\nabla} \times \left(\frac{\vec{s} \times \hat{R}}{R^2} \right)}_{\vec{W}_S} + \underbrace{\frac{1}{\hbar} \frac{\vec{p} \times \hat{R}}{R^2}}_{\vec{W}_L} \right] \quad (2.25)$$

with the first term between brackets coming from the spin of the electron and the second term derived from its orbital momentum. This potential operator can be plugged into equation 2.18, for which we consider separately the neutron spin and orbital contributions, and calculate first $\langle \vec{k}_1 | \hat{V} | \vec{k}_0 \rangle$

$$\langle \vec{k}_1 | \hat{W} | \vec{k}_0 \rangle = \langle \vec{k}_1 | \hat{W}_S | \vec{k}_0 \rangle + \langle \vec{k}_1 | \hat{W}_L | \vec{k}_0 \rangle \quad (2.26)$$

we obtain the i-th electron-spin contribution to this matrix element via

$$\langle \vec{k}_1 | \hat{W}_{S_i} | \vec{k}_0 \rangle = \int e^{-i\vec{k}_1 \cdot \vec{r}} \left[\vec{\nabla} \times \left(\frac{\vec{s}_i \times \hat{R}}{R^2} \right) \right] e^{i\vec{k}_0 \cdot \vec{r}} d\vec{r}, \quad (2.27)$$

and using the vector calculus relation

$$\vec{\nabla} \times \left(\frac{\vec{s} \times \hat{R}}{R^2} \right) = \frac{1}{2\pi^2} \int \hat{q} \times (\vec{s} \times \hat{q}) e^{i\vec{q} \cdot \vec{R}} d\vec{q}$$

with \vec{q} representing a vector in reciprocal space, hence

$$\langle \vec{k}_1 | \hat{W}_{S_i} | \vec{k}_0 \rangle = \frac{1}{2\pi^2} \int \int e^{-i\vec{k} \cdot \vec{r}} [\hat{q} \times (\vec{s}_i \times \hat{q})] e^{i\vec{q} \cdot \vec{r}} d\vec{q} d\vec{r}, \quad \vec{k} = \vec{k}_0 - \vec{k}_1 \quad (2.28)$$

if we now consider that the position in the reference frame of the neutron, \vec{r} , relates to the position of the i-th electron, \vec{r}_i , and the origin of the laboratory reference frame, \vec{R} , via $\vec{r} = \vec{r}_i + d\vec{R}$, and change variables to integrate over \vec{R} , then:

$$\int e^{i(\vec{k} + \vec{q}) \cdot \vec{R}} d\vec{R} = (2\pi)^3 \delta(\vec{k} + \vec{q}), \quad (2.29)$$

which leads to

$$\langle \vec{k}_1 | \hat{W}_{S_i} | \vec{k}_0 \rangle = 4\pi e^{i\vec{k} \cdot \vec{R}} [\hat{\kappa} \times (\vec{s}_i \times \hat{\kappa})] \quad (2.30)$$

A similar treatment can be applied to determine the contribution of the i -th electron orbital:

$$\langle \vec{k}_1 | \hat{W}_{L_i} | \vec{k}_0 \rangle = \frac{1}{\hbar} \int e^{i\vec{k} \cdot \vec{r}} \left(\frac{\vec{p}_i \times \hat{R}}{R^2} \right) d\vec{r} \quad (2.31)$$

which can be solved utilising the following vector calculus identity:

$$\int e^{i\vec{k} \cdot \vec{r}} \left(\frac{\hat{R}}{R^2} \right) d\vec{R} = 4i\pi \frac{\hat{\kappa}}{\kappa}, \quad (2.32)$$

and the fact that $[(\vec{p}_i \times \hat{\kappa}), (\vec{\kappa} \cdot \hat{r}_i)] = 0$. Therefore

$$\begin{aligned} \langle \vec{k}_1 | \hat{W}_{L_i} | \vec{k}_0 \rangle &= \frac{1}{\hbar} e^{i\vec{k} \cdot \vec{r}_i} \int e^{i\vec{k} \cdot \vec{R}} \left(\frac{\vec{p}_i \times \hat{R}}{R^2} \right) d\vec{R} \\ &= \frac{4i\pi}{\hbar\kappa} e^{i\vec{k} \cdot \vec{r}_i} (\vec{p}_i \times \hat{\kappa}) \end{aligned} \quad (2.33)$$

Consequently, we can write the partial differential cross section of equation 2.18 in terms of the potential due to all the electrons in the sample using equations 2.25, 2.30, 2.33, and approximating the proton mass to the neutron mass:

$$\begin{aligned} \left. \frac{\partial^2 \sigma}{\partial \Omega \partial E} \right|_{\vec{k}_0 \rightarrow \vec{k}_1} &= (\gamma r_0)^2 \frac{k_1}{Nk_0} \left| \langle \vec{\sigma}_1 \lambda_1 | \left(\sum_i \langle \vec{k}_1 | \vec{\sigma} \cdot \hat{W}_i | \vec{k}_0 \rangle \right) | \vec{\sigma}_0 \lambda_0 \rangle \right|^2 \delta(E + E_{\lambda_0} - E_{\lambda_1}) \\ &= (\gamma r_0)^2 \frac{k_1}{Nk_0} |\langle \vec{\sigma}_1 \lambda_1 | \vec{\sigma} \cdot \hat{Q}_\perp | \vec{\sigma}_0 \lambda_0 \rangle|^2 \delta(E + E_{\lambda_0} - E_{\lambda_1}) \end{aligned} \quad (2.34)$$

where r_0 and \hat{Q}_\perp are:

$$r_0 = \frac{\mu_0 e^2}{4\pi m_e} \approx 2.818 \text{ fm}, \quad \hat{Q}_\perp = \sum_i e^{i\vec{k} \cdot \vec{r}_i} \left[\hat{\kappa} \times (\vec{s}_i \times \hat{\kappa}) + \frac{i}{\hbar Q} (\vec{p}_i \times \hat{\kappa}) \right], \quad (2.35)$$

the constant r_0 is known as the classical electron radius and \hat{Q}_\perp is an operator related to the magnetisation of the sample. We should also notice the magnetic

differential cross section is more complicated than its nuclear scattering counterpart. This difference occurs because the nuclear interactions are central forces, but the dipole-dipole and dipole-current interactions are not [168–171].

A full-length demonstration of the relation between the magnetisation of the sample and the operator \hat{Q}_\perp is out of the scope of this thesis, whose details are extensively discussed in references [122, 172]. Nonetheless, we are able to consider the \hat{Q}_\perp operator as a linear combination of two components: one due to the spin-spin interaction and a second term arising from the spin-current force. Let $\hat{M}_S(\vec{r})$ and $\hat{M}_L(\vec{r})$ be the spin- and orbital magnetisation operators, with Fourier transforms $\hat{M}_S(\vec{k})$ and $\hat{M}_L(\vec{k})$, respectively. Then, \hat{Q}_\perp fulfils

$$\begin{aligned}\hat{Q}_\perp &= \hat{Q}_{\perp_S} + \hat{Q}_{\perp_L} = -\frac{1}{2\mu_B} \hat{k} \times \{[\hat{M}_S(\vec{k}) + \hat{M}_L(\vec{k})] \times \hat{k}\} \\ &= \vec{k} \times (\hat{Q} \times \vec{k}), \quad \hat{Q} = -\frac{\hat{M}_S + \hat{M}_L}{2\mu_B}\end{aligned}\tag{2.36}$$

which proves that \hat{Q}_\perp is the projection of \hat{Q} onto a line orthogonal to the vectors \vec{k} and $\hat{Q} \times \hat{k}$. Hence, \hat{Q}_\perp is the perpendicular component of the spin contributions with respect to the scattering vector \hat{Q} , which allows us to directly determine the direction of the spins. For example, if $\hat{M}(\vec{r}) = \hat{M}_S(\vec{r}) + \hat{M}_L(\vec{r})$ points in the same direction as the incident neutron beam, then we would observe no magnetic scattering, which is not the case for nuclear neutron scattering. Moreover, \hat{Q} is the Fourier transform of the total magnetisation of the sample due to spin and orbital motion. A time dependent version of the differential cross section can be obtained if we consider the following relations that arise from the definition of the Dirac delta function and the action of the time evolution quantum operator on the states of the scattering system:

$$\begin{aligned}\delta(E + E_{\lambda_0} - E_{\lambda_1}) &= \frac{1}{2\pi\hbar} \int_{-\infty}^{\infty} \exp\left[\frac{i(E_{\lambda_1} - E_{\lambda_0})t}{\hbar}\right] \exp(-iEt/\hbar) \\ &\quad \exp(-i\hat{H}t/\hbar)|\lambda_0\rangle = \exp(-iEt/\hbar)|\lambda_0\rangle\end{aligned}\tag{2.37}$$

Therefore, it is possible to prove that the time-dependent differential cross section can be written in a general form as:

$$\left. \frac{\partial^2 \sigma}{\partial \Omega \partial E} \right|_{\vec{k}_0 \rightarrow \vec{k}_1} = \frac{(\gamma r_0)^2}{2\pi \hbar} \frac{k_1}{Nk_0} \sum_{\alpha, \beta} (\delta_{\alpha\beta} - \kappa_\alpha \kappa_\beta) \int \langle Q_\alpha(-\vec{k}, 0) Q_\beta(\vec{k}, t) \rangle \exp(-iEt/\hbar) dt, \quad (2.38)$$

with $Q_\beta(\vec{k}, t)$ defined as

$$Q_\beta(\vec{k}, t) = \exp(i\hat{H}t/\hbar) Q_\beta(\vec{k}) \exp(-i\hat{H}t/\hbar), \quad (2.39)$$

which is the β component of the \hat{Q} operator defined in equation 2.36. Furthermore, a general expression for the elastic case of 2.38 is obtained by the thermal mean of the matrix elements in the differential cross section at the limit of long times ($t \rightarrow \infty$), and integrate over time and energy. The time-independent elastic cross section is then:

$$\left(\frac{d\sigma}{d\Omega} \right)_{el} = (\gamma r_0)^2 \sum_{\alpha, \beta} (\delta_{\alpha\beta} - \kappa_\alpha \kappa_\beta) \langle Q_\alpha(-\vec{k}) \rangle \langle Q_\beta(\vec{k}) \rangle \quad (2.40)$$

Notice, equation 2.38 contains the Fourier transform of the time-evolution of the correlation of spins in the sample, whereas equation 2.40 is its time independent equivalent. Hence, neutrons measure the influence of magnetic moments in the sample across both short- and long-range [173–175].

2.2.5 QUOKKA: the Small Angle Neutron Scattering instrument

The Small-Angle Neutron Scattering (SANS) experiments of my thesis project were performed at the instrument QUOKKA in the Australian Centre for Neutron Science (ACNS) of the Australian Nuclear Science and Technology Organisation (ANSTO) [176–178]. This instrument is attached to the cold neutron guide-line CG1 of the OPAL research reactor.

QUOKKA is inspired by instrument D22 at ILL and the SANS instrument at NIST, which entails it was built to have time-resolved capacities and host a large sample environment area. The instrument has a total length of about 40 meters, with up to 20 meters between the velocity selector and the sample and 20 meters between the sample and the neutron detector (see figure 2.6). The cold neutrons produced by the 20 MW OPAL reactor travel through the neutron guide and enter a Lead-bunkered mechanical velocity selector that enables choosing neutron

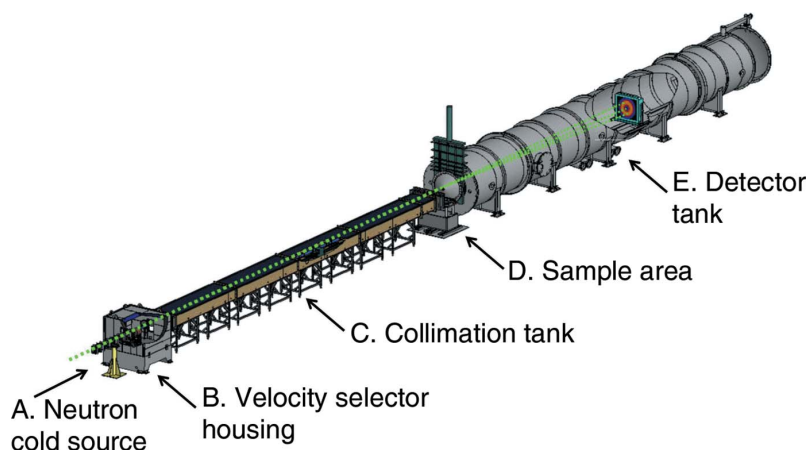


Figure 2.6: The instrument QUOKKA at ANSTO (image taken from [176]).

wavelengths between 4.5 and 43 Å. Once the neutrons pass the velocity selector, they arrive at the beam monitor, and a fast shutter before reaching the space in which a double disk chopper may be placed to perform time resolved measurements with sub-millisecond resolution. Between the fast shutter and the sample area, there is space for a collimation system, a neutron polarisation system based on a polarising mirror and radio-frequency spin flipper followed by a neutron guide with vertically-aligned permanent magnets to retain the neutron spin polarisation before they irradiate the sample. The collimation system also contains a motorised pinhole stage to select among different beam apertures to optimise the signal to noise ratio.

At the sample stage, there is approximately 1.20 meters of distance between the collimation and detector systems, in which the motorised sample stage and a goniometer support a sample environment of up to 1000 Kg of weight. Here, a set of cryostats, furnaces, magnets, electric field systems, optical stages and more are available upon contacting the sample environment team at ANSTO [179]. Moreover, a flux of more than 10^7 neutrons per square centimetre per second has been measured at the sample location of QUOKKA, which is comparable to the SANS instruments with the largest flux in the world.

The scattered neutrons enter into the 20 meters long vessel that contains a ^3He proportional neutron counter. The sample to detector distance can be varied from about 1 to 20 meters. Moreover, the position-sensitive detector of QUOKKA has an area of 1 m² with a spatial resolution of 5 mm and spans a reciprocal space

range between 0.0008 and 1.3 \AA^{-1} , making the instrument suitable to investigate phenomena in polymers, proteins, biological, chemical and magnetic samples.

Software: The instrument QUOKKA at ANSTO is controlled via the SINC Instrument Control Software (SICS), which is a client-server system written in C for UNIX computers at the spallation neutron source (SINQ) of the Paul Scherrer Institute (PSI) [180]. The original SICS software uses POSIX compliant system calls, which allowed its adaptation at ANSTO. Here, the SICS server runs on a Scientific Linux virtual machine and provides an interface to configure and control the instruments, accumulate and store data in the Hierarchical Data Format (HDF) version 5 – an open source file format developed by the HDF Group to store metadata and compressed n-dimensional data in the same file [181–183].

Variable	Value	Description	State
Sample	ask*	≥ 1 raw data files	checked
Background	–	blocked beam scan	–
Empty cell	PM_data.nx.hdf	PM phase pattern	checked
Sensitivity	sens_kt_12m.nx.hdf	detector calibration	checked
Absolute	–	intensity scaling	–
Mask	–	data analysis mask	–
Average	AVTYPE=QxQy_ASCII	Protocol type	checked

Table 2.3: Example of the parameters to build a SANS data reduction protocols in Igor. The result of this simple configuration is one or more reduced data text files that contains the reduced neutron scattering intensity for each pixel in the detector of QUOKKA.

ANSTO users interact with the SICS server using two main client options: a JavaScript Open Notation interface, and a graphical command line interface. The open source SICS client GumTree provides users an intuitive Graphical User Interface to interact with neutron and X-rays instruments [184, 185]. Our research group opted to use the graphical SICS command line interface, which enables users to write single commands or to read them from Python scripts. Both SICS

*The option "ask" lets the user select a list of raw data file names from a customisable drop-down list or writing a comma-separated list.

and GumTree enable users to accumulate data setting time limits for each measurement, alternatively, the beam monitor or detected neutron counts may be use, or a logical combination of all these options. A Python script can generates all the SICS commands to instruct QUOKKA to measure a complex phase diagram with less than 100 lines of code (available upon reasonable request). Unless explicitly stated, our SANS measurements were performed using a counting time limit of 60 to 90 seconds per file, which is possible with intense scattering signals.

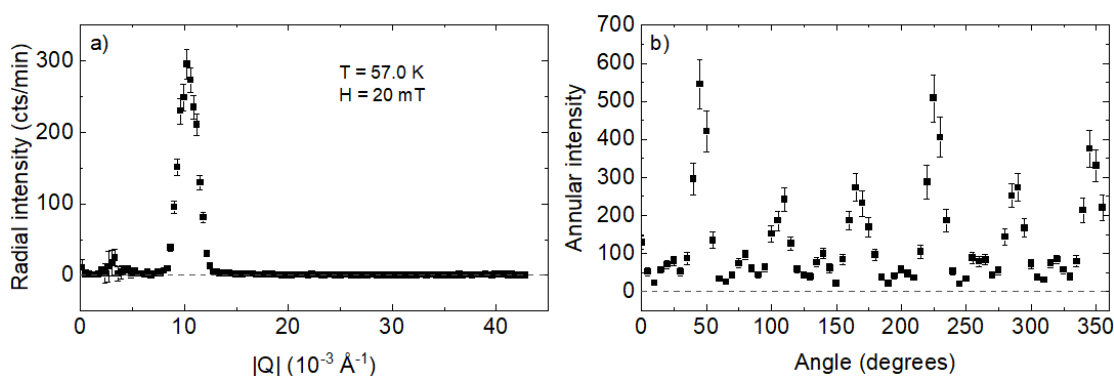


Figure 2.7: Example of the result of reducing raw neutron data using custom annular and radial integration protocols in Igor Pro with the ANSTO macros enabled. Data obtained from the first random orientated sample at $T = 57.0 \text{ K}$ and $H = 20 \text{ mT}$ (see discussion in section 3.2).

The raw data from QUOKKA are processed considering the detector sensitivity calibration and other parameters using ANSTO's SANS data reduction macros (based on NIST SANS and USANS macros, but need small modifications to be compatible with the latest versions of Igor) for the IGOR Pro software[†] to correct, reduce and perform analysis of data from QUOKKA [186–188]. For example, the scattering intensity contained in the HDF5 raw data files can be converted into generic text files (.DAT) using the parameters shown in table 2.3 in the "Build Protocol" option from the "Reduction" macro [189], and the outcome can be obtained in terms of radial intensity (neutron scattering intensity vs $|\vec{Q}|$) or annular intensity (neutron scattering intensity vs polar angle) as it is exemplified in figure 2.7.

[†]Igor Pro ® is maintained and distributed by WaveMetrics Inc. Portland, OR, USA

2.3 Sample alignment

Neutron Laue Diffraction can be used to characterise and align solids along different symmetry axes. Bragg's law (see equation 2.7) dictates how a plane of ions induces the constructive interference of scattered neutrons. Hence, a white beam of neutrons maximises the number of Bragg peaks observed at the detector. Moreover, this method can be compared to X-rays Laue diffraction: neutrons are sensitive to all elements and distinguish between different isotopes, whereas X-rays offer little sensitivity for light elements since the scattering length of X-rays increases with an increasing atomic number Z . In contrast to x-ray scattering, the entire sample can be investigated due to the large penetration depth of neutrons. This allows to determine the sample quality (domain structure, twinning, inclusions, etc.) directly [113, 115, 116, 156, 190].

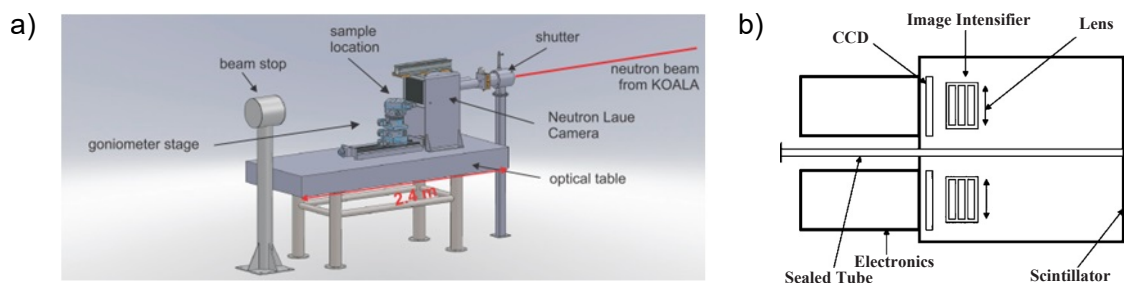


Figure 2.8: Geometry of a) the neutron Laue camera JOEY, and b) its neutron detector (images taken from [191], and [111]).

JOEY was built at ANSTO in 2013 and inspired by Orient Express at the Institute Laue-Langevin (ILL) [111, 192]. These two instruments also inspired the design of FALCON at BER-II reactor of the HZB in Berlin [191, 193]. JOEY was placed in line with two other instruments: KOWARI and PELICAN, which implies the neutron flux at JOEY is susceptible to receive a small neutron flux depending on the sample environment and the beam aperture used at KOWARI and PELICAN. The speed at which a diffraction pattern can be obtained at JOEY is determined by the neutron flux, the size of the sample and its element content, the beam aperture used at JOEY.

The setup of JOEY (see panel a) of figure 2.8) starts with a shutter and pin-hole that control the incident neutron beam and its diameter. Next, the neutrons pass through a sealed tube between the two halves of the detector and reach

the sample location from which backscattered neutrons impinge the detector and transmitted neutrons hit a beam stop at the end of the setup. The detector built by Photonic Science Ltd. consists of a neutron scintillator that absorbs neutrons and emits scintillation light, twin CCD cameras behind two image intensifiers and optical lenses (see figure 2.8b) [194, 195]. Moreover, a set of motors and a goniometer control the sample position and orientation.

To orient a single crystal with known unit cell parameters at JOEY, we start glueing the sample at the tip of a sharp sample holder at the sample stage. Once the sample position is optimised, the appropriate pinhole optimises the signal to noise ratio. The diffraction patterns are collected and optimised using the neutron detector software provided by Photonic Science Ltd. (now Scintacor), whose options include detection and removal of artifacts in the signal. The collected images are saved as TIF pictures that can be analysed using the ImageJ software developed at the National Institutes of Health (NIH) and Orient Express developed at ILL [111, 192, 196]. Notice, some regions of the diffraction image may exhibit white shadows produced by electronic noise generated by warming of the detector during long neutron exposure times [197].

The recorded diffraction patterns can be compared with simulated neutron Laue patterns using the Orient Express software, which takes as input the space group (in this case $P2_13$), the lattice constant (8.925 Å), unit cell angles (90° for Cu_2OSeO_3), the sample to detector distance (4.00 cm), neutron wavelengths (0.1 Å - 4.0 Å), a neutron beam angle (180° to indicate backscattering mode), and dimensions of the detector (height: 20.0 cm, width: 26.0 cm). An example of this simulation with the crystallographic axis $\langle 100 \rangle$ parallel to the incoming neutron beam is shown in figure 2.9. Here, a set of strong Bragg reflections (see panel b) of figure 2.2) have been highlighted in red with their reciprocal space indices. Moreover, in this example, the main diagonal contains both the [20-1] and the [201] Bragg reflections, which differ only by a propagation vector proportional to $\langle 001 \rangle$; similarly, the secondary diagonal describes the propagation vector $\langle 010 \rangle$.

Once we obtain the desired sample orientation at JOEY, the sample has to be transferred to QUOKKA. To this end, we must manually glue the sample onto a new sample holder since there is no equipment available at ANSTO to automatise

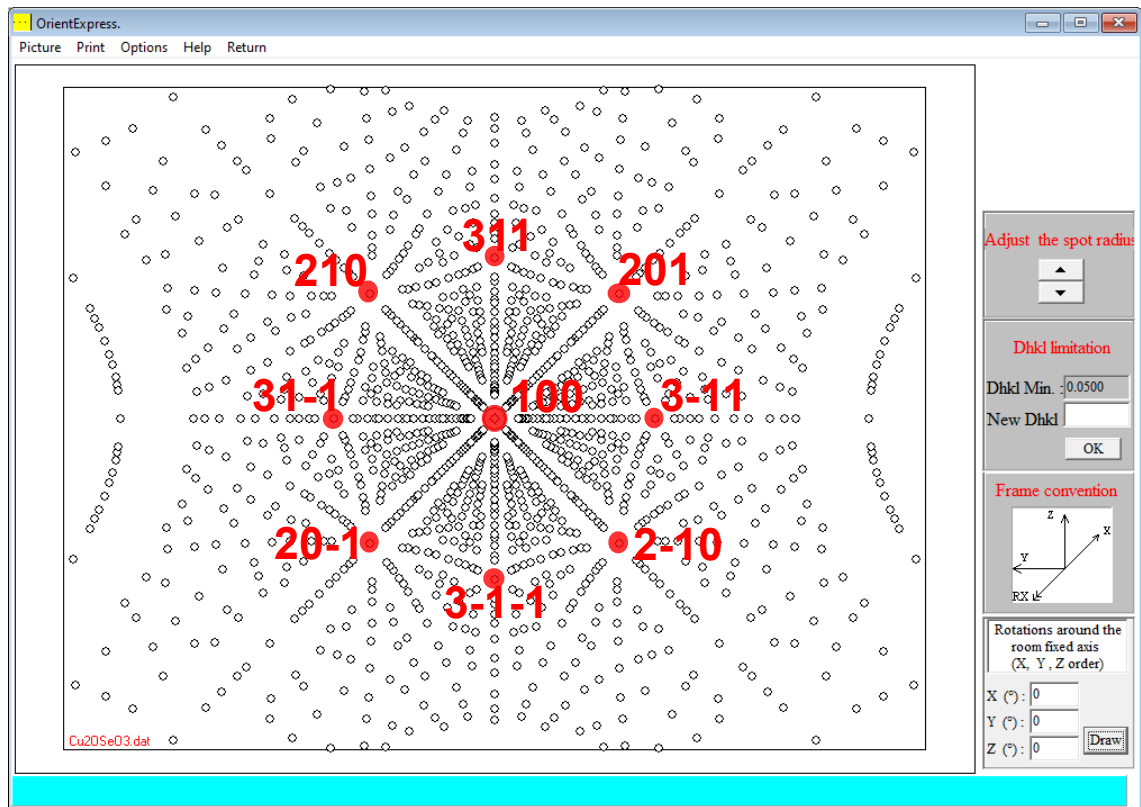


Figure 2.9: Example of neutron Laue Bragg peak indexing using the Orient Express[®] software package with the incoming neutron beam parallel to the crystallographic axis $\langle 100 \rangle$ as shown by the Bragg peak at the centre of the detector. Selected strong Bragg reflections have been highlighted in red together with their respective reciprocal space indices determined by the software using the parameters needed to describe the backscattering geometry of the instrument and the characteristics of the detector.

the sample transfer or to polish the sample maintaining the alignment obtained at JOEY. As preparation for our SANS experiments at QUOKKA, the aligned samples were glued onto an Aluminium sheet using Ge varnish [198–200], and placed under a Cadmium mask to improve the signal to noise ratio. Due to the viscosity of the varnish at room temperature, a slight pressure must be used to insert the sample into the varnish, which inevitably distorts the sample alignment by a few degrees. In order to minimise this undesired effect, it is better to glue the sample on top of its largest phases (which are perpendicular to $\langle 110 \rangle$ [109]). Alternatively, an automatic sample glueing could be obtained using a robotic arm (for example: [201]) that minimises manual imprecisions. Furthermore, comple-

mentary single crystal neutron diffraction experiments can be performed at the instruments KOALA, WOMBAT at ANSTO with greater sample environment capabilities, and a broader range in reciprocal space at KOALA and ECHIDNA or using a much larger flux of neutrons that permits the determination of weak signals at WOMBAT [202–206].

2.4 Raman scattering

When light illuminates a solid, most of it will be reflected, transmitted or absorbed. However, a small portion will be scattered elastically or inelastically, which are known as Rayleigh and Raman scattering, respectively, with the first being usually several times more intense than the second [207, 208]. The energy of inelastically scattered phonons changes through quantum mechanical interactions with elementary excitations that are created or annihilated upon photons absorption and re-emission. Thus, the energy change can be used to study the fundamental properties of excitations such as phonons, magnons or the breaking of superconducting Cooper pairs, using the energy and momentum conservation rules [209–211]:

$$\begin{aligned}\hbar\omega_i &= \hbar\omega_s \pm \hbar\omega_e \\ \vec{k}_i &= \vec{k}_s \pm \vec{q}\end{aligned}\tag{2.41}$$

Inelastic light scattering experiments are usually carried out using a beam of photons with an energy near the optical range ($E \sim 1$ eV) or synchrotron radiation sources for Inelastic X-rays Scattering ($E \sim 1$ keV) with visible photons having a wave vector of $\sim 10^{-3} \text{ \AA}^{-1}$, which is very small compared to the magnitude of typical reciprocal lattice vectors (\vec{G}). Hence, first order Raman is limited to interact with optical phonons around the centre of the Brillouin Zone.

2.4.1 Raman scattering theory: Semi-classical approach

Light waves interact with electrically charged matter and scatter inelastically from solids by changing their polarisation through dynamical excitations. The

induced polarisation per unit volume, \vec{P} , is proportional to the electric field of the incident light beam, \vec{E}_i [212]:

$$\vec{P}(\vec{r}, t) = \varepsilon_0 \chi \vec{E}_i(\vec{r}, t) \quad (2.42)$$

where ε_0 is the dielectric constant, and the electric susceptibility tensor, χ , contains contributions from collective atomic displacements. If the magnitude of the wave vector of the incident light beam is much smaller than the typical reciprocal space vectors ($|\vec{k}_i| \ll |\vec{G}|$), we use the dipole approximation and consider the magnitude of the incident electric field as constant through the unit cell:

$$\vec{E}_i(\vec{r}, t) = E_{i,0} \cos(\vec{k}_i \cdot \vec{r} - \omega_i t) \hat{e}_i \simeq E_{i,0} \cos(\omega_i t) \hat{e}_i \quad (2.43)$$

where $E_{i,0}$ is the electric field magnitude, \vec{r} a position vector, and \hat{e}_i the field polarisation. Moreover, χ we can be expressed as a Taylor series in terms of small atomic vibrations around their equilibrium positions:

$$\chi = \chi_0 + \left. \frac{\partial \chi}{\partial \vec{u}} \right|_{\vec{u}=0} \cdot \vec{u}(\vec{r}, t) + \left. \frac{\partial^2 \chi}{\partial \vec{u}^2} \right|_{\vec{u}=0} \cdot \vec{u}^2(\vec{r}, t) + \dots \quad (2.44)$$

here, $\vec{u}(\vec{r}, t) = \vec{u}_0 \cos(\vec{q} \cdot \vec{r} - \omega_p t)$, ω_p is the frequency of vibration, χ_0 is the electric susceptibility component independent of atomic oscillations, the second term contains the modulation of the susceptibility from a single vibrational mode and the n-vibrational mode terms are proportional to $\partial^n \chi / \partial \vec{u}^n$. Considering single oscillation modes and equation 2.44 into equation 2.42, we obtain:

$$\vec{P}(\vec{r}, t) = \varepsilon_0 \chi_0 \vec{E}_i(\vec{r}, t) + \varepsilon_0 \left[\left. \frac{\partial \chi}{\partial \vec{u}} \right|_{\vec{u}=0} \cdot \vec{u}(\vec{r}, t) \right] \vec{E}_i(\vec{r}, t), \quad (2.45)$$

where the applied electromagnetic radiation induces both a elastic scattering response at the same frequency, and inelastic scattering frequency-shifted oscillations. Expanding the inelastic term we get:

$$\frac{\varepsilon_0}{2} \frac{\partial \chi}{\partial \vec{u}} \cdot \vec{u}_0 \vec{E}_{i,0} \{ \cos[(\vec{k}_i + \vec{q}) \cdot \vec{r} - (\omega_i + \omega_p)t] + \cos[(\vec{k}_i - \vec{q}) \cdot \vec{r} - (\omega_i - \omega_p)t] \} \quad (2.46)$$

where the first sinusoidal term depicts the energy gain of a scattered photon through phonon annihilation (anti-Stokes), whilst the second term models the

energy loss of the scattered photon by creating a phonon (Stokes process). Figure 2.10 illustrates the resulting Raman spectrum. In general, the components of $\partial\chi/\partial\vec{u}$ are determined by the lattice and phonon symmetries. However, the product $[\partial\chi/\partial\vec{u}] \cdot \hat{u}$ defines a second-rank tensor,

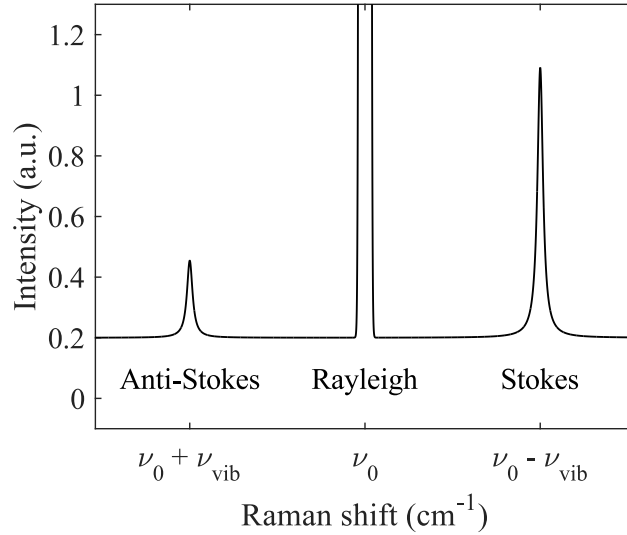


Figure 2.10: A Raman spectrum induced by incident light with frequency ν_0 contains Stokes (lose energy creating a vibrational mode with frequency ν_{vib}) and Anti-Stokes (photons gain energy by absorbing a phonon) modes.

$$R = \frac{\partial\chi}{\partial\vec{u}} \cdot \hat{u} \quad (2.47)$$

The Raman tensor, R , is used to model phonons in the unit cell. To quantify the scattering intensity, I , we start considering the radiation energy emitted over time dW_s of an oscillating dipole moment with frequency ω [213]:

$$\frac{dW_s}{d\Omega} = \frac{\omega^4}{(4\pi)^2 \epsilon_0 c^3} |\hat{e}_s \cdot \vec{P}|^2 \quad (2.48)$$

where $d\Omega$ is a differential solid angle, and \hat{e}_s the scattered light polarisation. Substituting equation 2.42 in 2.48, we get

$$\frac{dW_s}{d\Omega} = \frac{\omega^4 \epsilon_0}{(4\pi)^2 c^3} |\hat{e}_s \cdot \chi \cdot \hat{e}_i|^2 E_i^2 \quad (2.49)$$

We obtain the differential scattering cross section, $\partial^2 W_s / \partial\Omega \partial\omega$, dividing equation 2.49 by the incident energy per unit area and second, $W_i = \epsilon_0 c E_i^2$:

$$\frac{\partial^2 \sigma}{\partial \Omega \partial \omega} = \frac{1}{(4\pi)^2} \left(\frac{\omega}{c} \right)^4 |\hat{e}_s \cdot \chi \cdot \hat{e}_i|^2 \quad (2.50)$$

The Raman scattering intensity, I , is thus directly proportional to the differential cross section and depends on the incident and scattered polarisations:

$$I \sim |\hat{e}_s \cdot \chi \cdot \hat{e}_i|^2 \quad (2.51)$$

2.4.2 Quantum mechanical approach

The semi-classical approach fails explaining the strong signal enhancement that occurs when the energy of the incident photons matches the energy gap between real electronic states in the material, a condition known as Resonant Raman Scattering. The following Hamiltonian describes the Raman interaction [209]:

$$\hat{H} = \hat{H}_e + \hat{H}_i + \hat{H}_p + \hat{H}_{ei} + \hat{H}_{ep} + \hat{H}_{ip} \quad (2.52)$$

which includes the unperturbed system ($\hat{H}_0 = \hat{H}_e + \hat{H}_i + \hat{H}_p$, with the Hamiltonian for the electrons, ions and photons \hat{H}_e , \hat{H}_i and \hat{H}_p), the electron-ion interaction, \hat{H}_{ei} , the electron-photon relation, \hat{H}_{ep} , and the ion-photon interaction, \hat{H}_{ip} . \hat{H}_0 is used to calculate an exact solution, while the \hat{H}_{ei} and \hat{H}_{ep} are taken as perturbations to the system, and \hat{H}_{ip} is considered negligible. A two-bands scattering process (intra-band scattering) can be described by virtual steps [214]:

1. A photon is absorbed, and creates an electron-hole pair, which are given by the initial and intermediate quantum states $|I\rangle$ and $|II\rangle$.
2. The electron (or hole) interacts with the lattice and creates or annihilates a phonon, after which the electron-hole pair is in the intermediate state, $|III\rangle$.
3. The radiative recombination of the electron-pair occurs, thus transitioning from the intermediate state $|III\rangle$ to the final state $|F\rangle$.

Due to the time reversal symmetry of fermionic processes, these three steps can vary and all possible permutations must be considered to calculate the scattering cross-section [212]. Moreover, the states $|I\rangle$ and $|F\rangle$ are identical. The transition probability for each step can be obtained using Fermi's golden rule [215]:

$$\begin{aligned}
P_{I \rightarrow II} &\sim \left| \frac{\langle II | \hat{H}_{ep} | I \rangle}{\hbar\omega_i - (E_{II} - E_I)} \right|^2 \\
P_{II \rightarrow III} &\sim \left| \frac{\langle III | \hat{H}_{ei} | II \rangle}{\hbar\omega_i - \hbar\omega_{ph} - (E_{III} - E_I)} \right|^2 \\
P_{III \rightarrow F} &\sim \left| \frac{\langle F | \hat{H}_{ep} | III \rangle}{\hbar\omega_i - \hbar\omega_{ph} - \hbar\omega_s - (E_F - E_I)} \right|^2
\end{aligned} \tag{2.53}$$

Here, $P_{a \rightarrow b}$ is the probability of a transition from state $|a\rangle$ to $|b\rangle$ with energies E_a and E_b . The energies of the incident and scattered photons are $E_i = \hbar\omega_i$ and $E_s = \hbar\omega_s$, and $E_{ph} = \hbar\omega_{ph}$ is the energy of the phonon. Notice, each step must conserve momentum, but energy conservation holds just for the whole process. Furthermore, the momentum exchange comes from the creation/annihilation of phonons. Thus, the Stokes and Anti-Stokes transition rates are:

$$P_{I \rightarrow F} = \frac{2\pi}{\hbar} \left| \frac{\langle F | \hat{H}_{ep} | III \rangle \langle III | \hat{H}_{ei} | II \rangle \langle II | \hat{H}_{ep} | I \rangle}{[E_i - (E_{II} - E_I)][E_i \pm E_{ph} - (E_{II} - E_I)]} + \dots \right|^2 \delta(E_i \pm E_{ph} - E_s) \tag{2.54}$$

where the triple dots indicate the steps permutations, the positive and negative signs of E_{ph} indicate the absorption and creation of a phonon, respectively.

Phonon-phonon interaction

In perfect crystals, phonons have infinite lifetimes and their energy is given by a Dirac delta function (see equation 2.54), this is the harmonic approximation. In real crystals, phonons interact with lattice defects and other phonons, creating decay channels that result in a finite phonon lifetime, linewidth, and a frequency shift defined by the anharmonic decay model. The phonon self-energy, Σ , is given by:

$$\Sigma(\omega_0) = \Delta(\omega_0) + i\Gamma(\omega_0) \tag{2.55}$$

where ω_0 is the single-phonon frequency, and the real and imaginary parts determine the changes in the phonon frequency and linewidth, respectively, and obey the Kramers-Kronig relations. Additionally, a lineshape function, L can substitute the Dirac delta in the scattering cross-section, resulting in [212]:

$$\frac{\partial^2 \sigma}{\partial \Omega \partial \omega} \sim \left| \hat{e}_s \cdot \frac{\partial \chi}{\partial \vec{u}} \cdot \hat{e}_i \right|^2 (2n + 1) L(\omega, \omega_0), \quad (2.56)$$

here, the number of phonons, n , follows the temperature-dependent Bose-Einstein distribution. Thus the phonon-phonon interaction probability rises with temperature. Moreover, considering the decay of one optical phonon into two acoustic phonons with equal energies and opposite momentum is the main decay channel [216], and using second-order perturbation theory, we obtain the temperature-dependent frequency, ω_{ph} , full width at half maximum, Γ_{ph} , and phonon lineshape function [217]:

$$\omega_{ph}(T) = \omega_0 - A \left[1 + \frac{2}{\exp(\hbar\omega_0/2k_B T) - 1} \right] \quad (2.57)$$

$$\Gamma_{ph}(T) = \Gamma_0 + B \left[1 + \frac{2}{\exp(\hbar\omega_0/2k_B T) - 1} \right] \quad (2.58)$$

$$L(\omega, T) = \frac{\Gamma_{ph}(T)}{[\omega - \omega_{ph}(T)]^2 + \Gamma_{ph}^2(T)} \left[1 + \frac{1}{\exp(\hbar\omega_0/k_B T) - 1} \right] \quad (2.59)$$

where A, B are positive constants, and Γ_0 is a constant phonon linewidth originated by the interaction between phonons and lattice defects. The temperature dependence of ω_{ph} and Γ_{ph} is plotted in figure 2.11.

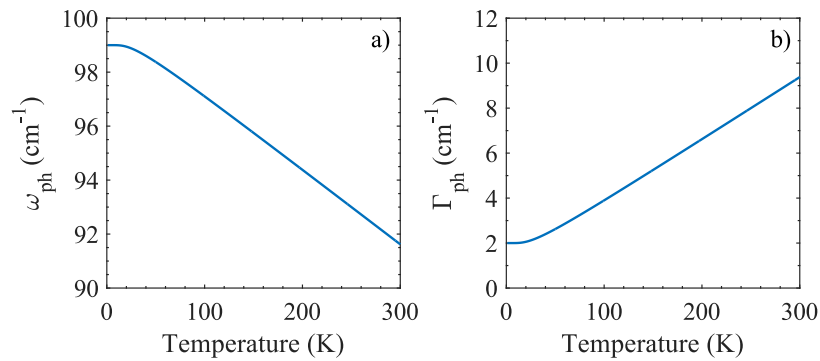


Figure 2.11: Temperature dependence of the phonon a) frequency and b) full width at half maximum given by the anharmonic decay model (equations 2.57, 2.58) for $\omega_0 = 100 \text{ cm}^{-1}$, $A = 1 \text{ cm}^{-1}$, $\Gamma_0 = 1 \text{ cm}^{-1}$ and $B = 1 \text{ cm}^{-1}$.

Electron-phonon interaction

Additional decay channels for lattice vibrations may emerge from the electron-phonon interaction, which impacts the phonon frequency and lineshape of the measured phonon modes. This interaction requires that the phonons and the electronic continuum have similar energies and symmetries. The Raman phonon lineshape indicates the strength of this interaction: as the interactions become stronger, the symmetric phonon lineshapes become Fano asymmetric profiles (see figure 2.12):

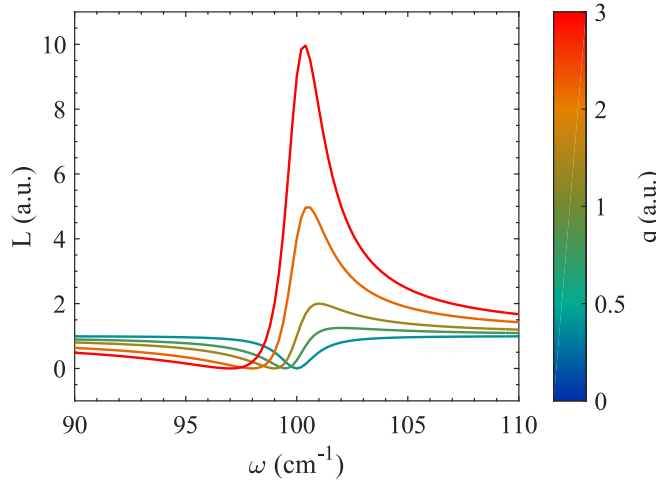


Figure 2.12: Evolution of the Fano profile with different values of the asymmetry parameter, q , with $\omega_0 = 100 \text{ cm}^{-1}$, $\Gamma_0 = 2 \text{ cm}^{-1}$ and $C = 1$.

$$L(\omega, \omega_0) = C \frac{(q + \epsilon)^2}{q + \epsilon^2}, \quad \text{with} \quad \epsilon = \frac{\omega - \omega_0}{\Gamma/2} \quad (2.60)$$

where q is the asymmetry parameter. Values of $q = 0$ or $q \rightarrow \infty$ will replicate a Lorentz curve [218].

2.5 Experimental setup

For the Raman scattering experiments in this thesis, a “macro” Raman setup was utilised at the School of Physics UNSW in pseudo-backscattering mode (see figure 2.13). Here, a “macro” Raman setup was preferred over a “micro” Raman setup since the first offers greater options in sample environment, while the latter is limited to smaller sample environments. Moreover, a commercial “Innova

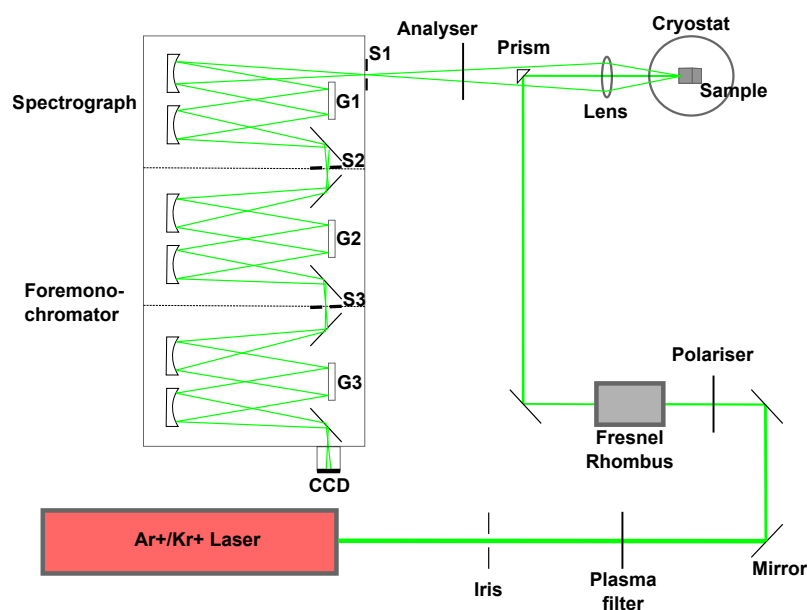


Figure 2.13: Diagram of the Raman setup at the School of Physics UNSW.

70" Ar⁺/Kr⁺ tunable laser source with a maximum power of 5 Watt was operated at a wavelength of $\lambda = 514.32$ nm and the intensity of the laser was tuned so that the sample is illuminated with constant 10 mW to minimise laser heating effects. Once the light passes through an optical iris, a plasma filter removes weaker plasma lines close in wavelength to the selected laser colour, an optional polariser and a Fresnel rhombus set the polarisation of the incident laser. At this point of the laser path, a pair of pinholes are used to clean reflected stray photons and amend lateral contraction effects on the laser beam.

A double refracted optical prism collects the laser beam behind the pinholes and reflected into a photo objective lens ($f = 80$ mm) that focuses the beam onto the surface of the sample with a diameter of ≈ 100 μ m. Notice that if we tilt the sample so that the geometric reflection is not collected by the photo objective lens, then we minimise the Rayleigh scattering signal at the spectrometer. An optional polarisation analyser may be used here to investigate the selection rules of the Raman active modes. Furthermore, a set of three vertical slits controls the input of the scattered light into a Dilor XY triple grating Raman spectrometer that selects the scattered wavelengths with great energy accuracy using triple holographic gratings (1800 lines per mm). Finally, a liquid Nitrogen cooled CCD camera detects the scattered photons at different energies.

Silver Conductive Paste was used to attach the samples to a Copper cold head

while maximising the thermal conductivity inside the cryostat [219, 220]. Here, a Cryovac helium flux cryostat with a temperature range between 12 and 300 K – regulated by a heating element and a PID controller [221] – was used at a vacuum pressure of $\approx 1 \times 10^{-5}$ mbar to isolate the temperature of the sample, and its sample chamber was filled with gaseous Helium (cooling agent) at 300 mbar of pressure.

2.6 SQUID magnetometry

Quantum interferometers based on Josephson junction circuits are widely used as magnetic field sensors, where the Aharonov-Bohm phase of tunneling superconducting currents is measured. As a result of the quantum interference effect, Superconducting Quantum Interference (SQUID) magnetometers can measure magnetic flux variations with high sensitivity. However, commercial SQUID magnetometers are affected by external sources of noise and fitting artifacts that reduce the sensitivity to $\sim 10^{-8}$ emu in VSM mode [222–225].

SQUID magnetometers in DC mode measure the magnetisation, M , which relates to the magnetic moment, m , by $M = m/V$ for a sample with volume V . In general, the magnetic susceptibility is defined by a tensor $\chi_{ij} = \partial_{H_j} M_i$, where H is the magnetic field. Furthermore, the application of an AC magnetic field allows us to measure the real and imaginary components of the magnetic susceptibility, χ' and χ'' (indicative of energy dissipation in magnetic relaxation) [226].

2.6.1 SQUID magnetisation in skyrmion systems

The critical field values of magnetic phase transitions can be determined from the inflection points of $\chi'(B)$ and the minimum of its derivative $d\chi'(B)/dB$, or the local maximum values of χ'' (see figure 2.14) [227]. Thus, $\chi'(B)$ provides evidence of the helical to a conical first-order phase transition at the critical field $B_{C1} = 6$ mT. Moreover, the critical fields $B_{A1} = 14.5$ mT and $B_{A2} = 25$ mT define the lower and upper borders of the high temperature skyrmion phase, and $B_{C2} = 43$ mT defines the conical to ferrimagnetic phase transition. Notice, a hallmark of the conical to skyrmion phase is a local minimum of χ' between two energy dissipa-

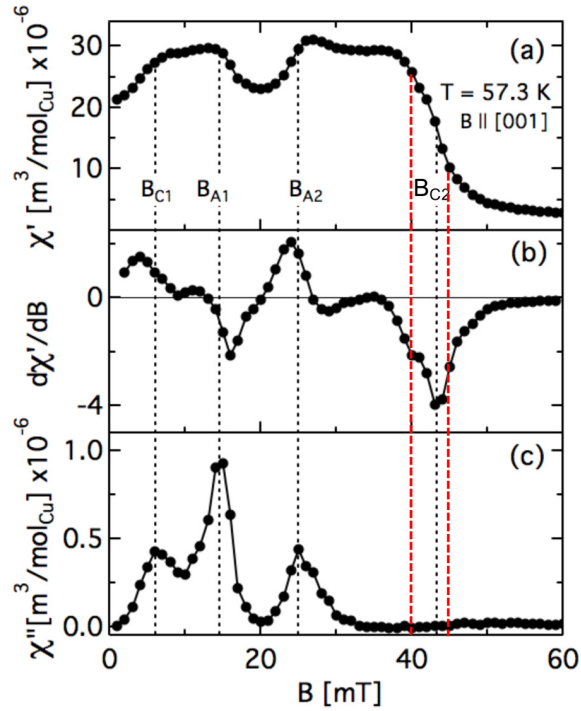


Figure 2.14: AC magnetisation measurements of single crystalline Cu_2OSeO_3 plotted as a function of the applied field B along the $[001]$ crystallographic axis at $T = 57.3$ K. Panel (a) shows the susceptibility with inflection points at critical fields, (b) shows its derivative whose minimum define the critical field B_{C2} , and (c) shows χ'' with local maxima at the critical fields B_{C1} , B_{A1} and B_{A2} . The dotted lines indicate the critical fields (image taken from [227]).

tion maxima in χ'' [9, 228]. The outlined method has also exposed the emergence of a second skyrmion phase at lower temperatures and higher magnetic fields (see figure 2.15) [10, 79]. However, the low temperature skyrmion lattice is not characterised by two peaks in χ'' as in the case of its higher temperature analog, which may be an indication of different phase transition mechanisms.

In the previous section, we proved that magnetic neutron scattering is correlated to the magnetisation of the sample within a plane perpendicular to the direction of the incident beam of neutrons. Moreover, since Superconducting Quantum Interference Device (SQUID) magnetometry is a method to determine the magnetisation of small samples in the direction parallel to an applied magnetic field. Thus, both techniques complement each other since they enable researchers to investigate different components of the magnetisation vector.

Therefore, we used a commercial setup (MPMS3 by Quantum Design) at

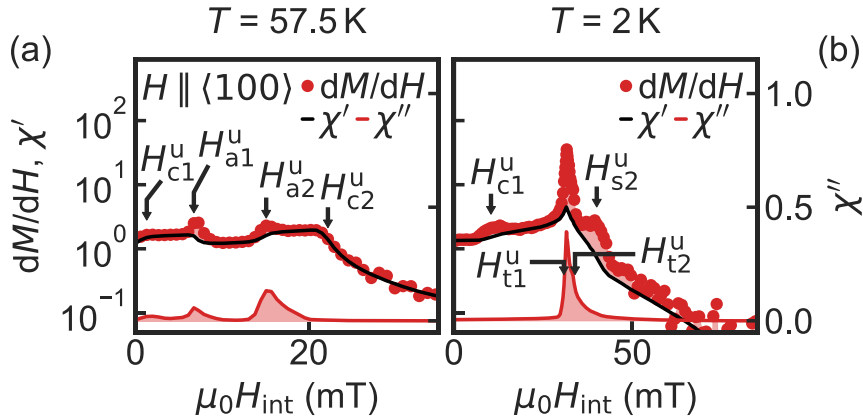


Figure 2.15: AC magnetisation of single crystalline Cu_2OSeO_3 measured upon Zero Field Cooling (ZFC) along one of the $\langle 100 \rangle$ crystallographic directions as a function of magnetic field B at (a) $T = 57.3$ K and (b) $T = 2$ K. The left panel shows the appearance of two peaks in χ'' whereas the right panel only shows one (image extracted from [79]).

UNSW that provides two main modes of operation utilised to characterise the DC-susceptibility through a constant magnetic field, or the AC-susceptibility via an oscillating magnetic field with known frequency and amplitude. However, it is convenient to consider that SQUID magnetometers do not directly measure the magnetisation of a sample, instead they quantify the magnetic flux $\phi = \int \vec{B} \cdot d\vec{A}$, where A is the area of the effective area of the superconducting coils used as sensors – and this magnetic flux induces a voltage, V_{SQUID} , that is recorded by the control computer. Therefore, most commercial SQUID magnetometers operate in VSM mode, which varies the magnetic flux through a mechanical displacement, x , of the sample around the center of the superconducting coil and parallel to both the symmetry axis of the pick-up coil and the applied magnetic field [229].

Scaling behaviour and stability range of skyrmions in
 Cu_2OSeO_3

During the last decade, topological materials have attracted the attention of the scientific community due to a plethora of exotic emergent properties that stem from macroscopic quantum phenomena and open avenues for novel applications on data storage, manipulation, sensor devices and for testing fundamental theories [230–233]. In this context, magnetic skyrmions arise as viable solutions for the limitations on silicon-based information technology. Nevertheless, some fundamental details about the quantum mechanical processes behind the stabilization of these spin vortices remain unanswered [6, 25, 41, 65, 234]. In this chapter, further light is shed onto the role played by thermal fluctuations and magnetic anisotropy in the formation and nucleation of quantum-protected spin swirls and the extent to which their topological protection holds in bulk Cu_2OSeO_3 [86, 235].

3.1 Data collection, reduction and analysis protocols

The reduced data from QUOKKA can be analysed using SASfit, SasView and Igor-based Irena [236–238]. Alternatively, it is possible to analyse these data using high-level programming languages, *e.g.*, Python, Matlab, C++, Java or R.

Given the large amounts of data of this thesis, a set of Matlab scripts were coded to automatise the analysis (available upon reasonable request), which includes defining the geometry of the detector, importing the data, wrangling the data, calculating the variables of interest and their uncertainties [239–242]. Unless otherwise stated, we focus on an annular region in reciprocal space containing the observed Bragg reflections, given by $6.5 \times 10^{-3} \text{Å}^{-1} < |\vec{Q}| < 12.5 \times 10^{-3} \text{Å}^{-1}$ (see figure 3.1). However, different regions may be selected depending on each sample alignment and magnetic phase. Furthermore, non-linear curve fitting methods were applied to the data to determine the annular intensity and magnitude of the scattering vector, $|Q|$ [243–245].

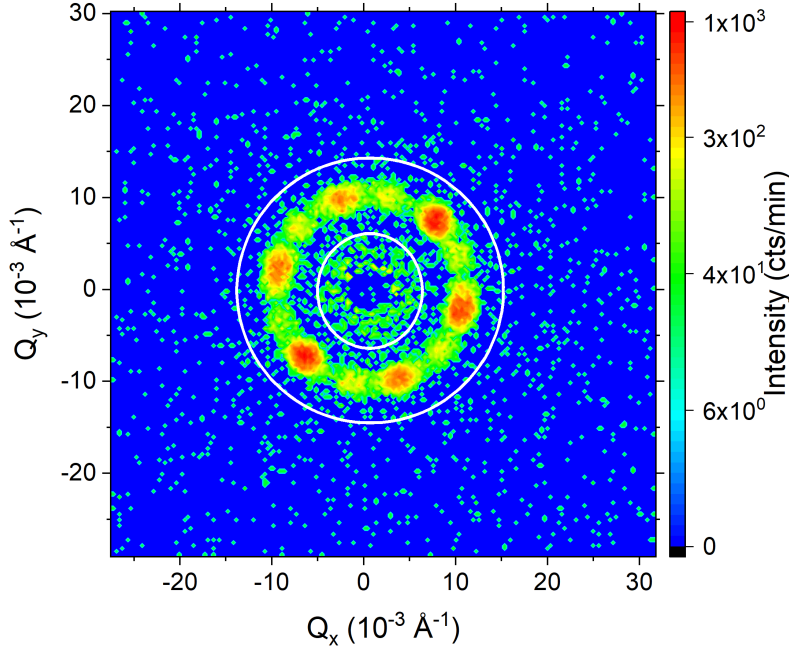


Figure 3.1: Detector mask used for analysing most of our neutron data. The region between dashed circles contains the magnetic scattering signal of interest, whilst its exterior area contains no magnetic scattering signal, and the center of the image is ignored since it corresponds to the position of the beam stop. This scattering pattern corresponds to a randomly orientated sample of pristine Cu_2OSeO_3 and exhibits twelve Bragg peaks in the skyrmion lattice phase at $T = 57 \text{ K}$ and $H = 17.5 \text{ mT}$.

We selected a Gaussian profile to fit the total neutron count, I_n , reported by the neutron detector within the selected annular region since this distribution usually improves the numerical analysis of small angle scattering [162, 163, 246]:

$$I_n(Q) = \frac{I_0}{\omega\sqrt{\pi/2}} \exp\left[-\frac{2(Q-Q_0)^2}{\omega^2}\right] \quad (3.1)$$

where, I_0 is the area under the Gaussian profile curve and will be used to measure the intensity of the observed Bragg peaks within the selected annular region with uncertainty $\sqrt{I_0}$, the centre of the peak, Q_0 , gives the magnitude of the scattering vector, and the half width at half maximum of the peak is $\sqrt{\log 4}\omega$. Moreover, the uncertainty of the magnitudes Q_0 and ω is given by 95 % trust intervals calculated via least square methods applied to the reduced neutron data after binning the neutron count per pixel according to their reciprocal space vector.

Additional information is contained in the raw HDF5 data files such as the instrument parameters for each file. For example, the temperature of the sample is recorded within the HDF5 structure as sensor `"/data/T1S2"`, the field applied by the cryostat magnet is saved in `"/data/B01SP01"`, the total monitor count in `"/data/total_counts"`, and a time stamp * taken at the end of each measurement is stored in `"/end_time"`. This metadata complement the experiment logbooks and data, and can be extracted from the HDF5 files using Matlab scripts (these scripts are available upon reasonable request to the author of this thesis via email).

Unless otherwise stated, we performed our experiments using a neutron wavelength of 5 Ångstrom with 10 % resolution and equal source-to-sample and sample-to-detector distances of 20 meters. The sample was glued onto a thin Aluminium sheet using GE varnish and placed on top of sample holder and below a Cadmium mask with a hole of a diameter proportional to the width of the sample (see figure 3.2 a). The sample holder was introduced inside a cryostat-magnet to apply magnetic fields parallel to the incident neutron beam. The sample was either randomly orientated or pre-aligned to the desired crystal plane using the neutron Laue camera JOEY (see section 2.3) [194, 195], and the alignment was optimized inside the cryostat at QUOKKA at base temperature with no applied magnetic field, *i.e.*, using the magnetic Bragg peaks characteristic of the helical phase, through rocking scans to obtain symmetric scattering intensities. Moreover, the thermal protocols used in our SANS experiments consist of four basic steps (see figure 3.2 b): starting with the sample at room temperature and

*with respect to the UNIX Epoch as specified in the standard ISO-8601 [247]

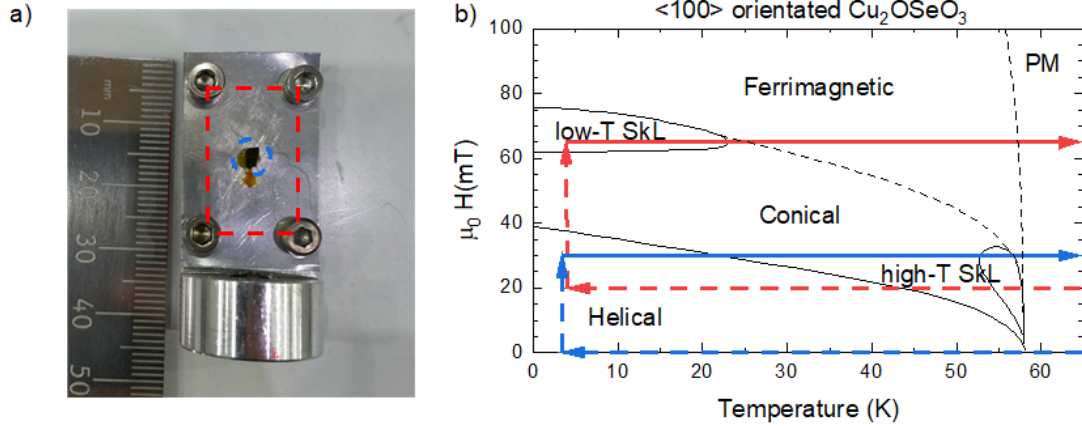


Figure 3.2: a) The sample holder used at QUOKKA consists of a thin Aluminium plate screwed on top of a custom made Al frame (red dashed line). Moreover, a thin Cadmium mask with a hole of a diameter proportional to the width of the sample was attached and centred behind the sample (blue dashed line) b) Diagram of thermal protocols used during our neutron experiments. The blue lines indicate Zero Field Cooling, followed by a magnetic field sweep at constant temperature and data collection upon Field Heating, while the red lines indicate Field Cooling across the high-temperature Skyrmion Lattice (SkL) at $H = 20$ mT, a magnetic field sweep at base temperature and data collection upon Field Heating.

in absence of applied magnetic fields, we first cool the sample either with- (Field Cooling, FC) or without an applied field (Zero Field Cooling, ZFC) down to base temperature (usually $T = 4$ K). Second, if necessary, we ramp the magnetic field up or down to the desired value at a constant base temperature. Third, we collect data upon Field Heating (FH). Fourth, we reset the magnetic state of the sample at zero field in the paramagnetic phase, commonly at 90 K since our SQUID data suggest that short-range order could persist a few degrees within the PM phase.

3.2 Randomly orientated Cu_2OSeO_3

In order to investigate the effect of the sample orientation with respect to the directions of the incident neutron beam and the applied magnetic field on the properties of the observed magnetic Bragg reflections, we will start discussing

the neutron scattering results from a random sample alignment under an applied magnetic field parallel to the direction of the primary neutron beam. The reason to investigate a random orientation is related to the influence of magnetic anisotropy terms along major symmetry axis of the unit cell upon the nucleation of the low- and high-temperature skyrmion lattice phases of Cu_2OSeO_3 . Thus, we collected two Zero Field Cooling phase diagrams upon Field Heating (ZFC/FC) during two different neutron experiments, with a difference of approximately 15° between the first and second random sample alignments. Additionally, we performed ZFC magnetic field sweeps at constant temperature to study the field dependence of the observed features.

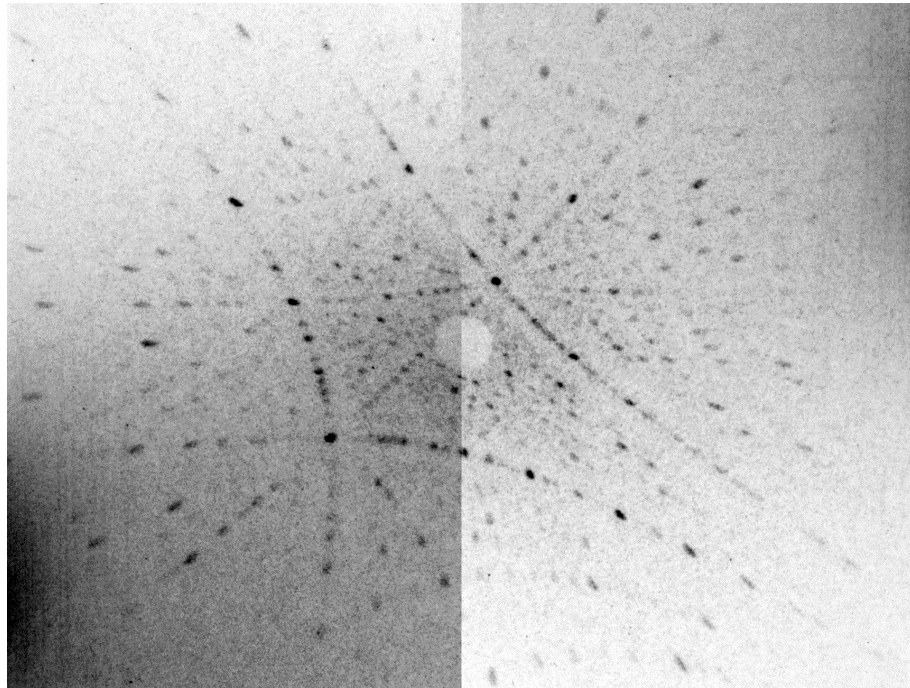


Figure 3.3: The measured neutron Laue diffraction of randomly orientated Cu_2OSeO_3 single crystal at room temperature proves that the sample was not orientated with any of its major symmetry axes parallel to the incident neutron beam. This pattern should be compared to the Laue diffraction pattern of the sample orientated along $\langle 100 \rangle$ (see figure 2.2).

Before our experiments, we glued the sample on a custom sample holder for the instrument QUOKKA and measured a Laue diffraction pattern at the instrument JOEY to confirm the sample had a random alignment. Figure 3.3 shows the

neutron Laue diffraction pattern for the first experiment[†], in which the raw neutron pattern provides evidence that no major symmetry axis pointed parallel to the Laue neutron beam. This can be deduced from the absence of a symmetric set of lines centred around a Bragg reflection at the centre of the detector, which is represented by the white circle at the centre of the image. Notice also the difference between this diffraction pattern and the one produced when the sample is orientated parallel to $\langle 100 \rangle$ (see figure 2.2).

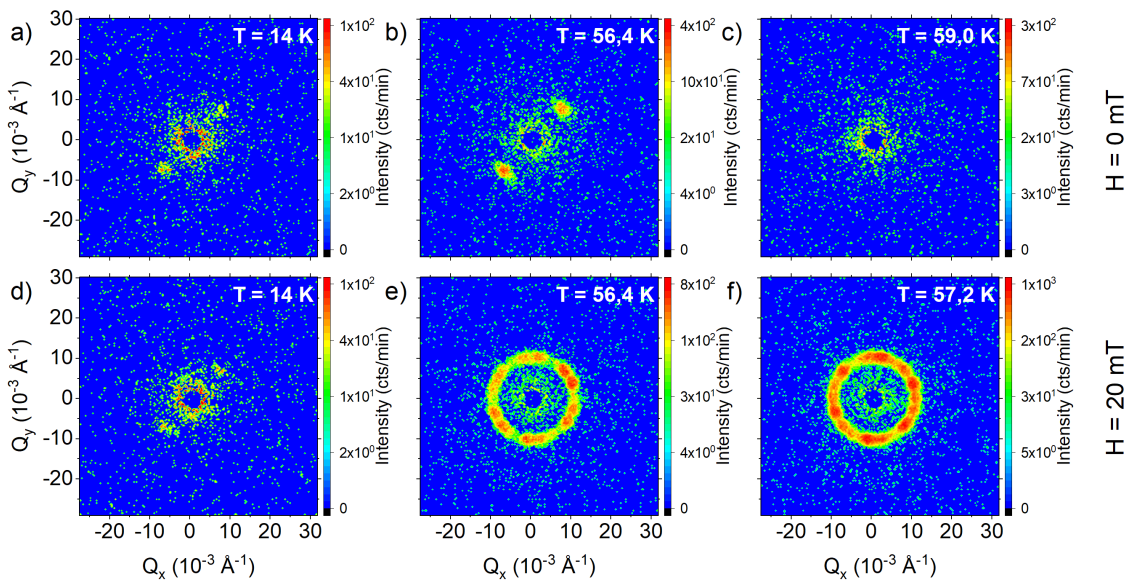


Figure 3.4: Selected reduced SANS diffraction patterns from randomly orientated Cu_2OSeO_3 in a, b, d) the helical, e, f) skyrmion and c) paramagnetic phases

A selection of reduced Small Angle Neutron Scattering patterns measured under this random orientation is shown in figure 3.4. These patterns were accumulated under Zero Field Cooling/Field Heating, and represent three different magnetic phases: the helical state is characterised by magnetic domains with parallel spin stripes propagating along a single direction produces two-fold symmetric patterns as seen in panels a), b) and d); the six-fold symmetric patterns in panels e) and f) correspond to the magnetic skyrmion lattice phase in which the skyrmions form a two dimensional hexagonal lattice with propagation vectors perpendicular to both the applied magnetic field and the incident neutron beam;

[†]Disclaimer: the contrast in the intensity between the two halves of the detector is due to a calibration issue of the instrument, which also explains the bright corners associated with infrared light produced by overheating of the CCD detector

and panel c) shows the signal in the paramagnetic phase that only contains a weak artifact at the position of the neutron beam stop.

The correspondence between the observed scattering patterns and their magnetic phases can be proved via two dimensional Fourier transforms of experimental Lorentz TEM data or through calculations of the Fourier transform of each magnetic phase. First, let us consider the spin-helical stripes, which can be modelled by a set of sinusoidal waves in the (x, y) -plane: $f(x, y) = \cos[2\pi(ax + by)]$. In that case, its 2D Fourier transform is [248–250]:

$$\begin{aligned}
 \mathcal{F}(q_x, q_y) &= \int_{-\infty}^{\infty} \int_{-\infty}^{\infty} f(x, y) e^{-2i\pi(q_x x + q_y y)} dx dy \\
 &= \int_{-\infty}^{\infty} \int_{-\infty}^{\infty} \cos[2\pi(ax + by)] e^{-2i\pi(q_x x + q_y y)} dx dy \\
 &= \frac{1}{2} \delta_{2D} \left(q_x - \frac{1}{a}, q_y - \frac{1}{b} \right) + \frac{1}{2} \delta_{2D} \left(q_x + \frac{1}{a}, q_y + \frac{1}{b} \right) \\
 &= \frac{1}{2} \delta \left(q_x - \frac{1}{a} \right) \delta \left(q_y - \frac{1}{b} \right) + \frac{1}{2} \delta \left(q_x + \frac{1}{a} \right) \delta \left(q_y + \frac{1}{b} \right)
 \end{aligned} \tag{3.2}$$

here, q_x and q_y are 2D reciprocal space coordinates, δ_{2D} are Dirac delta functions are extended to a two dimensional space, a and b are constants that define the real space periodicity of the sinusoidal stripes. Notice, $\mathcal{F}(q_x, q_y)$ in equation 3.2 consists of two peaks at a distance $q = \sqrt{1/a^2 + 1/b^2}$ from the origin of the reciprocal space – the magnitude of the wave propagation vector. Therefore, we observe that the two-fold spatial symmetry of single domain spin stripes (see Panel a) in figure 3.5) lead to two Bragg peaks in reciprocal space characterised by a single propagation vector with magnitude q . However, neutron scattering enables us to detect multiple domains, for example, a two-domain state with perpendicular orientations would lead to a scattering pattern with 4 Bragg peaks. Similarly, the Fourier transform of the skyrmion lattice preserves the 6-fold symmetry of the magnetic lattice observed through Lorentz TEM shown in Panel b), which could be understood as a superposition of three coplanar propagation vectors per domain, although a sample could have more than one skyrmion domain [9, 42].

A series of almost 400 SANS patterns accumulated during our first experiment on the randomly orientated sample lead to the magnetic phase diagram shown in panel a) of figure 3.6, which includes a narrow region zoomed in panel b) below

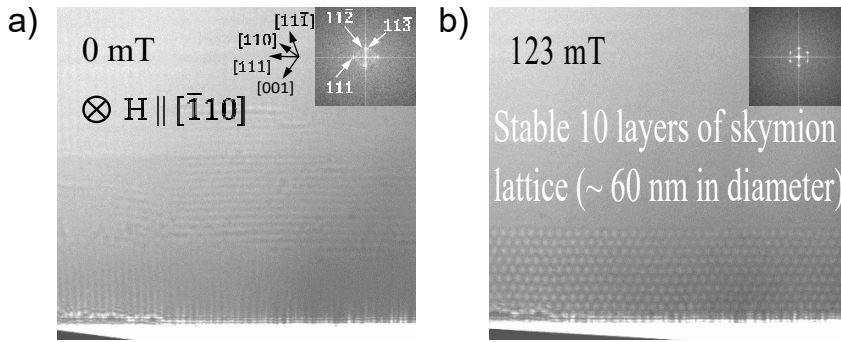


Figure 3.5: Lorentz TEM images of a) the spin-helical and b) skyrmion phases of Cu_2OSeO_3 measured at $T = 26$ K upon a field sweep different magnetic fields by our collaborators at Brookhaven National Laboratories (figure not published, but part of the project leading to reference [76]).

the paramagnetic transition temperature, in which a magnetic skyrmion lattices crystallises. Additionally, we determined c) the magnitude of the scattering vector. The latter quantity, $|\vec{Q}|$, is inversely proportional to the distance between individual skyrmions in the skyrmion lattice (or individual spin helices in the helical phase), as given by Bragg's law, thus it can be used as a phase transition parameter since it tends to zero when a magnetic phase is no longer periodic in space.

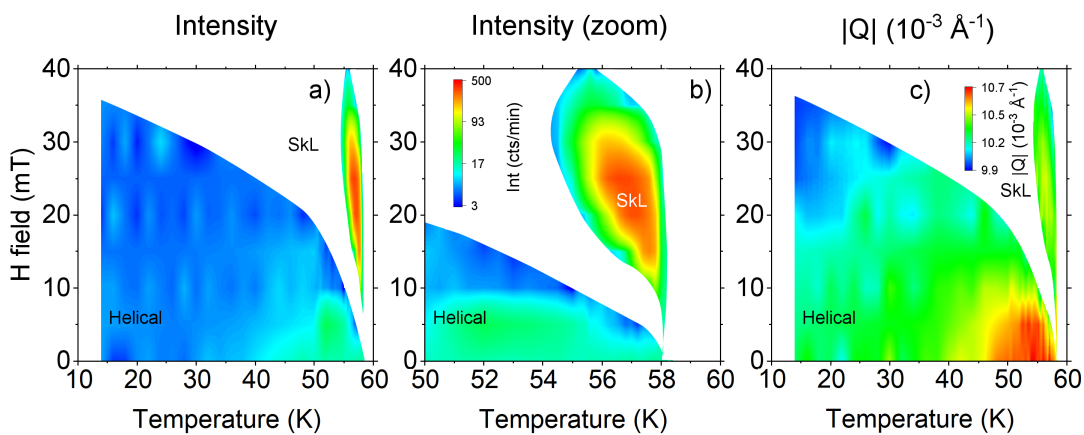


Figure 3.6: The intensity of the magnetic Bragg peaks measured by Small Angle Neutron Scattering enables us to identify a) the phase diagram of randomly orientated Cu_2OSeO_3 and b) a small range of temperatures in which a skyrmion lattices develops. Moreover, from the centre of the Bragg peaks, we obtain c) the magnitude of the scattering vector of the observed Bragg reflections.

First, we observe both the spin helical state, and the high temperature skyrmion pocket centred at $T \approx 57$ K. To analyse these phases, let us focus on the temperature dependence of a) the neutron intensity, b) the propagation vector, and c) the periodicity of the magnetic lattices shown in figure 3.7 for $H = 0$ mT and $H = 20$ mT. The intensity (panel a) at zero field is only related to the helical phase, which takes its minimum value at base temperature and reaches its maximum around $T = 55 \pm 1$ K; whereas at $H = 20$ mT the scattering intensity starts with its minimum value at base temperature and vanishes at $T \sim 50$ K, above this temperature the sample enters the conical phase and the Bragg peaks disappear from the detector under this random orientation. But a set of Bragg peaks originated from the skyrmion lattice appear as heating induces a phase transition into the skyrmion lattice state. The scattering intensity exhibits a strong temperature dependence in the skyrmion phase, and reaches its peak value at $T \approx 57$ K before disappearing upon the paramagnetic phase transition. The observed temperature dependence of the intensity within the helical phase along this sample orientation is unusual, that is, an increase of the intensity upon heating is contrary to the observations made when the sample is oriented along any of its major symmetry axes (see Section 3.3).

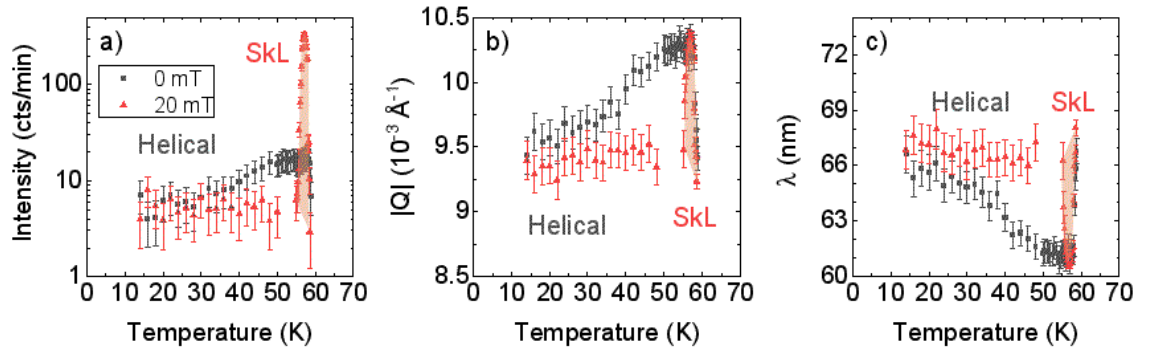


Figure 3.7: Selected temperature scans upon constant applied field of a) the neutron scattering intensity, b) the magnitude of the scattering vector, and c) the spacing of the observed magnetic features upon ZFC/FH from randomly orientated Cu_2OSeO_3 . The red shaded areas indicate the temperature range of the skyrmion lattice.

Moreover, figure 3.7 shows in panel b) the temperature dependence of the magnitude of $|\vec{Q}|$, which at zero field corresponds only to the scaling behaviour of the

helical phase and manifests a continuous growth upon heating until reaching its maximum value a few degrees below $T = 58$ K and decreasing as heating induces a paramagnetic state. This scaling is more evident in panel c) where we plot the distance between magnetic features, λ , which decreases as the sample approaches $T \sim 57$ K. Notice that λ increases upon the melting of the long range magnetic order. Furthermore, at $H = 20$ mT, the periodicity of the helical phase shows a weaker temperature dependence, whilst the skyrmion phase displays a pronounced peak in $|\vec{Q}|$ upon heating at $T \sim 57$ K. The skyrmion lattice scaling implies a change in the magnetic lattice parameter between 67 and 61 nm.

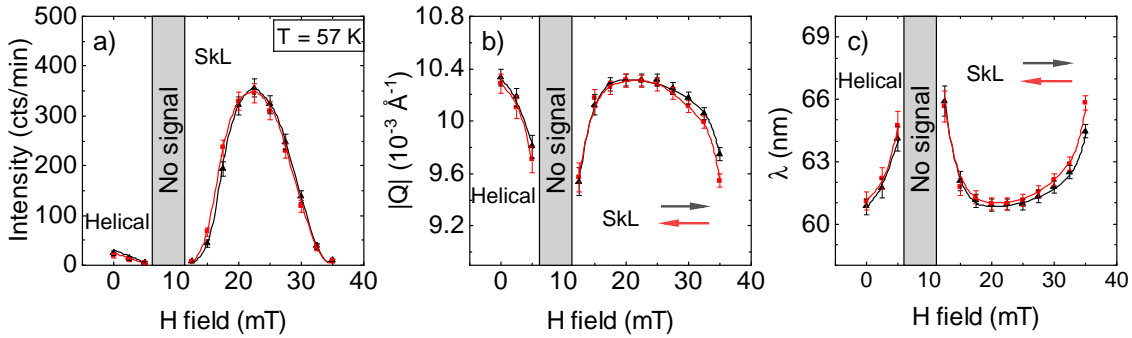


Figure 3.8: Magnetic field scans at a constant temperature of $T = 57$ K of a) the neutron scattering intensity, b) the magnitude of the scattering vector, and c) the spacing of the observed magnetic features upon increasing and decreasing magnetic fields from randomly orientated Cu_2OSeO_3 . The solid lines are guide to the eye used to highlight the observed trends. The gray shadows indicate the conical phase field range in which the signal disappears from the detector under this random orientation.

Additional information is obtained from the magnetic field dependence shown in figure 3.8. The scattering intensity is plotted in panel a) for increasing and decreasing magnetic field sweeps at $T = 57$ K, which is the temperature of the maximum intensity in the skyrmion phase. Here, the spin helical phase reaches its maximum intensity at zero field and is quenched as greater magnetic field values induce a magnetic phase transition into the conical phase, in which the magnetic Bragg reflections disappear from the plane of the neutron detector along this sample orientation. This phase transition is followed by the magnetic skyrmion lattice state at slightly higher magnetic fields, whose field dependence is characterised

by a peak with a maximum intensity at $H \sim 22.5$ mT. No significant hysteresis was found during these field sweeps. Panel b) shows the field dependence of the magnitude of the scattering vector, and panel c) the distance between magnetic features, *i.e.*, the distance between individual skyrmions in the skyrmion phase and between spin helices in the helical phase. Here, the periodicity of the helical phase grows as its intensity decreases with higher fields, whereas the field dependence of the periodicity skyrmion lattice displays a dome with its minimum value between 20 and 25 mT of applied field. Hence, the skyrmion field dependence at $T = 57$ K suggests that the magnetic lattice crystallises within a small range of applied fields and melts down at higher values.

In a second neutron experiment with a randomly orientated sample, we induced a rotation of approximately 15 degrees within the horizontal plane with respect to the alignment of the first random orientation and measured its effects upon ZFC/FH. As a result, we obtain the phase diagram plotted in panel a) of figure 3.9, in which only the high-temperature skyrmion pocket was observed and the blue background color indicates the background level detected in the temperature-field region we studied. A zoomed-in region of the observed skyrmion phase is shown on panel b), on which the background signal is not shown and the plot only displays the region of the phase diagram where magnetic peaks were observed. The region in which the skyrmion phase appears under this second random sample orientation (panel b) resembles its equivalent for the first random observation. Notice, the temperature shift of ≈ 0.5 K between the first and second random orientations data (see figures 3.6 and 3.9) does not affect the width of the temperature range of the skyrmion state and could be caused by the changes in the single ion anisotropy upon changing sample orientations. Nonetheless, this shift does not affect the scaling of the magnitude of $|\vec{Q}|$ along the first and second random sample orientations, which are identical within their errors bars. Additionally, panel c) shows $|\vec{Q}|$ for the magnetic Bragg peaks observed.

An advantage of this sample alignment is that the both the temperature- and field-dependencies of the observed features reveal exclusively the behaviour of the skyrmion lattice without any possible influence of the spin helical phase since

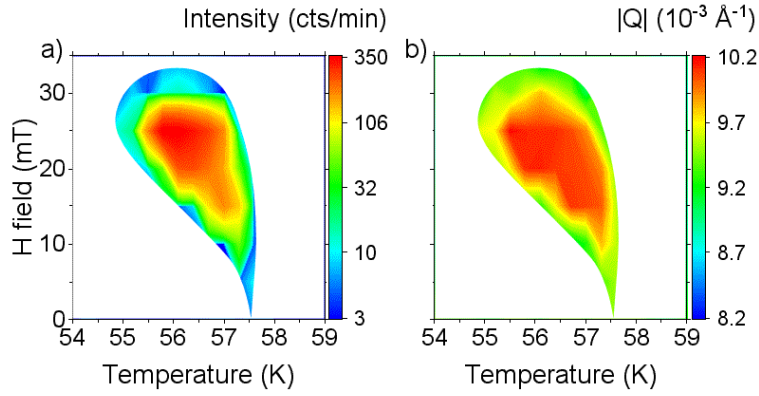


Figure 3.9: a) The magnetic phase diagram of Cu_2OSeO_3 with the sample in the second random sample orientation (deviated $\approx 15^\circ$ with respect to the first random orientation) exhibits magnetic Bragg peaks exclusively across the same temperature and magnetic field region in which the skyrmion lattice stabilises in the first randomly orientation of Cu_2OSeO_3 . Panel b) shows the magnitude of the scattering vector for the skyrmion lattice along this sample orientation.

the spin helical and conical Bragg peaks are not observed by the detector due to the rotation of the Ewald's sphere (see figure 3.10) [251].

In the temperature dependent scans upon an applied magnetic field of $H = 20$ mT, the neutron scattering intensity forms a peak for temperatures between $T = 55$ K and 58 K (see figure 3.10). The maximum intensity was observed near $T = 56.4$ K. Notice that the peak in intensity is shifted by 0.5 K between the two random sample orientations investigated, which could be caused by the effects of the sample orientation in the single ion anisotropy. Interestingly, this intensity drops down above the paramagnetic phase transition temperature, which could be an indication of incoherent magnetic neutron scattering within the analysed region of the detector. Moreover, no Bragg peaks were manifested in the temperature scan with no applied field, this is not necessarily associated with the absence of spin-helical long range order since rotations in the sample alignment lead to a rotation in Ewald's sphere and the helical Bragg peaks appear only parallel to preferential symmetry axes. Notice, the magnitude of the scattering vector and the spacing of the magnetic features in panels b) and c) in figure 3.10 exhibit similar values within the size of the error bars regardless of the small shift in temperature between the data from the first and second random sample orien-

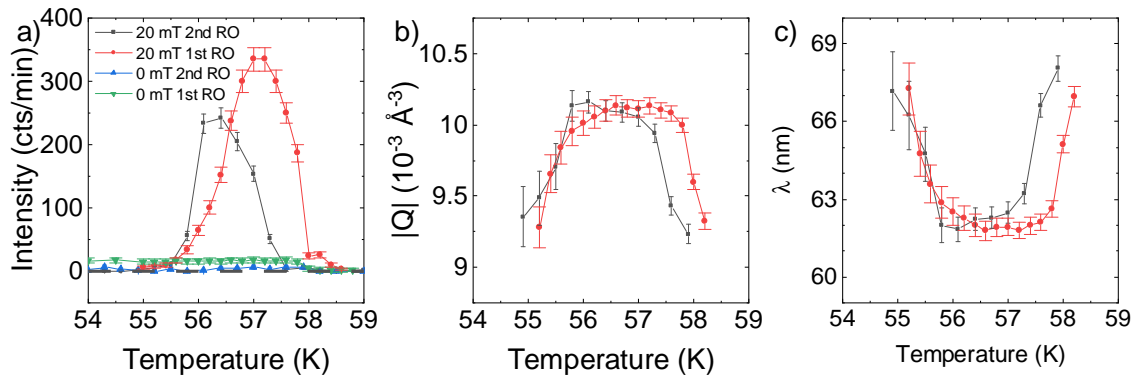


Figure 3.10: The a) neutron scattering intensity, b) magnitude of the scattering vector and c) skyrmion spacing for selected temperature scans from the first and second Random Orientation (RO) of the sample at constant field isolate the scaling of the skyrmions. The dashed line in a) indicates the background intensity below the paramagnetic phase transition temperature.

tations.

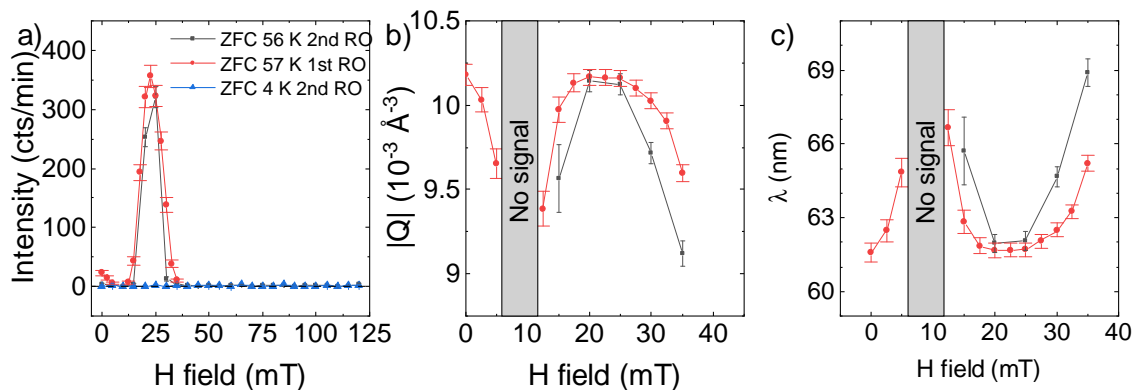


Figure 3.11: The a) scattering intensity, b) magnitude of the scattering vector and c) skyrmion spacing for selected field scans from the first and second Random Orientations (RO) of the sample at constant temperature only reveal the high-temperature skyrmion phase in the second random sample orientation.

Complementary to the phase diagram, scans as a function of magnetic field at constant temperature only reveal the existence of the high-temperature skyrmion pocket close to the paramagnetic phase transition but do not show a low-temperature equivalent (see figure 3.11). However, this lack of evidence does not necessarily imply a lack of effect. In other words, there is a possibility that a low-temperature skyrmion lattice exists upon this sample orientation, but their

magnetic Bragg reflections could have shifted out of the range of the neutron detector of QUOKKA. Hence, we are sure that the high-temperature skyrmion state always manifests along a plane perpendicular to the applied magnetic field regardless of the orientation of the sample with respect to its major symmetry axes. Notice, the magnitude of the scattering vector and the spacing of the magnetic features in panels b) and c) in figure 3.11 exhibit similar values within the size of the error bars regardless of the small shift in magnetic field between the data from the first and second random sample orientations.

3.3 Axially orientated Cu_2OSeO_3

3.3.1 $\langle 100 \rangle$ sample orientation

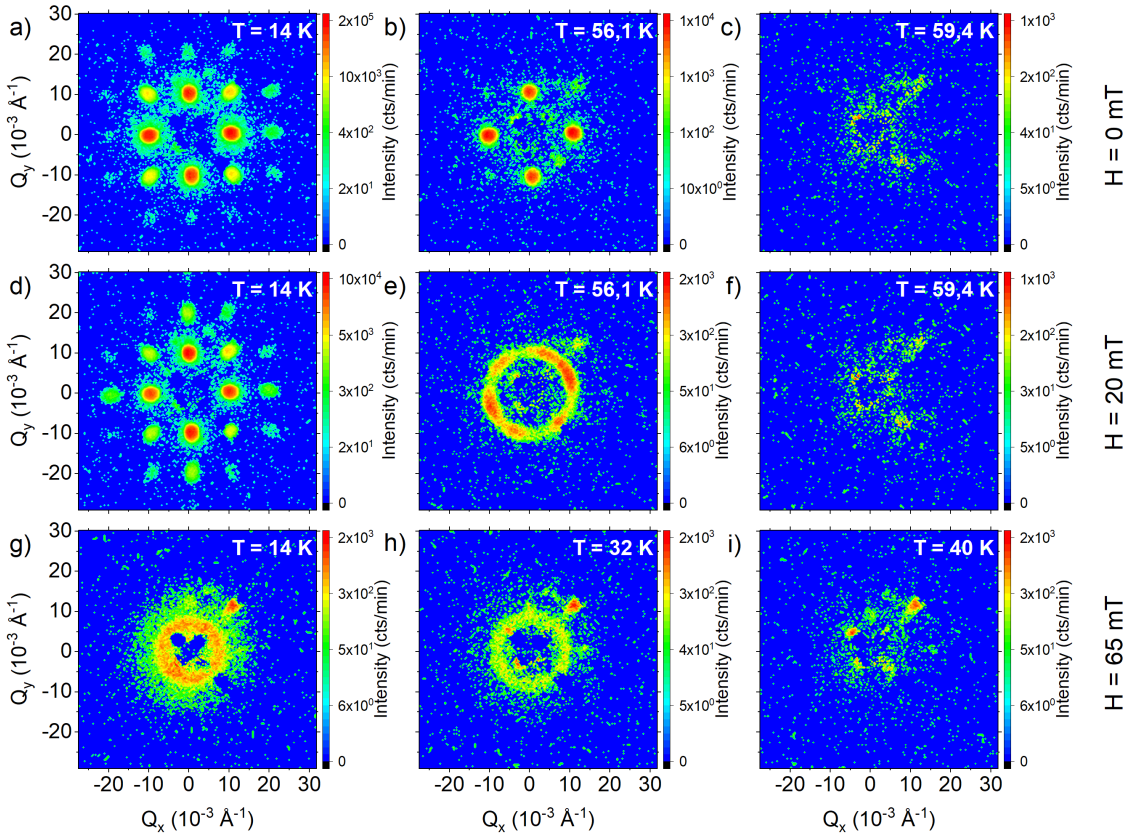


Figure 3.12: Selected SANS diffraction patterns from ZFC Cu_2OSeO_3 when the neutron beam and magnetic field are applied parallel to the $\langle 100 \rangle$ axis in a, b, d) the spin helical, e, g, h) skyrmion and c, f, i) PM phases

In order to investigate the effects of the orientation of the crystallographic axes

of Cu_2OSeO_3 single crystals with respect to the incident neutron beam and the applied magnetic field, we pre-aligned our sample with its $\langle 100 \rangle$ axis along the direction of the neutron beam using the neutron Laue instrument JOEY at ANSTO. The sample was mounted into a cryo-magnet at the instrument QUOKKA, where the sample alignment was optimised at base temperature under no applied magnetic field, that is, in the spin-helical phase. This optimisation was performed using rocking scans until the magnetic Bragg peaks had a symmetric intensity. The data acquisition was then performed using the instrument parameters detailed in Section 2.2 under ZFC/FH. A selection of diffraction patterns is shown in figure 3.12. In panels a), b) and d) we observe 4-fold symmetric patterns that emerge from two or more spin-helical domains. Although panels a), b), and d) pertain to the spin-helical phase, these patterns are not all the same. First, we notice both panels a) and d) exhibit higher-order Bragg reflections (four second-order, four third-order, and eight fourth-order peaks) that suggest a highly ordered four-fold spin helical state at base temperature, but the relative intensities change with the magnitude of the applied field. Second, we observed the higher-order peaks are not visible above $T \approx 52$ K at constant field, which could indicate these features are also temperature dependent, as we will discuss later. With respect to the skyrmion phase, we observed a six-fold symmetric pattern in the same temperature and magnetic field range of the randomly orientated sample setup (around $H = 20$ mT, $T = 56.4$ K), but a scattering ring also appears at higher magnetic fields and lower temperatures, which has been associated previously with fluctuations between skyrmion domains in single crystalline Cu_2OSeO_3 [5, 76–80]. Hence, the observed circular patterns suggest this second skyrmion phase could have a rotationally-symmetric lattice in real space. Lastly, some asymmetric features at low- $|\vec{Q}|$ values remain present in the scattering patterns collected from the sample after all the Bragg reflections have disappeared in c, f, i) the paramagnetic phase. These low- $|\vec{Q}|$ features have been associated with defects in the texture of the single crystal [9]. Let us now take a look at the resulting ZFC/FH magnetic phase diagram along $\langle 100 \rangle$ and compare it with one its first random orientation equivalent (see figure 3.13).

It is worth noting that the temperature-field region in which the spin helical

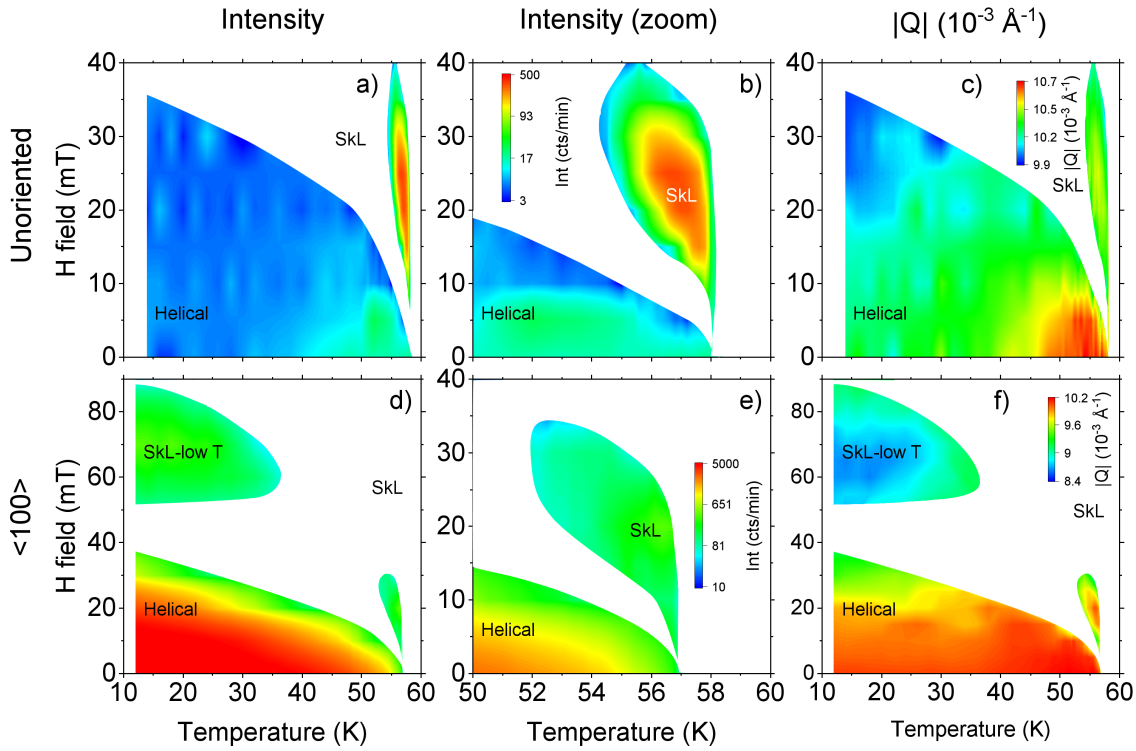


Figure 3.13: Comparison of the magnetic phase diagrams extracted from the neutron scattering intensity a) randomly orientated, and d) $\langle 100 \rangle$ -aligned Cu_2OSeO_3 single crystal. Panels b, e) zoom into the high-temperature skyrmion pockets shown in panels a, d). Panels c, f) show the magnitude of the neutron scattering vector from randomly- and $\langle 100 \rangle$ orientated Cu_2OSeO_3 .

and high-temperature skyrmion regions appear along $\langle 100 \rangle$ is similar to that in which this phases manifested along the first random sample orientation. However, a second skyrmion phase appears along $\langle 100 \rangle$ in a region that is thermodynamically disconnected from the high-temperature skyrmion pocket, that is, at higher magnetic fields and lower temperatures down to base temperature. Before discussing the temperature and field dependence of the observed features, let us consider the effects of Field Cooling along $\langle 100 \rangle$ on the observed phases.

As a result of measuring data upon FC (at $H = 20$ mT)/FH, a different set of scattering patterns were observed (see figure 3.14). In panels a, b, d) we observe the spin-helical phase, but not as we did upon ZFC/FH. After we cool down the sample at an applied magnetic field of 20 mT, a superposition of the spin-helical structure and FC-skyrmions appear when measuring upon FH at 20 mT even at base temperature as shown in panel d), which strongly suggests that Field Cool-

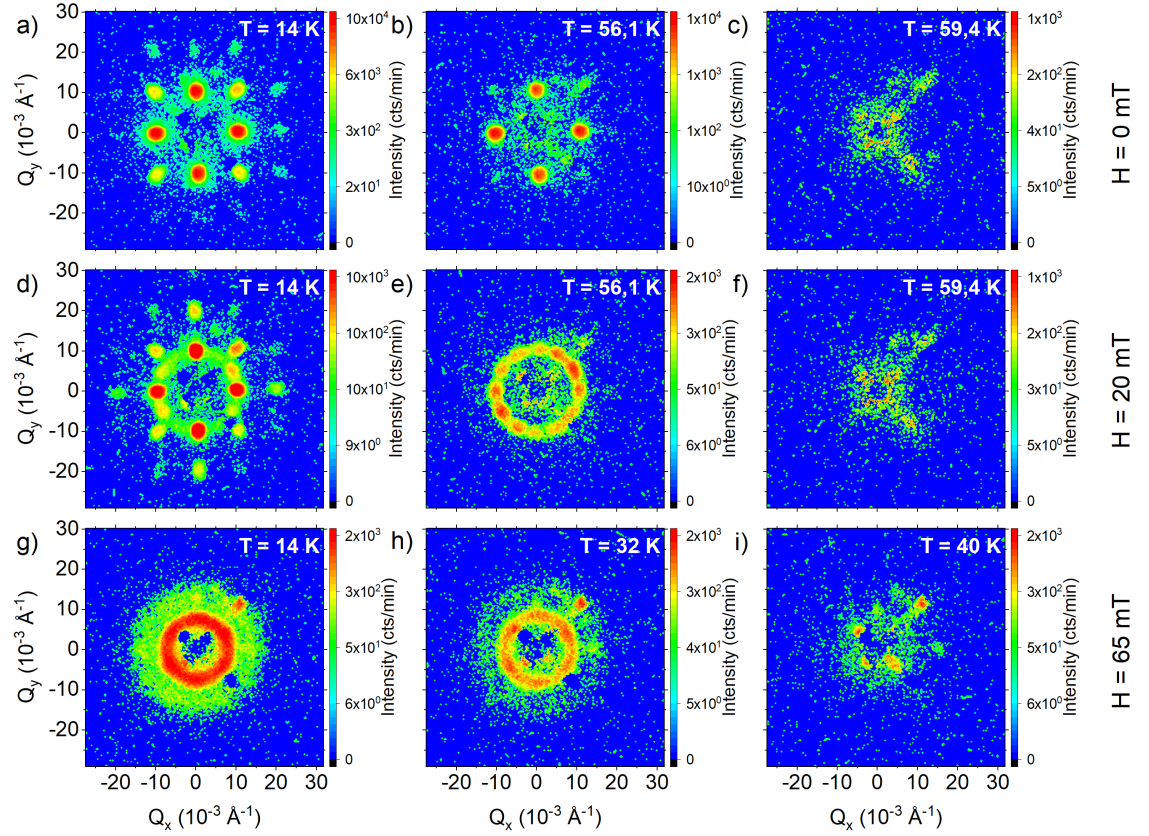


Figure 3.14: Selected SANS diffraction patterns from FC COSO when the neutron beam and magnetic field are applied parallel to the $\langle 100 \rangle$ axis and the sample is FC at $H = 20$ mT in a, b, d) the spin helical, e, g, h) skyrmion and c, f, i) PM phases

ing across the centre of the high-temperature skyrmion pocket (at $H = 20$ mT) induces the nucleation of some magnetic domains of meta-stable skyrmions, which persist even at base temperature and upon Field heating [80]. This coexistence indicates a strong competition between different magnetic phases as in the case of skyrmions in kagomé lattices [252]. Moreover, the high-temperature skyrmion pocket turned into a 12-fold symmetric pattern upon FC/FH, whereas a 6-fold symmetry was observed upon ZFC/FH, which may suggest a coexistence of two or more magnetic skyrmion domains with their planes rotated horizontally 30 degrees with respect to the other, as it has been previously discussed in the literature [10, 76, 253, 254]. Finally, the c, f, i) paramagnetic state patterns exhibit the same low- $|\vec{Q}|$ features observed upon ZFC/FH, which may suggest they arise from defects in the texture of the sample [9].

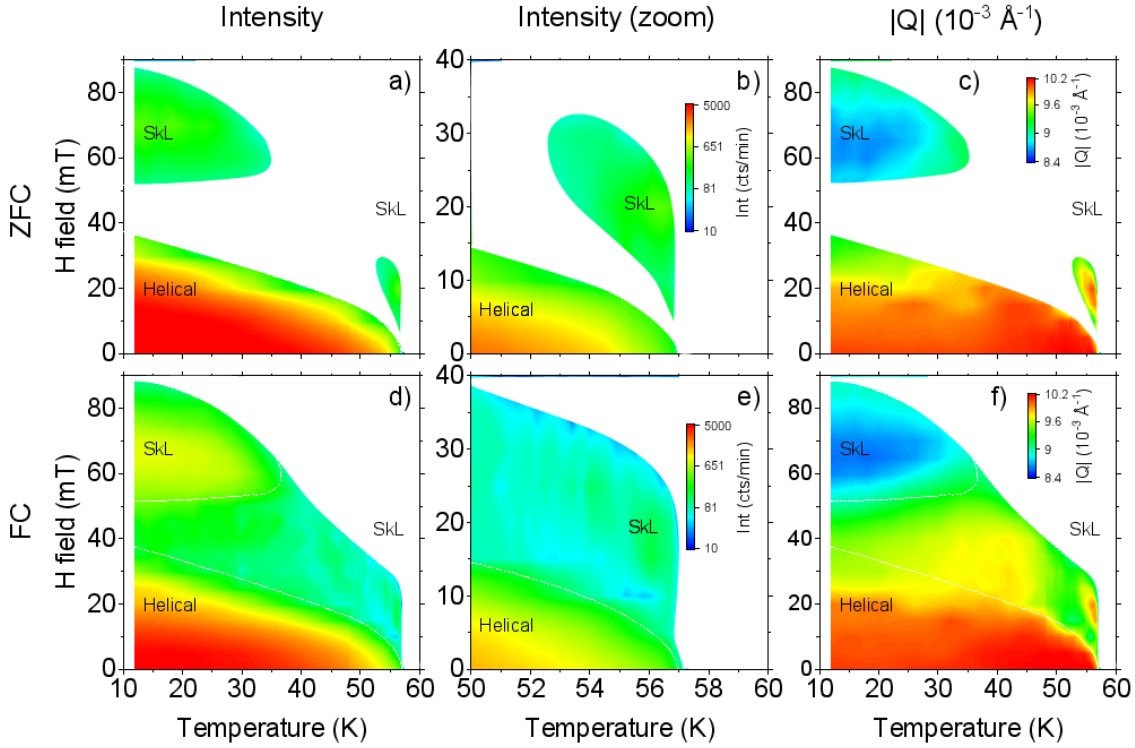


Figure 3.15: Neutron scattering intensity from the $\langle 100 \rangle$ -orientated Cu_2OSeO_3 single crystal upon a) ZFC/FH and b) FC at $H = 20$ mT/FH. The intensity at the high-temperature skyrmions is zoomed for ZFC/FH and FC/FH in panels b) and e) respectively, and the magnitude of the neutron scattering vector under ZFC/FH and FC/FH are shown in panels c) and f) respectively.

The magnetic phase diagrams resulting from measuring upon Field Cooling at an applied magnetic field of 20 mT down to base temperature, ramping the magnetic field to the desired value and measuring the scattering intensity upon Field Heating (FC/FH) together with the magnitude $|\vec{Q}|$ are compared to their ZFC/FH equivalents in figure 3.15.

Let us consider the temperature and field extension of the helical phase region of the $\langle 100 \rangle$ -orientated magnetic phase diagram (see figure 3.15). Both upon a) ZFC/FH and d) FC/FH, this phase manifests as a 4-fold scattering pattern visible from base temperature and up to T_C upon measuring at zero field, from base temperature up to $T \sim 53$ K at an applied field of $H = 10$ mT, up to $T \sim 40$ K at 20 mT, up to $T \sim 30$ K at 30 mT, and it is not visible upon measuring at a constant field of 40 mT. At constant base temperature, we find this phase from zero field up to $H = 35$ mT. Although the border of this magnetic phase depends both on the tem-

perature of the sample and the applied field, this behaviour remains unaffected by the cooling and heating protocol. Similarly, the high-temperature skyrmion pocket observed just below the paramagnetic phase transition temperature and between applied fields of $H \sim 5$ and 35 mT, persists within the same temperature and field conditions upon both b) ZFC/FH and e) FC/FH. The low-temperature skyrmion phase is, likewise, observed within the same range of temperatures between base temperature and $T \sim 30$ K, and between fields of approximately 55 and 85 mT upon both a) ZFC/FH and d) FC/FH. However, a broad intermediate region of a) the ZFC/FH phase diagram exhibits no magnetic Bragg reflections between the low- and high-temperature skyrmion phases. This intermediate region develops intense skyrmion features upon d) FC/FH. Moreover, field cooling at 20 mT induces a noticeable increase in the intensity of the low-temperature skyrmion Bragg peaks, and a coexistence of the helical and skyrmion states.

In the literature, there has been a discussion whether the low- and high-temperature states are thermodynamically disconnected or not [77–80]. In our experiments, we observe these two skyrmion states are thermodynamically disconnected upon ZFC/FH, but skyrmions populate the intermediate region of the phase diagram upon FC/FH, which resembles observations of metastable skyrmion states upon an applied electric field and fast FC [78, 80, 255]. Hence, our data may suggest that the observed increase of the temperature and field range in which a skyrmion lattice appears with metastable states. Nonetheless, we shall explore the question of their stability in section 4.3. For now, let us drive our attention towards the scaling behaviour of the observed magnetic features. Panels c) and f) of figure 3.15 provide a broad picture of the temperature and field dependence of $|\vec{Q}|$ for a crystal with the magnetic field along the $\langle 100 \rangle$ direction upon c) ZFC/FH and f) FC/FH. We may notice that $|\vec{Q}|$ takes different values for the low- and high-temperature skyrmion states for both ZFC/FH and FC/FH, which could imply they respond differently to variations in field and temperature. If that is the case, this could indicate different stabilisation mechanisms for both skyrmion lattices. To examine this question, let us discuss the temperature and field dependence of selected data at constant field and temperature, respectively.

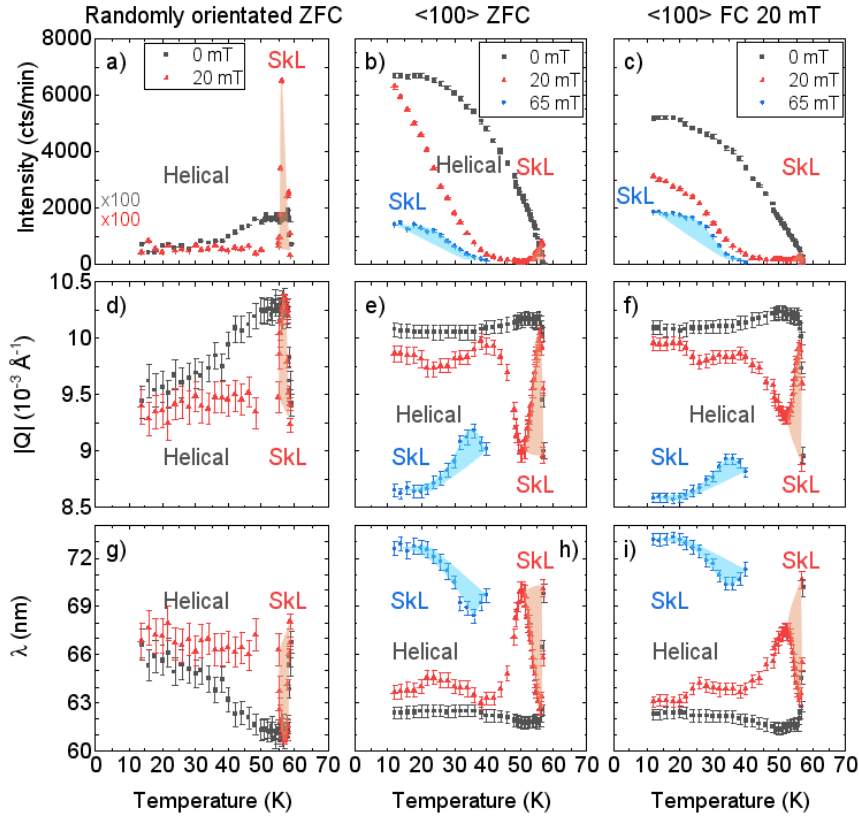


Figure 3.16: Comparison of a-c) the neutron scattering intensity, d-f) the magnitude of the scattering vector, $|\vec{Q}|$, and g-i) the spatial periodicity of the magnetic lattices of Cu_2OSeO_3 measured using temperature sweeps at constant magnetic fields along the first random sample orientation (left column), $\langle 100 \rangle$ upon ZFC/FH (middle column), and FC/FH (right column). The coloured shadows indicate the region in which a skyrmion lattice was observed. Note: the helical intensity in a was multiplied by 100.

Figure 3.16 shows the temperature dependence curves for the a-c) neutron scattering intensity, d-f) magnitude of the scattering vector, and g-i) spacing of the magnetic structures observed from the first random sample orientation and the $\langle 100 \rangle$ -aligned sample under ZFC/FH and FC/FH at selected constant magnetic fields. In the helical phase with or without applied magnetic field, the scattering intensity is lower in the case of the first randomly orientated sample than when the $\langle 100 \rangle$ -axis of the sample is parallel to the incident neutron beam and magnetic field. We notice the scattering intensity is also higher when measured without an applied field than at $H = 20$ mT along any sample orientation. However, the temperature dependence of the intensity differs between the two orientations: the

intensity grows as temperature raises along the first random orientation, but the opposite behaviour is observed along $\langle 100 \rangle$, which exhibits its maximum at base temperature. Moreover, we observed a different behaviour upon ZFC/FH and FC/FH: the intensity measured without an applied field is higher for ZFC/FH than with FC/FH; similarly, FC/FH reduces the intensity measured with $H = 20$ mT with respect to the values obtained upon ZFC/FH. On the other hand, only a small difference was observed in the scaling behaviour of the helical phase upon changing the orientation of the sample: along both $\langle 100 \rangle$ and the first random sample orientation, $|\vec{Q}|$ raises upon heating in the absence of applied magnetic fields, which implies the distance between the spin helices is reduced with increasing thermal energy. Nonetheless, this scaling behaviour becomes more complex in the case of the $\langle 100 \rangle$ -orientated samples when measured upon an applied field of $H = 20$ mT, which induces a non-linear behaviour between base temperature and $T \sim 40$ K, *i.e.*, in the helical phase, followed by a sudden drop in $|\vec{Q}|$ until the sample enters the skyrmion lattice state.

The temperature-dependence of the neutron scattering intensity of the high-temperature skyrmion pocket (red curves in figure 3.16 a-c) follows a similar behaviour along every orientation, which is defined by an intensity peak with a maximum centred around $T \sim 56.4$ K, and peak width and position in temperature remain unaltered by the thermal protocols used. Similarly, $|\vec{Q}|$ retains its peak-like behaviour along all orientations of the sample and thermal protocols and displays its maximum value at $T \sim 56.4$ K. Nevertheless, the low-temperature skyrmion state displays a thermal dependence different from its higher temperature equivalent. This skyrmion state was not observed under the first random sample orientation, but appears in a broad temperature range with the neutron beam and applied field along $\langle 100 \rangle$ [78]. The neutron scattering intensity remains approximately constant from base temperature up to $T \sim 30$ K upon both ZFC/FH and FC/FH, although the intensity upon FC/FH is more than twice higher than upon ZFC/FH. Moreover, the magnitude $|\vec{Q}|$ remains approximately constant up to $T \sim 25$ K upon both ZFC/FH and FC/FH; upon further heating the temperature dependence of $|\vec{Q}|$ develops a peak with its maximum centred around $T \sim 35$ K. This is in contrast to the high-temperature skyrmion

phase, which exhibits a minimum in $|\vec{Q}|$ at the maximum intensity. Thus, the differences between the temperature dependence of the magnetic Bragg reflections from the low- and high-temperature skyrmion lattices may suggest that the high-temperature skyrmion state depends strongly on thermal fluctuation while the low-temperature skyrmions are less affected by thermal energy. Furthermore, the temperature- and field-dependence of both skyrmion states may assist us in solving the question about the conditions that stabilise these two long-range orders. In order to clarify this, let us examine the field dependence of selected scattering patterns at constant temperature.

The strong differences in the temperature-dependence of the low- and high-temperature skyrmion lattices suggest that they may be stabilised by different factors: the high-temperature skyrmion state crystallises as a consequence of thermal fluctuations, whereas the low-temperature skyrmion lattice depends more on magnetic anisotropies and quantum fluctuations as previously proposed in the literature [80, 81, 85]. To confirm the role of magnetic anisotropies in the formation of both skyrmion states we will investigate the effect of a third sample orientation: $\langle 110 \rangle$. But, before discussing a second sample orientation, let us comment the temperature and field dependence of the secondary magnetic Bragg peaks observed in the scattering patterns along $\langle 100 \rangle$.

Figure 3.17 shows the neutron scattering intensity of first- and secondary magnetic Bragg peaks shown in figures 3.12 and 3.14 at $H = 0$ and 20 mT, that is, within the helical and high-temperature skyrmion states. In this discussion, “1st order” represents the set of four first-order Bragg reflections found at $\vec{Q} = (\pm q_x, 0)$ and $(0, \pm q_y)$ in the diffraction patterns, “Secondary” is the set of four Bragg reflections at $\vec{Q} = (\pm q_x, \pm q_y)$, and by “Higher” we denote those reflections at $\vec{Q} = (\pm 2q_x, 0)$. To analyse these reciprocal space regions, annular sections in the (q_x, q_y) detector range were defined for each case: “1st order” was calculated within $0.0065 \text{ \AA}^{-1} \leq |\vec{Q}| \leq 0.0125 \text{ \AA}^{-1}$, “Secondary” in $0.0092 \text{ \AA}^{-1} \leq |\vec{Q}| \leq 0.0177 \text{ \AA}^{-1}$, and “Higher” between $0.0145 \text{ \AA}^{-1} \leq |\vec{Q}| \leq 0.0280 \text{ \AA}^{-1}$. Moreover, these reciprocal space regions were carefully defined within an angular range of $\pm 15^\circ$ from the centre of the Bragg reflections. We notice that upon both ZFC/FH and FC/FH the temperature dependence of the observed peaks reaches its max-

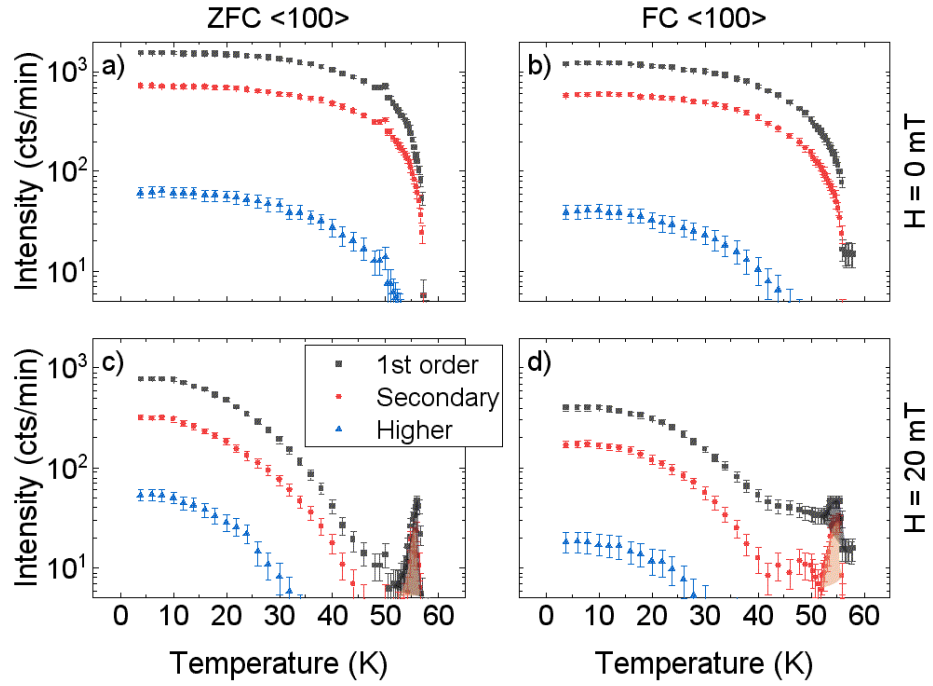


Figure 3.17: Temperature dependence of the intensity of higher-order Bragg peaks from Cu_2OSeO_3 single crystal when the neutron beam and the applied magnetic field are parallel to the $\langle 100 \rangle$ crystallographic axis.

imum intensity at base temperature and decreases monotonically until a phase transition occurs: the helical to paramagnetic transition around 58 K at $H = 0$ mT and the helical to conical phase transition at $H = 20$ mT. Moreover, the first-order scattering intensity is well defined within the high-temperature skyrmion range and reaches a local maximum around the centre of the skyrmion phase at $T \approx 56$ K, the intensity of “Secondary” follows a similar trend but is weaker than “1st order”, and “Higher” is even weaker than “Secondary” and was not observed within the skyrmion phase. Furthermore, the intensities of these features follow a similar temperature dependence scaled by a constant ratio for each case, with the intensity of “1st order” disappearing close to the phase transition temperatures, the intensity of “Secondary” disappears at a temperature less than 1 K before “1st order”, but “Higher” vanishes completely more than 10 K before the other two reflections. Additionally, the observed intensities were higher under ZFC/FH than upon FC/FH, and decrease with increasing applied magnetic fields as shown for the first order reflections in figure 3.16.

Complementary, figure 3.18 shows the magnitude of the scattering vector, $|\vec{Q}|$,

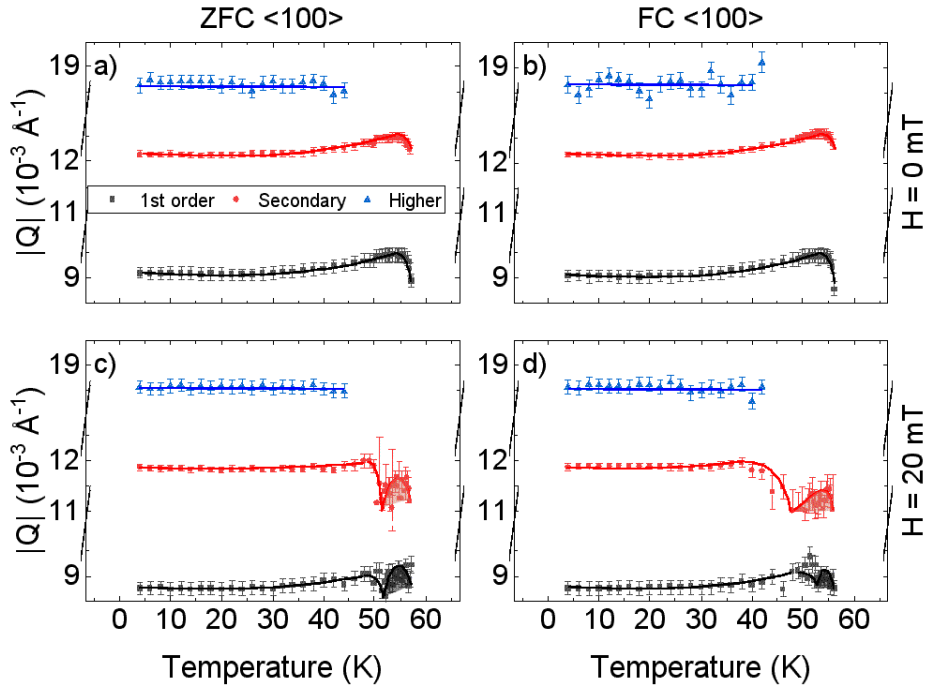


Figure 3.18: Temperature dependence of the $|\vec{Q}|$ magnitude of higher-order Bragg peaks from Cu_2OSeO_3 when the neutron beam and magnetic field are applied parallel to the $\langle 100 \rangle$ axis. The black and coloured symbols correspond to the first- and higher order peaks observed in our data. The coloured lines are guides to the eye, and the coloured areas indicate the temperature region of the skyrmion lattice.

for the first- and higher-order magnetic Bragg reflections. We observe that independently of the thermal protocol or the applied magnetic field, the magnitude of $|\vec{Q}|$ for “Higher” is approximately twice larger than for “1st order”, and it is approximately $\sqrt{2}$ times larger for “Secondary” than for “1st order”. Secondary neutron scattering peaks have been previously reported in non-centrosymmetric magnets, but their origin is not always clear since secondary Bragg reflections could be caused by high-order neutron scattering, double scattering or additional modulations on top of long-range magnetic ordering [9, 18, 78, 80, 155]. Nonetheless, Renninger scans are able to elucidate between high-order and double scattering, with the last one emerging as usual consequence of highly intense Bragg reflections [154, 155, 256]. As part of our sample alignment fine-tuning procedure at QUOKKA, we performed rocking scans along three different angles at base temperature and without an applied field. The resulting Renninger scans

(not shown here) reveal a clear angular dependence of the intensity of the secondary Bragg reflections, and lead us to associate these secondary Bragg reflections to double scattering peaks and not with high-order Bragg peaks since the latter would show no angular dependent intensity [256]. However, it would be desirable to confirm the double scattering nature of these reflections by using a neutron filter between the sample and the detector at QUOKKA, which would remove any high-order scattering signal from the recorded data.

3.3.2 $\langle 110 \rangle$ sample orientation

Small angle scattering patterns were collected with the $\langle 110 \rangle$ crystallographic axis of our sample parallel to the incident neutron beam and the applied magnetic field. Temperature scans were accumulated upon ZFC at $H = 0$ mT and FC/FH at $H = 20$ mT, to detect the presence or absence of the helical and skyrmion phases. A selected set of scattering patterns is shown in figure 3.19 and reveals a two-fold symmetric pattern of magnetic Bragg reflections within a, b) the spin helical phase at zero field, e, f) a six-fold symmetric pattern typical of the high-temperature skyrmion lattice phase at $H = 20$ mT that disappears c) above the paramagnetic transition temperature, T_C . We notice that the observed magnetic Bragg peaks are not Gaussian under this sample orientation, but they are described by Gaussian profiles along other sample orientations. These deviations from a Gaussian shape are due to the strong influence of the shape of the single crystal used and its effects in the demagnetisation fields or due to changes in the instrumental resolution function into an elliptical shape as an effect of sample alignment [9, 257].

A noticeable superposition of d) the spin-helical and high-temperature skyrmion lattices develops at base temperature and an applied magnetic field of $H = 20$ mT, in which the six-fold skyrmion features have a weaker intensity than the helical Bragg reflections, and the two-fold spin-helical reflections exhibit higher-order diffraction peaks as we reported along the $\langle 100 \rangle$. These observations suggest that Field Cooling the sample across the centre of the high-temperature skyrmion lattice (at $H = 20$ mT) along the $\langle 110 \rangle$ crystallographic direction could freeze the skyrmions down to base temperature as in the case of the $\langle 100 \rangle$ sample

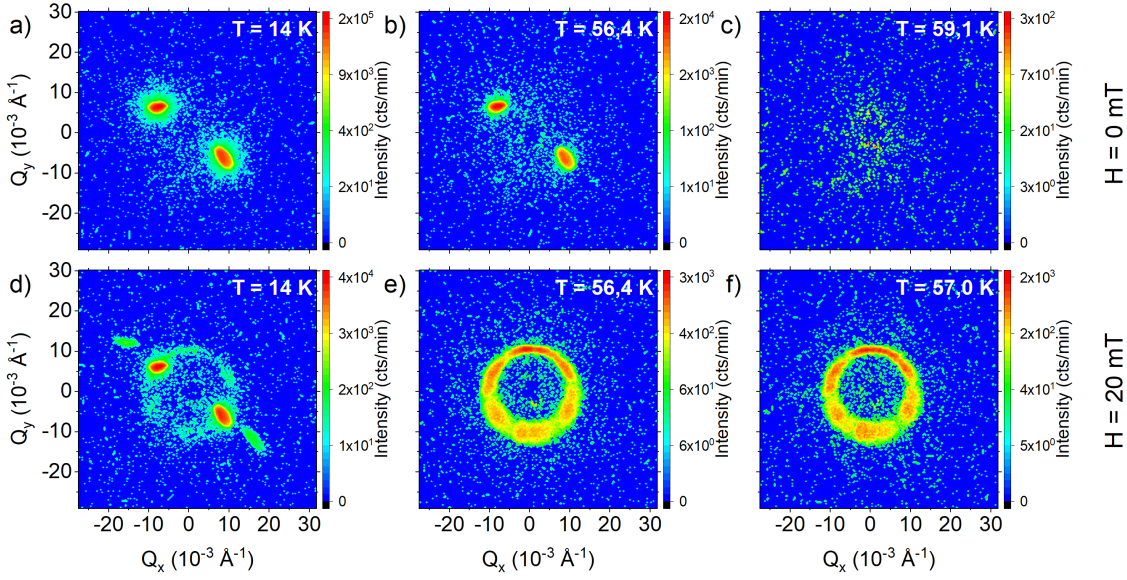


Figure 3.19: Selected SANS diffraction patterns from ZFC (top row) and FC (bottom row) measured upon Field Heating (FH) from Cu_2OSeO_3 when the neutron beam and magnetic field are applied parallel to the $\langle 110 \rangle$ axis in a, b, d) the spin helical, e, f) skyrmion and c) PM phases

orientation. Although, the higher intensity of the helical Bragg peaks with respect to the skyrmion peaks at $T = 14$ K and $H = 20$ mT along $\langle 110 \rangle$ suggests that the helical phase is more energetically favourable than the skyrmion states along this sample orientation, which could be consequence of a higher single ion magnetic anisotropy in the $\langle 100 \rangle$ crystallographic axis than in the $\langle 110 \rangle$ direction. To investigate this effect, more data were collected using FC/FH along the $\langle 110 \rangle$ sample orientation during increasing magnetic field sweeps instead of temperature sweeps due to experimental time constrains.

The spectra shown in Figure 3.20 seem to confirm that the effect of Field Cooling (FC) the sample across the centre of the high-temperature skyrmion phase along $\langle 110 \rangle$ is weaker than that of $\langle 100 \rangle$. The magnetic phase diagram obtained upon FC/FH the sample along $\langle 110 \rangle$ is shown in figure 3.21a) and compared to its $\langle 100 \rangle$ equivalent in panel b). Moreover, the magnitude of the scattering vector at the centre of the observed magnetic Bragg peaks is shown for the $\langle 110 \rangle$ and $\langle 110 \rangle$ sample orientations respectively in panels c) and d). Although the border of the observed magnetic phases is shifted with respect to the observations reported along $\langle 100 \rangle$ when measured along $\langle 110 \rangle$, this could

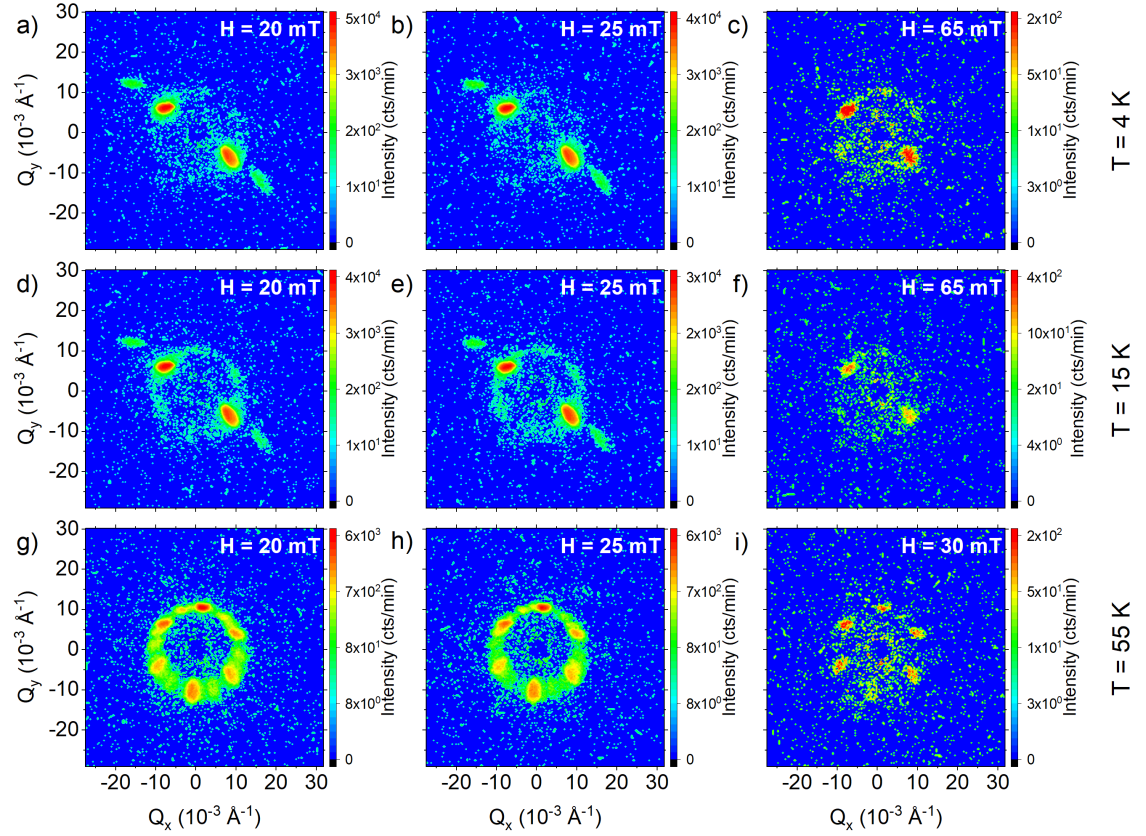


Figure 3.20: Selected SANS diffraction patterns from FC/FH Field scans at constant temperature on Cu_2OSeO_3 when the neutron beam and magnetic field are applied parallel to the $\langle 110 \rangle$ axis in a-f) a superposition of the spin helical and weak Field Cooled skyrmion features, and g-i) high-temperature skyrmion phases

be the result of different thermal protocols used: field sweeps along $\langle 110 \rangle$ and temperature sweeps along $\langle 110 \rangle$. Nonetheless, the appearance of low- and high-temperature skyrmion states along the $\langle 110 \rangle$ axis is noteworthy since this differs from the patterns observed upon FC/FH along all sample orientations other than $\langle 100 \rangle$. Furthermore, the neutron scattering intensity is higher when the $\langle 100 \rangle$ -alignment is used. These observations suggest that the stability of the low-temperature skyrmion state is enhanced when the magnitude of the easy-axis magnetic anisotropy reaches its maximum value, which corresponds to the applied magnetic field parallel to the $\langle 100 \rangle$ -crystallographic axis. On the other hand, significant changes in the magnitude of $|\vec{Q}|$ were induced as a consequence of the different sample orientations, with $\langle 100 \rangle$ developing slightly

higher values of $|\vec{Q}|$ than $\langle 110 \rangle$. In order to investigate the scaling behaviour of the spin structures along $\langle 110 \rangle$, let us examine the trends of selected temperature and magnetic field curves.

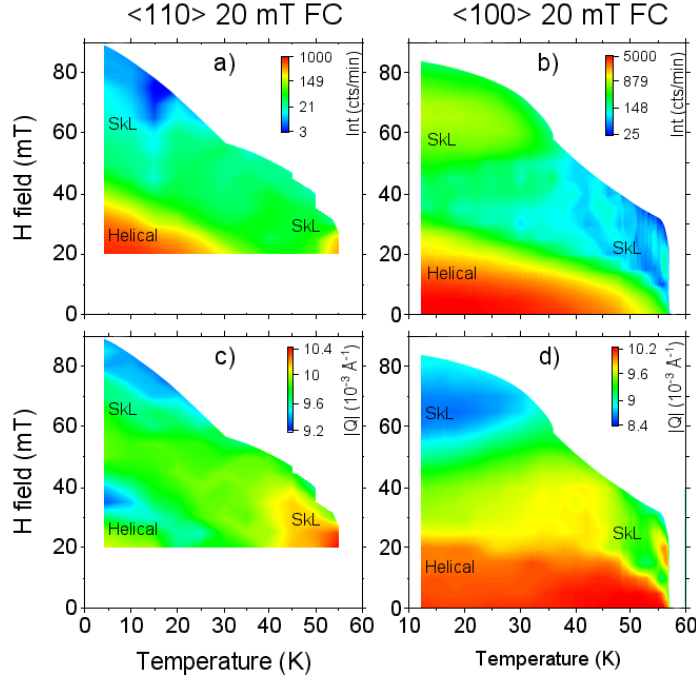


Figure 3.21: Comparison of the FC/FH magnetic phase diagrams (top row) and magnitude of $|\vec{Q}|$ (bottom row) for Cu_2OSeO_3 single crystals measured upon FC/FH along $\langle 110 \rangle$ (left) and $\langle 100 \rangle$ (right).

Figure 3.22 shows the temperature dependence of selected a) neutron scattering intensity, b) scattering vector, $|\vec{Q}|$, and c) magnetic textures spacing, λ , curves measured upon a fixed magnetic field with the $\langle 110 \rangle$ crystallographic axis parallel to the incident neutron beam and the applied magnetic field. The observed trends should be compared to the T -dependence along the $\langle 100 \rangle$ -axis (see figure 3.16). The patterns were collected upon ZFC/FH at $H = 0$ mT, and after FC/FH at $H = 20$ mT. The helical phase along $\langle 110 \rangle$ behaves similarly along $\langle 100 \rangle$: the scattering intensity reaches its maxima at lower temperatures and is quenched upon the transition a higher-T magnetic state both with and without an applied magnetic field. But, the intensity is higher upon no magnetic field, and is quenched at different temperatures: T_C under no applied magnetic field, whereas a substantial decrease happens at $T \sim 40$ K at $H = 20$ mT. On the other hand, the scattering vector magnitude, $|\vec{Q}|$, and the spacing, λ , obtain similar

values and temperature trends when compared to those observed along $\langle 100 \rangle$. In the spin-helical state, $|\vec{Q}|$ is approximately constant upon zero applied field until the sample temperature approaches T_C , at which $|\vec{Q}|$ sharply decreases, while at an applied magnetic field of 20 mT, $|\vec{Q}|$ exhibits a wiggle around $T \sim 40$ K and decreases before entering into the skyrmion state.

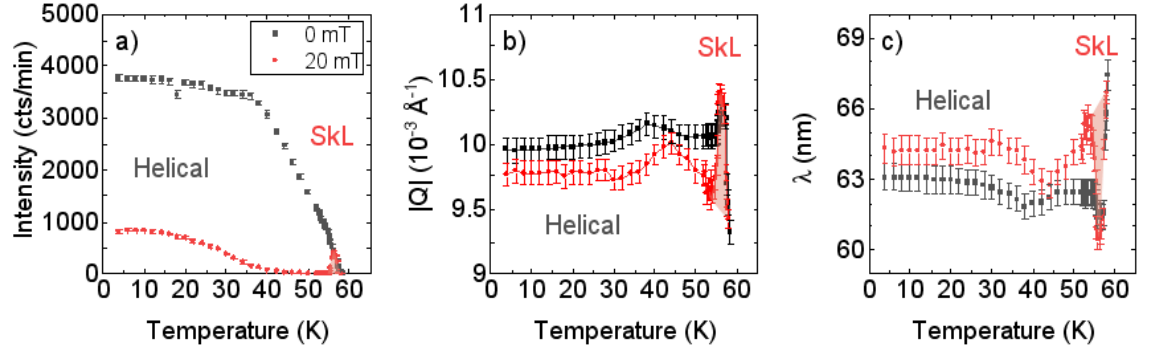


Figure 3.22: Temperature dependence of a) the neutron scattering intensity, b) the magnitude of the scattering vector, $|\vec{Q}|$, and c) the spatial periodicity of the magnetic lattices of Cu_2OSeO_3 measured using increasing temperature at selected constant magnetic fields when the neutron beam and the magnetic field are applied parallel to the $\langle 110 \rangle$ crystallographic axis upon ZFC/FH. The coloured areas indicate the region in which a skyrmion lattice was observed.

The temperature dependence of the high-temperature skyrmion lattice when the neutron beam and the magnetic field are applied parallel to the $\langle 110 \rangle$ crystallographic axis resembles all our previous observations when the neutron beam and the magnetic field are applied parallel to the $\langle 110 \rangle$ crystallographic axis $\langle 100 \rangle$ and for the random orientations examined. We notice the scattering intensity is higher when measured without an applied field than at $H = 20$ mT along the $\langle 110 \rangle$ sample orientation. Moreover, the temperature dependence of the intensity for the $\langle 110 \rangle$ sample orientation exhibits its maximum at base temperature. Similarly, the neutron scattering intensity at $H = 20$ mT reaches its maximum value at base temperature and decreases monotonically upon heating until the sample enters the skyrmion phase, in which the intensity increases to a local maximum (*i.e.* within the temperature range of the high-temperature skyrmion phase) around $T = 56.4$ K, and vanishes as the temperature of the sample reaches the paramagnetic phase transition temperature. On the other hand, only a small difference

was observed in the scaling behaviour of the helical phase upon changing the orientation of the sample: along both $\langle 110 \rangle$ and the first random sample orientation, when the neutron beam and magnetic field are applied parallel to the $\langle 110 \rangle$ axis, $|\vec{Q}|$ raises upon heating in the absence of applied magnetic fields, which implies the distance between the spin helices is reduced with increasing thermal energy.

3.4 Conclusions

Our data shows that the high-temperature skyrmion lattice appears perpendicular to the applied field along all sample orientations, which suggests this state is stabilised by temperature fluctuations alone. Our experiments also suggest that the helical phase could develop along all sample orientations, but the spin stripes have a preferential orientation. Moreover, we found the low-temperature skyrmion lattice depends strongly upon sample orientation, and its features remain almost constant through a wide range in temperature, but not upon variations in field. Thus, we may associate the nucleation of the low-temperature skyrmion phase with magnetic anisotropic terms.

Light induced effects, tellurium doping, and magnetic stability in Cu_2OSeO_3

In the previous chapter, we investigated the effect of different sample orientations and thermal protocols (see figure 3.2 and section 3.1) in the emergence of long-range magnetic order in Cu_2OSeO_3 . In this chapter, we aim to investigate the effect of illuminating the sample using visible light, the effects of applying internal pressure via atomic substitution, *i.e.* upon tellurium doping, and the time-stability of the observed magnetic features, which provide valuable insight into the energetic balance of the quantum magnetic interactions in the multiferroic skyrmion host material Cu_2OSeO_3 . The first section of this chapter is the main focus of my research, and the following two sections are part of a joint effort with the team of Prof. Tilo Soehnel at the University of Auckland.

4.1 Light-induced magnetic effects in Cu_2OSeO_3

The Small Angle Neutron Scattering experiments reported in sections 3.2 and 3.3 were performed along different orientations, where we observed that the scattering intensity across the spin-helical, low- and high-temperature skyrmion phases is optimised when the incident neutron beam and the applied magnetic field are

parallel to the $\langle 100 \rangle$ axis of the sample. Hence, we selected this geometry to investigate the light-induced phenomena and magnetic stability in Cu_2OSeO_3 single crystals. Note that the possibility to manipulate skyrmions by light was first experimentally discovered by C. Ulrich and our collaborators in the group of Prof. M. Ruebhausen at the Centre for Free Electron Laser Science (CFEL) and the University of Hamburg in Germany.

The manipulation of magnetic skyrmions achieved by illuminating the sample with ultra-fast laser radiation [258–264], applying alternating electric/magnetic fields or field gradients [235, 255, 265–273], together with the findings of the microwave resonant collective excitations of the conical and skyrmion states of Cu_2OSeO_3 [274–276], and the light-induced phase transitions in topological materials provide a few precedents of the effects of electromagnetic radiation in the optical region of the spectrum on the long-range spin ordered states of the magnetoelectric material Cu_2OSeO_3 [277, 278]. Hence, we performed a series of Small Angle Neutron Scattering experiments utilising a modified sample holder, and accumulated data under different light conditions to determine the effect of different wavelengths and light intensity in the phase diagram and the stability of the skyrmion phases of Cu_2OSeO_3 along two different sample orientations.

Let us start describing the custom optical setup developed in collaboration with Dr. Norman Booth at ANSTO. A tunable illumination setup was designed and arranged at the UNSW (see figure 4.1), and brought into ANSTO. The optical components of this light setup can be used to select a narrow range of wavelengths by exchanging the fibre adaptor by a monochromator grating with 1800 lines/mm and re-locating the optical fibre adaptor accordingly (not shown) [283, 284]. After aligning the optical elements in the illumination system, the light-spectra were collected using an Ocean Optics Maya 2000 spectrometer attached to the optical fibre adaptor, and the optical power was measured with care at the position of the sample after it has been reflected by the polished Aluminium mirror shown in figure 4.1a. Figure 4.2 shows the normalised intensity over the optical range for a selected set of spectra with their maxima centred within the visible range, where the positions of the centre of the peaks were selected using the monochromator setup and the dashed curve reflects the output of the Xenon

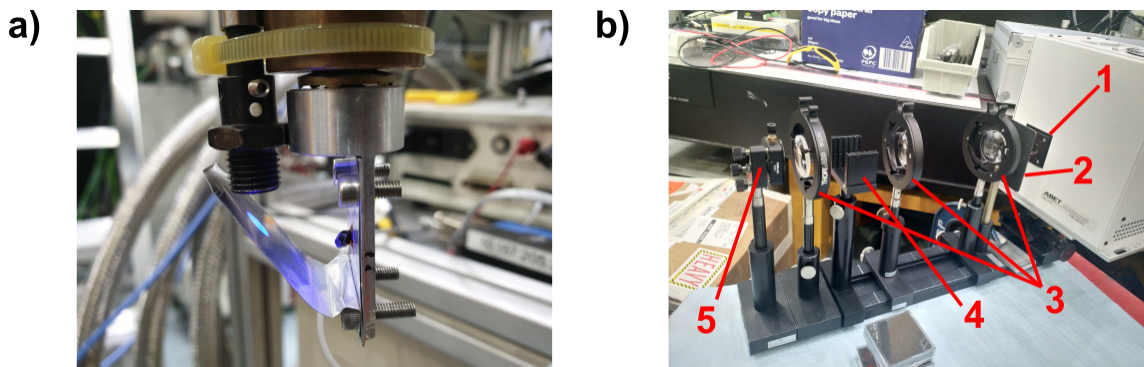


Figure 4.1: A tunable optical setup used in our SANS experiments consists of: a) an optical fibre installed inside the cryostat down to the sample stage, where the light is reflected onto the sample by a mirror made of polished Aluminium foil [279], and b) a custom made illumination system using (1) a Xenon arc-lamp [280], (2) a mechanical diaphragm (iris blend) to control the optical power applied to the optical components, (3) convex optical lenses [281], (4) optional neutral density filters to control the optical power [282], which is collected at (5) an optical fibre adaptor.

arc-lamp (white light) whose intensity is higher in the infrared region but contains contributions up to the ultraviolet region of the spectrum. Unless otherwise stated, the optical power was kept at a constant 5 mW at the sample position during the experiments.

The tunable light setup was connected to the cryostat through an optical fibre by Dr. Norman Booth and the sample environment team at ANSTO [285, 286]. Table 4.1 reports the optical power at the entrance of the cryostat and at the sample position inside the cryostat as measured using a Thorlabs laser power meter, which has a special measurement mode for the integration of the total light intensity over a wavelength range from 350 to 1050 nm. Table 4.1 also reports the linewidth of the patterns in figure 4.2. In order to determine if exposing the sample to light induces any effect on the magnetic phases of Cu_2OSeO_3 , we first aligned the sample along the $\langle 100 \rangle$ crystallographic axis and performed a series of temperature dependent scans following the ZFC/FH thermal procedures outlined in figure 3.2 (see explanation of “thermal procedures” in section 3.1) across the entire magnetic phase diagram. These measurements were performed first in the dark and followed by their equivalent with the sample exposed to white light

illumination in the cryostat. The results are shown in figure 4.3

Mean wavelength (nm)	HWHM (nm)	P_{cryo}^{in} (mW)	P_{cryo}^{sample} (mW)
400	10	14	2
500	15	30	10
600	15	36	14
700	15	32	13
800	20	24	10
900	20	220	110
350–1050 range	–	1230	610

Table 4.1: Parameters and integrated power of the light spectra used in our SANS experiments at QUOKKA measured using a Thorlabs laser power meter outside of the cryostat and at the position of the sample. Notice, the laser power meter has a special function to measure the light intensity for a broad spectrum over the entire visible range.

At first glance, the magnetic phase diagrams measured (panel a) in figure 4.3) in the dark and (panel b) under light resemble much. However, a difference of approximately $\pm 2\%$ in the neutron scattering intensity becomes evident when we subtract the neutron scattering intensity measured in the dark from its equivalent measured under light illumination as seen in panel c). We noticed that light illumination affects in different ways the spin-helical state, the low- and high-temperature skyrmion lattices. The low-temperature skyrmion lattice undergoes a small reduction in intensity, the helical phase a stronger intensity reduction, and the high-temperature skyrmion lattice exhibiting both an intensity reduction and increase. Moreover, the magnitude of the scattering vector measured (panel d) in the dark and (panel e) under light exposure were subtracted (see panel f) to unveil a change of up to $\pm 10\%$ in the value of $|\vec{Q}|$.

The different response from these three magnetic phases motivated us to perform ZFC/FH temperature scans at $H = 0, 20$ and 65 mT using light with different wavelengths. Figure 4.4 summarises the effect of illuminating the sample with light of different wavelengths across the helical (left column), high-temperature skyrmion (centre column), and low-temperature skyrmion (right

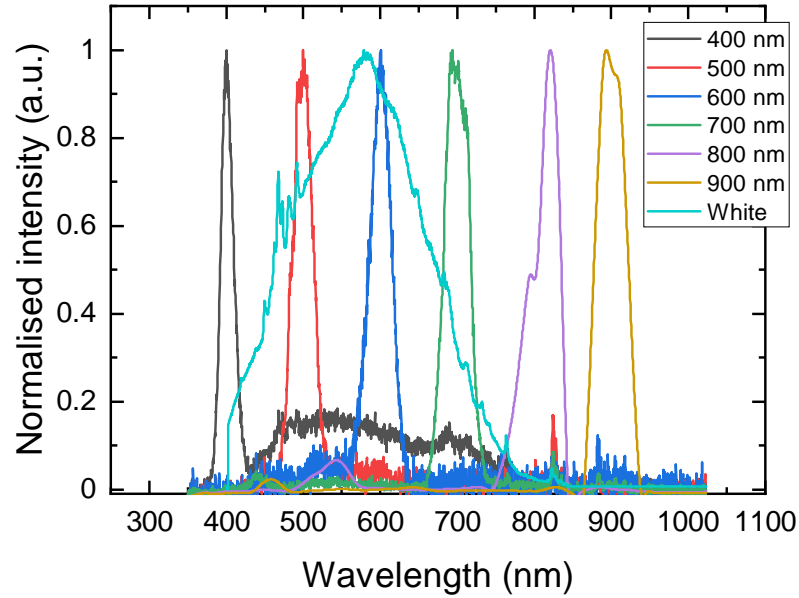


Figure 4.2: Light spectra used in our SANS experiments collected in 10 milliseconds with an Ocean Optics Maya 2000 spectrometer. Each spectra were recorded using a colourless short-pass KG3 filter to absorb infrared radiation and a neutral density filter. Note: the term “White light” refers to the spectrum of the Xe-Arc lamp with a KG3 filter.

column) phases of Cu_2OSeO_3 . The scattering intensity shows a temperature shift that depends on the wavelength of the applied beam of light. Near infrared light at 695 nm induces no temperature shift of the helical to PM (57.0 ± 0.2 K), high-temperature skyrmion to PM (57.0 ± 0.2 K) or low-temperature skyrmion melting transitions measured in the dark (not shown). However, 515 nm light shifts the phase transition temperatures by -0.3 K at $H = 0$ mT but not shift is observed at $H = 20$ mT; and 280 nm light induces a temperature shifts of -0.3 K at $H = 0$ mT, -0.6 K at $H = 20$ mT and -0.3 K at $H = 65$ mT. Notice that the illumination intensity of these measurements was fixed at 20 mW at the entrance of the optical fibre, which renders 5 mW at the sample position. Furthermore, the temperature shift is confirmed by the corresponding behaviour of $|\vec{Q}|$.

Next, let us consider the results of keeping the temperature and magnetic field constant and changing the wavelength of the electromagnetic radiation applied to the sample. Here, we used a set of longpass optical filters (which block light transmission below an edge, also known as cut-on wavelength, *i.e.*, a filter with higher cut-on blocks more light than a filter with lower cut-on wavelength) to

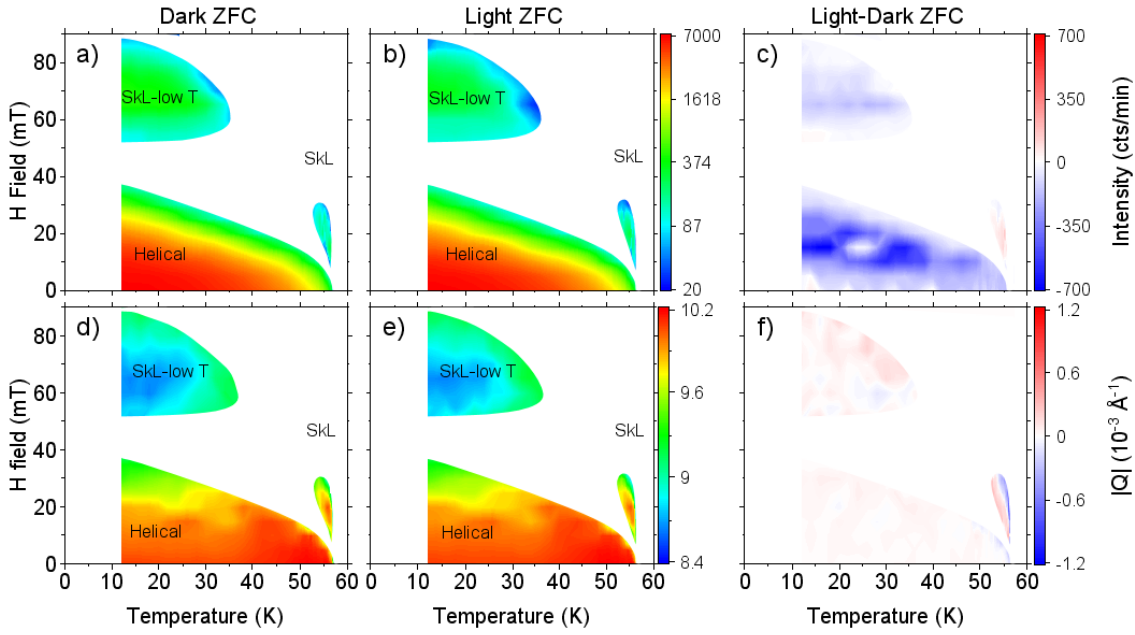


Figure 4.3: The (top row) magnetic phase diagrams and (bottom row) magnitude of the scattering vector, $|\vec{Q}|$, from our SANS experiments performed upon ZFC/FC (left column) without light illumination, *i.e.* in the dark, and under (centre column) white light illumination. The effects of light illumination become more evident when we (right column) subtract the results obtained in the dark from those measured using light.

select a portion of the light-spectrum [282]. Note, since the intensity of light was not adjusted, different long-pass filters also change the total intensity of light. Figure 4.5 shows the effects of selecting increasing filter cut-ons on the intensity and scattering vector measured upon ZFC/FH in three different magnetic phases along $\langle 100 \rangle$. Panel a) reveals that the scattering intensity of these three magnetic phases responds differently upon applied illumination with a different wavelength range: the low-temperature skyrmion lattice remains unaffected regardless of the color of the applied illumination, whereas the scattering intensity in the helical phase grows linearly as broader regions of the spectrum are blocked, and the high-temperature skyrmion lattice manifests a non-linear wavelength dependence. In other words, the low-temperature skyrmion phase exhibits Bragg peaks of the same intensity upon ultraviolet, visible and infrared light; the scattering intensity in the helical phase decreases linearly as we move from a purely IR to a white spectrum that includes UV, but the inclusion of UV light does not add any

additional effect to the non-linear behaviour of the high-temperature skyrmion phase (see inset scattering patterns). Moreover, the intensity of the scattered patterns is weaker upon light exposure than when measured in the dark for the helical phase, but the opposite is true for the low-temperature skyrmion phase, while the scattered intensity of the high-temperature skyrmion phase reaches upon illumination both lower and higher values than in the dark. Additionally, panel b) shows the effects of selecting different cut-on wavelengths on the scaling of the observed magnetic Bragg reflections. Here, the low-temperature skyrmion phase remains unchanged, while the scattering vector, $|\vec{Q}|$, grows linearly with increasing cut-on wavelength, and exhibits two regimes in the high-temperature skyrmion phase: i) in the lower cut-on wavelength range, a nearly constant $|\vec{Q}|$ appears as a diffuse scattering ring is measured, and ii) a quick change of $|\vec{Q}|$ occurs in the lower cut-on wavelength range and manifests the stabilisation of a long-range skyrmion order, as seen in the appearance of well defined magnetic Bragg reflections (see insets in both panels).

In order to determine if the wavelength dependent observations are related to the change in light intensity, we performed a series of measurements using light illumination – centred at two different wavelengths: 400 and 800 nm, which were carefully selected using a monochromator in our optical setup – and different neutral density optical filters. These measurements were performed under ZFC/FH upon no previous light exposure at a fixed temperature of $T = 55.5$ K, and an applied magnetic field of $H = 20$ mT. Figure 4.6 shows the a) neutron scattering intensity and b) scattering vector resulting from accumulating data between 0.12 and 12 mW of applied illumination power.

The scattering intensity (see figure 4.6a) decreases about 40% when the sample is illuminated by both violet (400 nm) and near infrared (800 nm) light. We noticed that the scattering intensity decreases almost linearly upon increasing optical power, and remains constant upon decreasing optical power regardless of the wavelength of the light (see the discussion of related time-evolution in section 4.3). Moreover, this large change in the intensity only induces small changes in the values of $|\vec{Q}|$ (see panel b) of figure 4.6), which is slightly reduced upon increasing light intensity and remains almost constant upon decreasing the light

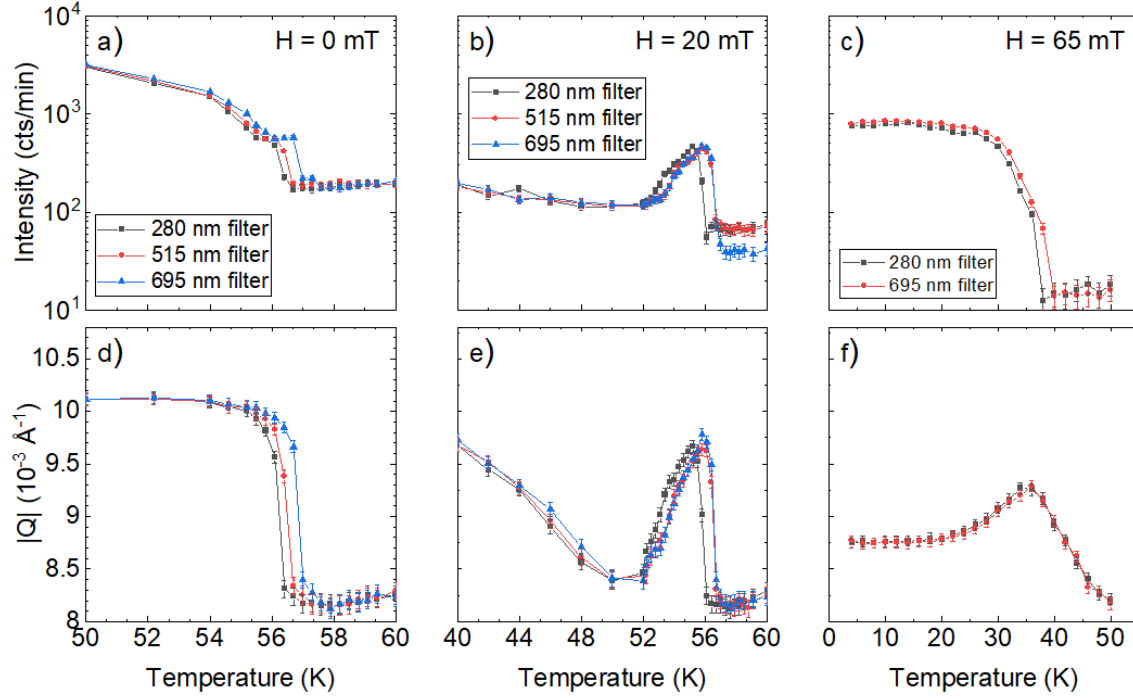


Figure 4.4: Wavelength effect on the (top row) scattering intensity and (bottom row) $|\vec{Q}|$ from selected temperature scans performed upon ZFC/FH and using an applied magnetic field of (left column) $H = 0$ mT for the helical phase, (centre column) 20 mT for the high-temperature skyrmion phase, and (right column) 65 mT for the low-temperature skyrmion phase.

intensity, and varies within typical values of the scattering vector in the high-temperature skyrmion phase ($\approx 9.75 - 10.25 \times 10^{-3} \text{ \AA}^{-1}$).

The series of temperature scans taken under illumination at different wavelengths (see figure 4.4), wavelength dependent measurements at fixed temperature, field and light intensity (see figure 4.5), and the dependence on the light intensity at fixed T , H , and wavelength manifest a different behaviour than the time-dependent magnetic relaxation processes reported in section 4.3. Particularly, we should consider that the scattering intensity measured at $T = 55.6$ K and $H = 20$ mT (panel a) in figure 4.9) grows more than one order of magnitude in less than five minutes and reaches a stable value at its maximum, whereas the scattering intensity measured upon illuminating the sample with different light colours at $T = 55.7$ K and $H = 20$ mT (see figure 4.5) grows much slower and only when the filter cut-on frequency exceeds 375 nm, and the scattering intensity measured at $T = 55.5$ K and $H = 20$ mT upon exposing the sample to violet and

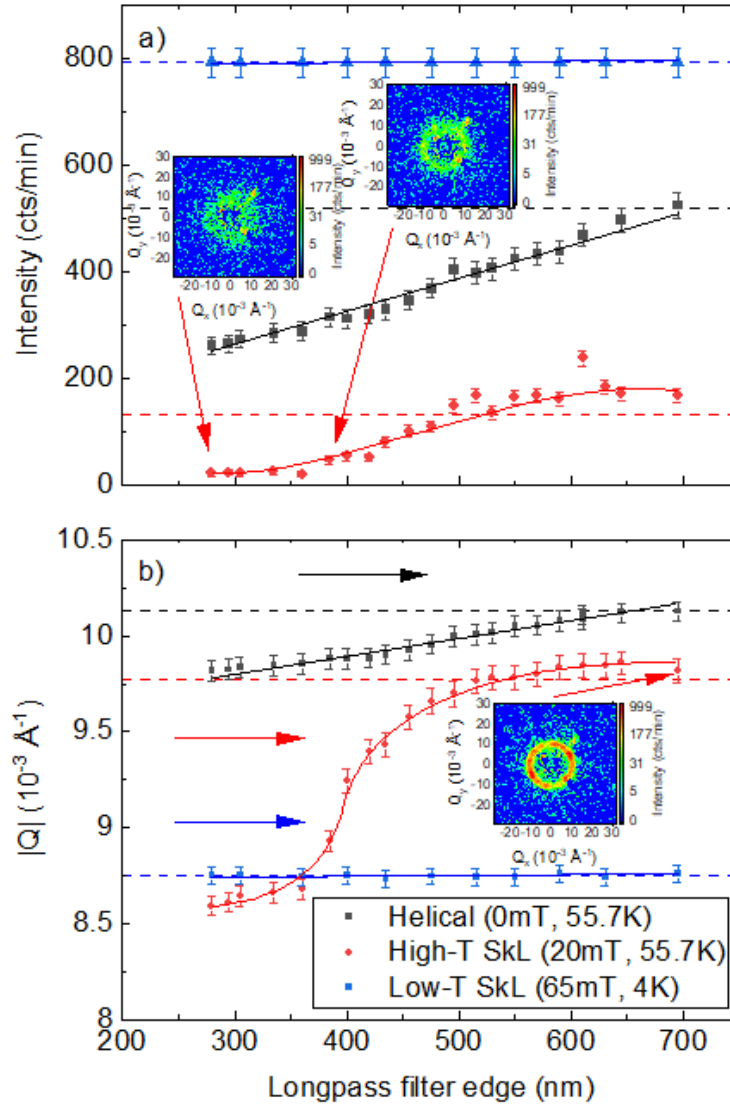


Figure 4.5: Wavelength effect on the a) scattering intensity and b) scattering vector $|\vec{Q}|$ from $\langle 100 \rangle$ -orientated Cu_2OSeO_3 at fixed temperature and field. The insets in a) show selected scattering patterns from the high-temperature skyrmion phase. The solid lines in both panels are guides to the eye, and the dashed lines indicate the values of the intensity and \vec{Q} measured at the same temperature, and field, but in the dark and without previous illumination. The coloured arrows indicate the order in which the optical filters were selected.

infrared illumination decreases as a function of light intensity.

These light-induced observations are not only a reminder of the photomagnetic effects (magnetic response to light, not to be confused with the magneto-optic effect: change in light interacting with a magnetic material) observed in ferrites or gold nanoparticles [287–291], but most importantly observed on the

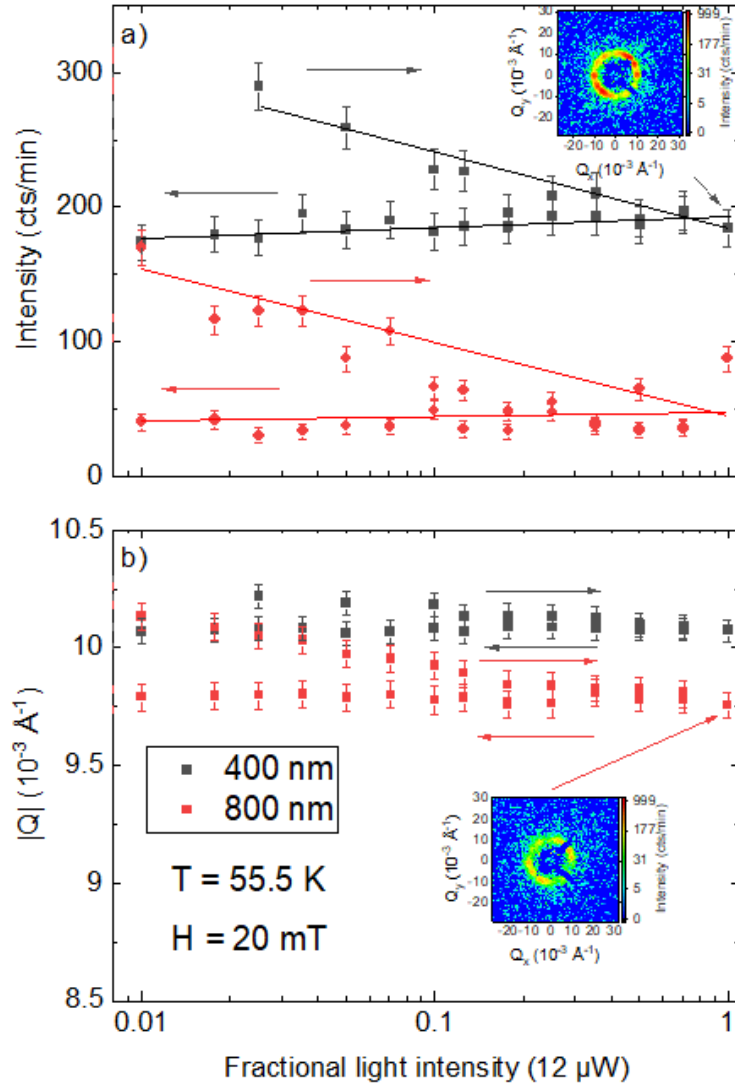


Figure 4.6: Effect of changing the light intensity on the a) scattering intensity and b) scattering vector $|\vec{Q}|$ from $\langle 100 \rangle$ -orientated Cu_2OSeO_3 at fixed $T = 55.5 \text{ K}$ and $H = 20 \text{ mT}$ after ZFC/FH. The insets in a) show selected scattering patterns from the high-temperature skyrmion phase under 12 mW of optical power. The arrows indicate the direction of the optical power sweeps.

skyrmion host materials FeGe, TbFeCo, Ta/Fe₇₂Co₈B₂₀/TaO_x tri-layers, and Cu₂OSeO₃ using high-frequency lasers or microwave radiation [260, 261, 263, 264, 274]. Although room temperature creation and annihilation of skyrmions has been achieved using ultra-fast pulses (35 fs) in thin films of ferromagnetic Ta/Fe₇₂Co₈B₂₀/TaO_x ($\approx 51 \text{ \AA}$ thick) – a crucial requisite for skyrmion and optical computing devices, this is the first time the manipulation of skyrmion lattices has been achieved with light, to the best of our knowledge [261, 292, 293].

Here, the energy of the absorbed visible photons seems to be large enough to impact the energy balance between two different magnetic states. However, the photomagnetic effects on Cu_2OSeO_3 could be superposed onto certain degree of light-induced heating, which has been associated by Yu *et al.* and Je *et al.* with changes in the skyrmion dynamics of Cu_2OSeO_3 , and would make the photomagnetism of Cu_2OSeO_3 similar to that of $\text{Ta}/\text{Fe}_{72}\text{Co}_8\text{B}_{20}/\text{TaO}_x$ [261, 294]. In a final step, it should be determined whether sample heating caused by light illumination is the reason for the observed effects or not. Therefore, the sample could be replaced by a temperature sensor and the light experiments could be repeated at the identical conditions, *i.e.* sample temperature and field, and the illumination with light at the same intensity and wavelength. Furthermore, the effective temperature of the sample inside a cryostat could be determined using the detailed balance of Stokes and Anti-Stokes phonon modes in its Raman spectrum (although this could be beyond the sensitivity of a Raman setup and the cooling power of different cryostats would be different) or alternative methods.

4.2 SANS on tellurium-doped Cu_2OSeO_3

Atomic substitution has been extensively utilised to investigate the role of a particular species in the electronic correlations of solids, and to induce chemical pressure due to the difference in atomic radii within a unit cell. For example, structural changes have been described through the Goldschmidt tolerance factor and the ionic filling fraction in perovskites and arbitrary ionic compounds respectively [295, 296]. The effects of atomic substitution are not constrained to structural phase transitions. They also affect the electronic band structure leading to changes in the magnetic correlations of magnetic or superconducting materials [297–300]. In the case of Cu_2OSeO_3 , it has been suggested that atomic substitution induces chemical pressure, stabilises the skyrmion phase in an extended temperature range, changes the effect of magnetic anisotropy terms, and enhances metastable skyrmions lifetime associated with an energy barrier in Zinc doped Cu_2OSeO_3 single crystals [301–306]. Notice, zinc and copper ions carry different

magnetic moments, thus this atomic substitution induces magnetic doping.

The partial substitution of copper by nickel in Cu_2OSeO_3 (notice that nickel ions carry a magnetic moment different than that of copper ions, thus this atomic substitution induces magnetic doping) has been associated with position-dependent skyrmion lifetime that are larger than in pristine Cu_2OSeO_3 , and an increased role of the demagnetisation effects [307, 308]. Additionally, it has been suggested that both substituting Copper by Silver and Oxygen by Sulphur increases the temperature range of the skyrmion phase towards lower temperatures in powdered Cu_2OSeO_3 , but this wider skyrmion temperature range could also be the result of the change in dimensionality of the crystallites as it has been reported in thin slabs of Cu_2OSeO_3 reduced from single crystals [5, 76, 309, 310]. With these precedents in mind, this section reports our investigation on the magnetic effects of inducing chemical pressure by substituting selenium by tellurium atoms in Cu_2OSeO_3 single crystals. Notice both selenium and tellurium are isoelectronic, *i.e.*, they carry the same magnetic moment and the effect of Te-doping is internal (chemical) pressure.

Te-content *	Space group	Lattice constant a (Å)	Unit cell volume (Å ³)
0.00	$P2_13$	8.9191(4)	709.53(9)
0.05	$P2_13$	8.92362(16)	710.596(22)
0.10	$P2_13$	8.92706(26)	711.420(35)
0.15	$P2_13$	8.93132(25)	712.438(35)
0.20	$P2_13$	8.93545(28)	713.427(38)
0.30	$P2_13$	8.94540(47)	715.814(65)
0.40	$P2_13$	8.94483(76)	715.6(1)
0.50	$P2_13$	8.94436(93)	715.56(13)

Table 4.2: Lattice parameters of the Te-doped Cu_2OSeO_3 series used in our experiments. This data were measured at room temperature by our collaborators at the University of Auckland via powder X-Rays Diffraction (data from [76, 110]).

Single crystals of $\text{Cu}_2\text{OSe}_{1-x}\text{Te}_x\text{O}_3$ were grown by our collaborators Rosanna

*Nominal tellurium content of the samples from the stoichiometric proportion of the precursors. For a discussion of the effective tellurium content of the samples, see section 5.2.

Rov and Luis Ealdama under the supervision of Prof. Tilo Soehnel at the University of Auckland. To this end, the Chemical Vapour Transport method (see section 2.1 and reference [76]) was used with CuO , SeO_2 , and TeO_2 as precursors in stoichiometric proportions, NH_4Cl as transport agent, and the temperatures of the hot and cold head of the furnace were set at 610 and 540 °C. Room temperature powder X-Rays Diffraction (XRD) were performed at the University of Auckland using the K_α edge of an Ag source ($\lambda = 0.56087 \text{ \AA}$) in a commercial Rigaku Oxford Diffractometer, and confirmed that the unit cell of all samples are described by the $P2_13$ space group (see table 4.2). Notice, the lattice constant, a , increases linearly with higher Tellurium concentrations, x , in $\text{Cu}_2\text{OSe}_{1-x}\text{Te}_x\text{O}_3$ within $0 \leq x \lesssim 0.30$ and remains approximately constant for $0.30 \lesssim x \lesssim 0.50$, which could suggest a saturation of the effective x in the crystals. Our Raman scattering results on $\text{Cu}_2\text{OSe}_{1-x}\text{Te}_x\text{O}_3$ single crystals reveals evidence of the effective tellurium content of the samples. Here, a systematic shift towards lower energies upon increasing nominal tellurium content was observed in phonon modes associated with the vibration of SeO_3 units. A first approximation to the effect of changes in the effective mass of the $\text{Se}_{1-x}\text{Te}_x\text{O}_3$ units upon Te-doping gives us effective contents of $3.0 \pm 0.3 \%$, $3.7 \pm 0.4 \%$, and $4.5 \pm 0.5 \%$ for the samples with nominal Te-contents of 10 %, 30 %, and 50 %, respectively (see table 5.1 and section 5.2).

The presence of Tellurium in our samples was confirmed using Energy Dispersive X-ray Spectroscopy (EDX), which demonstrated that the dopant is uniformly distributed throughout the crystals (see supplement in ref. [76]). However, the EDX measurements did indicate that the final Tellurium content in the single crystals is significantly smaller than the nominal Te-content from the starting materials. It is about a factor of 10 smaller, but due to the limited resolution of the EDX technique further experiments are required using other analytic methods (see discussion in section 5.2). Moreover, we performed neutron Laue diffraction on the Te-doped samples at the instrument KOALA at ANSTO (publication in preparation).

We performed Small Angle Neutron Scattering upon ZFC/FH on randomly orientated samples of $\text{Cu}_2\text{OSe}_{1-x}\text{Te}_x\text{O}_3$ with $x = 0.0$ (see section 3.2), 0.05, 0.10, 0.20 and 0.50 nominal doping using the same methods outlined in sections 2.2.5

and 3.1. In the pristine compound, Cu_2OSeO_3 , the dominating propagation direction of the helical phase is determined by the magnetic anisotropy terms along the $\langle 100 \rangle$ axes [77, 78, 80]. Moreover, we observed secondary neutron reflections throughout the doping series – due to intense neutron scattering at base temperature and upon field heating at $H = 20$ mT (see for example figure 3.12) – that suggest the formation of robust spin helices is not perturbed by non-magnetic atomic substitutions. Therefore, we conclude that the change in the lattice parameters upon partial substitution of the selenium ions of Cu_2OSeO_3 with tellurium does not affect significantly the magnetic anisotropy of the system.

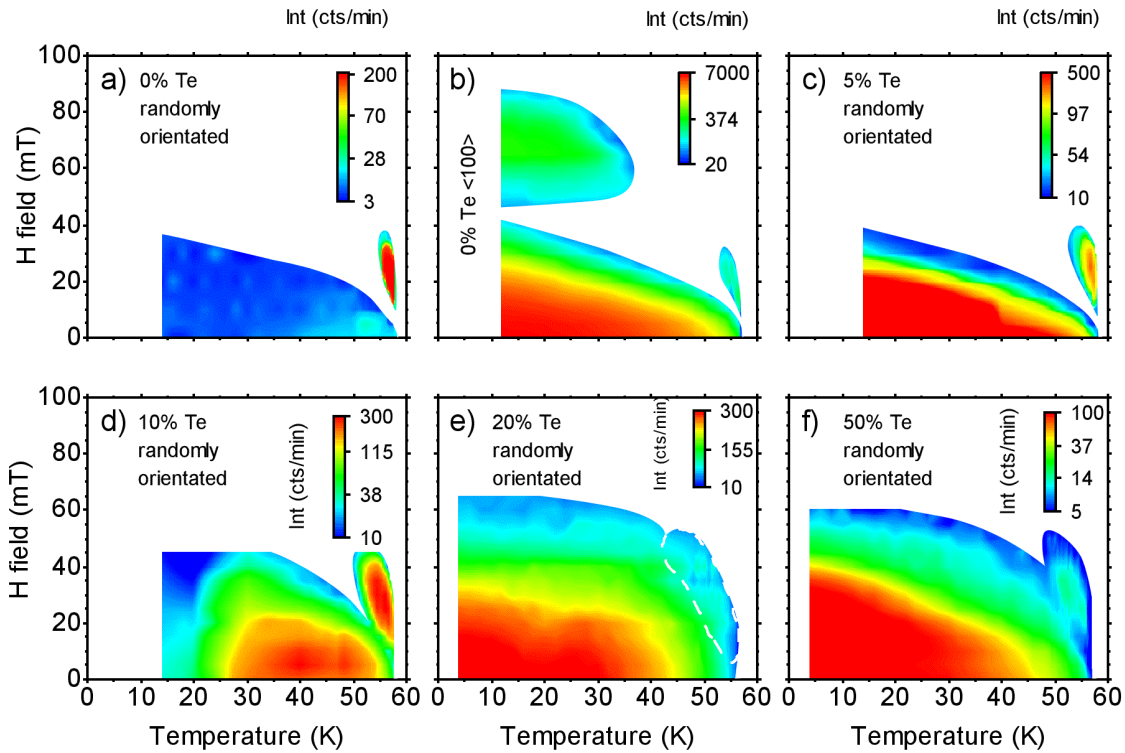


Figure 4.7: Magnetic phase diagrams of Te-doped Cu_2OSeO_3 single crystals from SANS upon ZFC/FH. Panels a) and c-f) show the SANS data from randomly orientated samples, while panel b) shows the SANS results from the $\langle 100 \rangle$ orientated sample.

The phase diagrams of the doping series measured upon ZFC/FH are shown in figure 4.7 along (panels a, c-f) random orientations and compared to the phase diagram of (panel b) pristine Cu_2OSeO_3 along $\langle 100 \rangle$. Here, we notice that the high-temperature skyrmion phase was clearly detected in the $x = 0.0, 0.05, 0.10, 0.20$ and 0.50 single crystals of $\text{Cu}_2\text{OSe}_{1-x}\text{Te}_x\text{O}_3$. This suggests that

this magnetic phase is not suppressed by tellurium doping. Furthermore, the low-temperature skyrmion phase was clearly observed upon 20 % of tellurium doping (not shown), which suggests that this magnetic phase also persists upon atomic substitution. However, further experiments are planned to determine if the low-temperature skyrmion phase appears upon doping under FC at 20 mT/FH throughout the doping series, and to determine the sample orientation dependence of the phase diagram. Let us briefly inspect the contour plots of $|\vec{Q}|$ for the doping series. Figure 4.8 shows that the main trends in the temperature- and field-dependent $|\vec{Q}|$ behaviour remain approximately unchanged upon increasing tellurium concentrations in $\text{Cu}_2\text{OSe}_{1-x}\text{Te}_x\text{O}_3$.

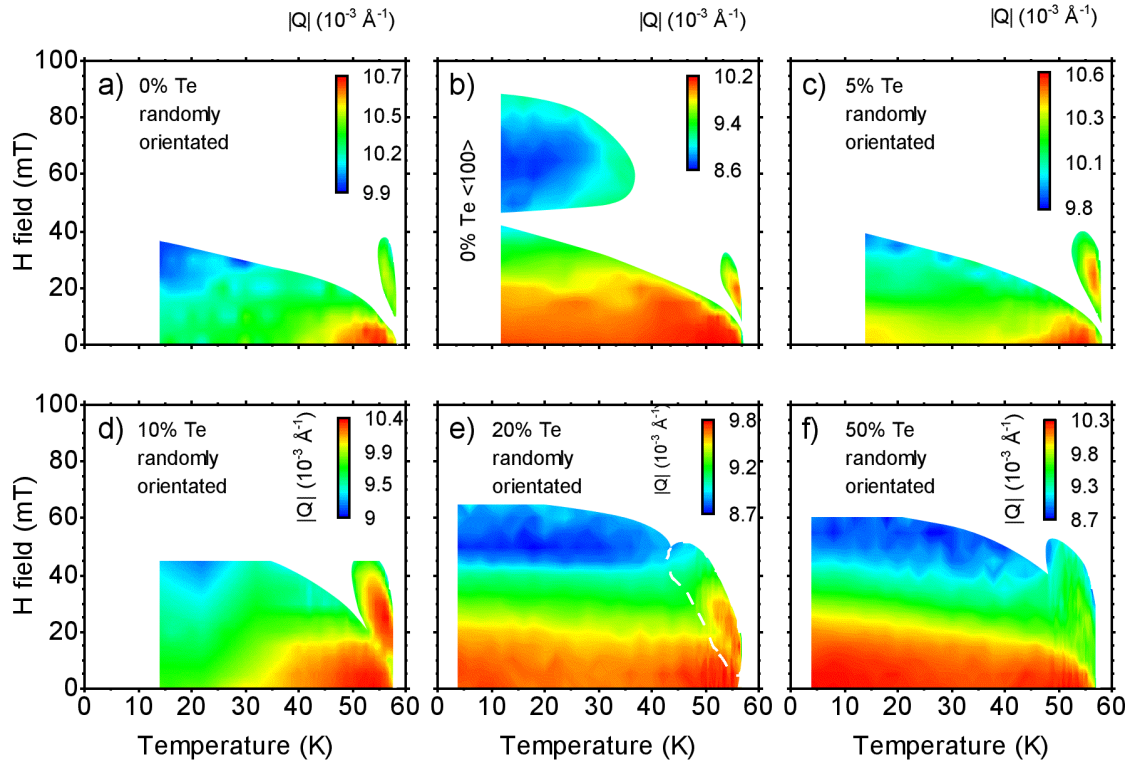


Figure 4.8: Contour plots of the scattering vector of the magnetic Bragg peaks from Te-doped Cu_2OSeO_3 single crystals observed through SANS upon ZFC/FH.

Finally, a careful examination of the scattering patterns for each doping level allowed us to determine the temperature and magnetic field range in which the high-temperature skyrmion phase is observed throughout the doping series. When we measure the SANS spectra upon ZFC/FH upon an applied magnetic field of $H = 20$ mT (across the centre of the skyrmion pocket), the temperature range of the high-temperature skyrmion range goes from $T = 55.3$ K to 57.9 K in

pristine randomly orientated Cu_2OSeO_3 , from 54.3 K to 57.9 K in the nominal 5 % Te-doped sample, from 53.1 K to 57.9 K in the nominal 10 % Te-doped sample, from 50.5 K to 57.0 K in the nominal 20 % Te-doped sample, and from 52.2 K to 56.5 K in the nominal 50 % Te-doped sample. Moreover, the phase diagrams indicate that the magnetic field range measured upon ZFC/FH at a constant temperature of $T = 56.1$ K (across the centre of the high-temperature skyrmion phase) goes from $H = 15$ mT to ≈ 38 mT in the pristine randomly orientated Cu_2OSeO_3 , from 14 mT to 39 mT in the nominal 5 % Te-doped sample, from 11 mT to 39.5 mT in the nominal 10 % Te-doped sample, from 10 mT to 40 mT at a temperature of 54.7 K in the nominal 20 % Te-doped sample, and from 15 mT to 40 mT at a constant temperature of 54.7 K in the nominal 50 % Te-doped sample. Hence, the evidence suggests that both the temperature and magnetic field range systematically increase upon higher nominal tellurium concentrations up to 20 %, but decrease when the nominal tellurium content is 50 %, which suggests that chemical pressure makes the high-temperature skyrmion phase energetically favourable in a broader temperature range (see discussion of Te-doping in section 5.2).

4.3 Time evolution of skyrmions and spin helices

To determine the time-stability of the long-range spin order of Cu_2OSeO_3 , in a tight collaboration with the research team of Prof. Tilo Soehnel at the University of Auckland, we collected SANS spectra at a constant temperature and magnetic field once the sample had reached the desired temperature and field within 0.2 K and 1 mT, respectively, and recorded data for approximately one minute per file. Moreover, the small deviations in the temperature, field and time from their expected values were extracted from the detector read-outs in the raw HDF files.

Figure 4.9a) shows a time series of approximately 50 scattering patterns collected upon ZFC/FH at a constant field of $H = 20$ mT and a temperature set at $T = 55.6$ K, in which the scattering intensity and magnitude of $|\vec{Q}|$ have been determined through Gaussian curve fitting routines. This temperature and magnetic field values were selected close to investigate the transition from the spin-

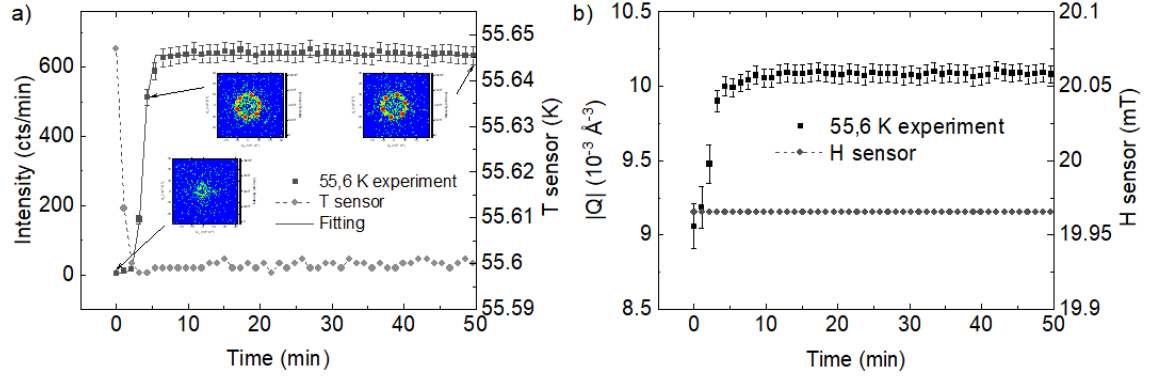


Figure 4.9: The SANS time evolution of $\langle 100 \rangle$ -orientated Cu_2OSeO_3 at $T = 55.6 \text{ K}$ and $H = 20 \text{ mT}$ reveals a) fluctuations in the neutron scattering intensity (black squares) upon minuscule fluctuations in the temperature of the sample as measured by the temperature sensor of the cryostat (small grey circles), and b) the scaling of the scattering vector (black squares) and the effective applied field (small grey circles). The continuous and dashed lines in a) show the curve fitting (discussed in the main text) of the intensity and the trend of the temperature, respectively. The insets show selected spectra with the observed Bragg peaks.

helical to the high-temperature skyrmion lattice states. Remarkably, the time series start with no magnetic Bragg peaks and after a few minutes a six-fold pattern with twelve magnetic Bragg reflections appears (see inset images) even though all the external stimuli remained unchanged. As a result, the scattering intensity (black squares) exhibits a sudden increase upon the emergence of long-range magnetic order.

In order to determine if the observed phenomenon is associated with a sizeable change in temperature, we extracted the temperature of the sample as recorded by the sensor in the cryostat (black circles). However, the change in temperature is below 10 mK and follows a decreasing trend (dashed line) that would indicate a minuscule reduction in the skyrmion-stabilising thermal fluctuations. Before fitting and discussing the time-dependent intensity, let us see the changes in $|\vec{Q}|$ and the applied magnetic field value recorded by the instrument.

Panel b) in figure 4.9b) shows the time evolution of $|\vec{Q}|$ from data collected at $H = 20 \text{ mT}$ and $T = 55.6 \text{ K}$. The resulting trend resembles the sharp scaling behaviour observed upon skyrmion phase transitions in chapter 3. Note, the val-

ues corresponding to the first few scattering patterns in figure 4.9 contain very weak magnetic Bragg reflections until a six-fold patterns develops after a few minutes. Moreover, panels a) and b) reveal that the changes in temperature and magnetic field are negligible compared to the scale of the regions in the phase diagram of $\langle 100 \rangle$ -orientated Cu_2OSeO_3 (see figure 3.13), and these variables can be regarded as constant without significant loss of detail. Therefore, we do not associate the observed onset of a long-range magnetic order with oscillations in the temperature of the sample or changes in the applied field. Let us then consider an Arrhenius law model to investigate the observed time series of data.

A succinct introduction to phase transitions was given in section 1.3 using the Ginzburg-Landau phenomenological treatment [9, 38, 90–92] and a modified version of the Kosterlitz-Thouless model for 2D topological phase transitions [95–99], whilst the question of the (meta)-stability of magnetic skyrmions was considered as the result of a small energy gap between two states [86–89]. Notice, the time dependence of magnetic neutron scattering intensity has been used in the past to investigate the kinetics of skyrmion host materials, which is possible since magnetic neutron scattering measures the temporal and spatial spin-spin correlations (see equations 2.38 to 2.40) [311–313].

For our analysis, let us use a compressed exponential function (Kohlrausch-Williams-Watt or KWW) to determine the spin-dynamics relaxation lifetime, $\tau(T)$ – which depends on the temperature of the sample and manifests in the time dependence of the measured scattering intensity, $I(t)$. The compressed exponential function is given by [85, 303, 314–316]:

$$I(t) = A \exp \left(- \left[\frac{t}{\tau(T)} \right]^\beta \right) + C \quad (4.1)$$

Here, C represents the limit to which the neutron scattering intensity converges as time tends to $+\infty$, A is the change in intensity, and β is called the compressed exponent and arises from a superposition of exponential decays. Notice that the compressed exponential belongs to a family of semi-empirical functions that describe relaxation phenomena (*e.g.* skyrmions, dielectrics, polymers, and spin-spin systems) and include the Debye, non-Debye, Cole-Cole, Cole-Davidson, Havriliak-Negami functions among others [87, 315, 317–321]. In figure 4.9 panel

a), the solid black line shows the fitting results at $T = 55.6$ K.

This model holds at different temperatures. For instance, figure 4.10 shows the spectral time evolution at $T = 55.0$ K and $H = 20$ mT. We notice that upon miniature change in sample temperature, the spectral time-dependence measured at $T = 55.0$ K differs from the trend observed at $T = 55.6$ K. At $T = 55.0$ K, the intensity shows its minimum value at time zero, reaches a maximum value after a few minutes, and converges at a value below the maximum as time increases. The insets in panel a) show the scattering patterns at different times, in which we observe at first a weak diffuse ring and no well defined Bragg peaks. However, a six-fold pattern with twelve peaks sets in after a few minutes, in which six peaks exhibit a higher intensity than the other six peaks rotated 30 degrees with respect to the brighter ones. Moreover, as time progresses, the intensity of the six brighter peaks remains unchanged and drops for the less brighter six peaks. This time-series could depict a scenario with two spin relaxation processes: the development of a skyrmion lattice from an intermediate state formed by skyrmion domains, and a reorientation of two or more skyrmion structures rotated 30 degrees with respect to each other along a plane perpendicular to the incident neutron beam.

Furthermore, in panel b) of figure 4.10, we observe that the value of $|\vec{Q}|$ increases with the development of the skyrmion lattice, and slightly decreases as the skyrmion structures reorient themselves.

The time series collected at $T = 56.3$ K and $H = 20$ mT differs from the data at the two temperatures previously discussed. At $T = 56.3$ K, the intensity follows a two step process that starts with no evident Bragg reflections (see panel (a) in figure 4.11). Over time, a weak scattering ring develops, but at this temperature this process is much slower than in the two previous cases. Approximately after one hour, a set of twelve magnetic Bragg peaks with a six-fold symmetry arose, where six peaks were more intense and rotated 30 degrees with respect to the weaker peaks. Moreover, panel b) reveals a continuous growth in $|\vec{Q}|$ as time progresses, which is independent of the two steps observed in the scattering intensity. Thus, the time series at $T = 56.3$ K could be associated with a continuous nucleation of skyrmion domains that manifests through a scattering ring upon the formation

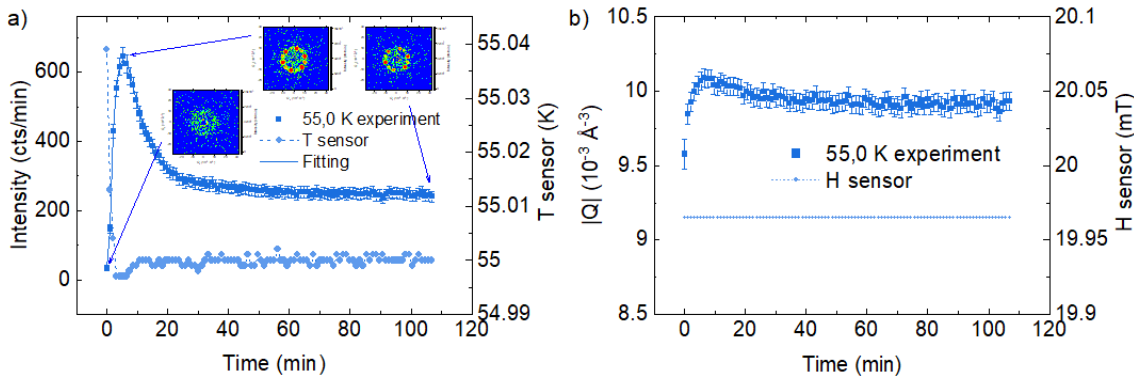


Figure 4.10: The SANS time evolution of $\langle 100 \rangle$ -orientated Cu_2OSeO_3 at $T = 55.0$ K and $H = 20$ mT reveals a) the evolution of the scattering intensity (dark blue squares) upon tiny changes in the temperature of the sample as measured a sensor in the cryostat (small light blue circles), and b) the scaling of the scattering vector (dark blue squares) and the effective applied field (small light blue circles). The continuous and dashed lines in a) show the curve fitting of the intensity and the trend of the temperature, respectively. The insets show selected spectra with the observed Bragg peaks as function of time.

of magnetic skyrmions disordered with respect to each other, and is followed by a reorientation of two or more domains in the sample.

From figures 4.9 to 4.11, we deduce that the temperature of the sample plays

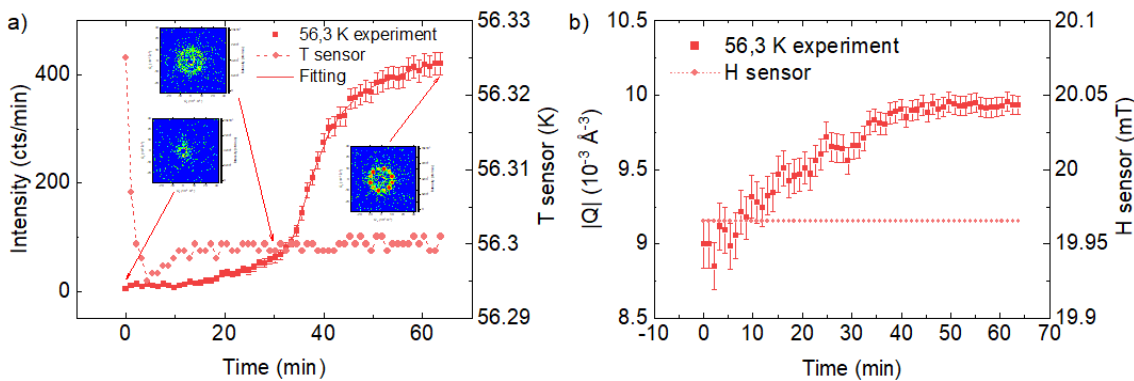


Figure 4.11: The SANS time evolution of a) the scattering intensity (dark red squares), its curve fitting (solid curve), and the sample temperature (light dark small circles and dashed line), and b) the magnitude of the scattering vector (dark red squares) and applied field (small light red circles) of Cu_2OSeO_3 orientated along $\langle 100 \rangle$ and measured at $T = 56.3$ K and $H = 20$ mT.

a role in determining the time scale of the formation of long-range magnetic skyrmion lattices. Given that the stability of the high-temperature skyrmion phase under investigation has been linked to temperature fluctuations in the literature [78, 80, 95, 228, 307, 311, 322, 323], we shall evaluate the spin relaxation temperature-dependence in the vicinity of the high-temperature skyrmion lattice state. Let us consider the variations in the scattering intensity as consequence of an energy gap, ΔE , that relates to the temperature, T , through the Arrhenius law expressed as [84, 86, 87, 324, 325]:

$$\tau(T) = \tau_0 \exp(-\Delta E/k_B T) \quad (4.2)$$

where τ_0 is the Arrhenius prefactor linked to fundamental fluctuation rates, and k_B is the Boltzmann constant. Our analysis uncovers three regimes in the inspected region of the phase diagram, around which the high-temperature skyrmion phase sets in: a two-steps relaxation process manifests at the lower limit of the skyrmion temperature range (blue shadowed region in figure 4.12). Around the centre of the skyrmion temperature range, a single step process occurs (no shadow). Just below T_C , another two-steps process starts with no Bragg peaks, and finishes with a high-T skyrmion state (red shadowed region).

The inverse-temperature dependence of the lifetime, τ , indicates that the single step process corresponds to an Arrhenius behaviour with a positive energy gap between the conical and skyrmion magnetic states, the lower-temperature region (highlighted in blue) follows a sub-Arrhenius behaviour that could be attributed to quantum mechanical tunnelling across an energy gap due to the influence of thermal fluctuations, and the higher-temperature region (highlighted in red) suggests a super-Arrhenius reaction such as the one observed in glass-forming liquids. A super-Arrhenius behaviour would match with the emergence of an intermediate hexatic phase dominated by topological defects between a topological and non-topological states of matter, as predicted by the Kosterlitz, Thouless, Halperin, Nelson and Young theory of 2D topological phase transitions [95–99].

In order to determine the field-dependence of the observed relaxation lifetime, different time series were collected at a constant temperature of $T = 56.1$ K between $H = 0$ mT and 20 mT, which maps the helical to skyrmion phase transition.

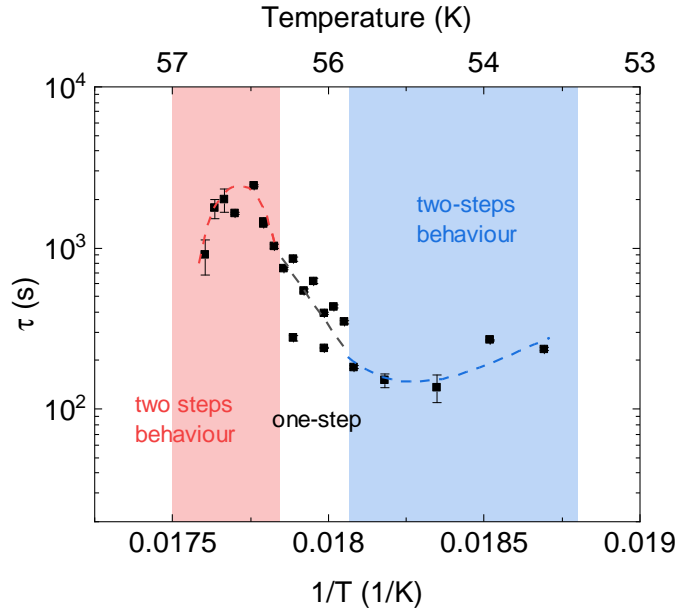


Figure 4.12: The temperature dependence of the Arrhenius prefactor measured upon ZFC/FH at $H = 20$ mT manifests in the scattering intensity lifetime as a function of temperature. The three regimes highlight the role of temperature in the conical-to-skyrmion phase transition as discussed in the main text.

Here, as the applied magnetic field is increased, the time series change from a purely helical scattering spectra, to a time-dependent superposition of the Bragg peaks characteristic of the helical and skyrmion phases, and time-dependent six-fold symmetric pattern typical of the skyrmion phase at higher fields. To quantify this field dependence, we fitted the scattering intensity for each curve using $\tau = \tau(H)$ into equation 4.1. The values of the lifetime of the magnetic relaxation, τ , are shown in figure 4.13.

Figure 4.13 unfolds an exponential regime of the field-dependence of the magnetic relaxation lifetime, τ , modelled by the Arrhenius law (see equation 4.2) in the magnetic field range of the high-temperature skyrmion phase, and a second regime in which τ is constant within the field region of the spin helical phase. These two regimes in the field-dependence of τ contrast with the three regimes found in its temperature-dependence, where the latter exhibits deviations from a simple Arrhenius law. This differences highlight the different roles of the temperature of the sample and the applied magnetic field in the stabilisation of the high-temperature magnetic skyrmion phase.

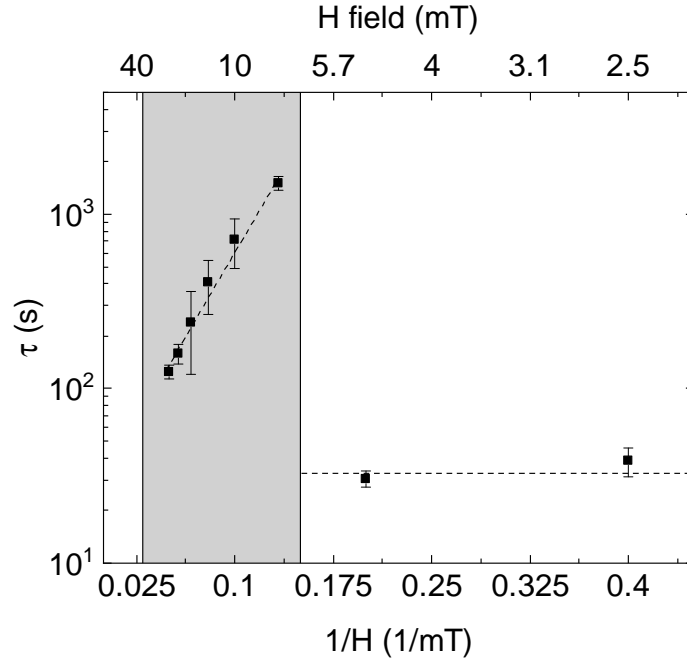


Figure 4.13: The magnetic field dependence of the scattering intensity relaxation lifetime measured upon ZFC/FH at $T = 56.1$ K follows two regimes that coincide with the spin-helical and skyrmion (grey shadow) phases, in which τ is given by a constant and an field-dependent exponential, respectively. The dashed lines are guides to the eye.

Previous investigations have provided further insight into the stabilisation of the skyrmion lattices of Cu_2OSeO_3 . Hicken *et al.* reported collective skyrmion excitations in single crystal Cu_2OSeO_3 using muon spin relaxation, in which the relaxation rate exhibits power-law behaviour above T_C [323]. However, they observed deviations from a power law below this transition, and associated these skyrmion dynamics to the creation and annihilation of skyrmions. Makino *et al.* found evidence of an energy gap between two different skyrmion states in single crystal Cu_2OSeO_3 using small angle neutron scattering [311]. Here, two skyrmion lattices were observed rotated 30 degrees with respect to each other, and their emergence depended on different thermal protocols akin the irreversibility of spin glasses. On the other hand, Crisanti *et al.* used space-resolved SANS on Cu_2OSeO_3 single crystals and discovered evidence of a position-dependence of the stability of the skyrmion state that induces different lifetimes across the sample [307]. The effect of the geometry of the sample on the extension/reduction of

the skyrmion lifetime is supported by the Small Angle X-ray Scattering (SAXS) investigation in thin slabs of Cu_2OSeO_3 performed by Wilson *et al.*, which revealed an extended skyrmion region in the T-H phase diagram along both [100] and [110] crystallographic directions. Furthermore, Lorentz TEM and magnetic susceptibility measurements have been used to demonstrate the role of topological defects along the skyrmion to paramagnetic phase transition as predicted by Janson *et al.*, Mohanta *et al.*, and the Kosterlitz-Thouless theory [95, 314, 326, 327]. These precedents support our deductions since they suggest the existence of collective skyrmion excitations across different time scales as consequence of an energy gap between different magnetic states, which depends on the temperature, thermal history and geometry of the sample, and arise as consequence of the quantum creation and annihilation of individual skyrmions through half-skyrmions and other topological spin arrangements. Nonetheless, we acknowledge the necessity of confirming whether the temperature measured by the sensor inside the cryostat reflects the real temperature of the sample in our setup, or if a thermal gradient exists between the sample and the sensor since that could impact the interpretation of our data. Hence, we plan to address this question in the upcoming months in collaboration with the scientists at ANSTO.

4.4 Conclusions

Our investigations of the stability of the high-temperature magnetic skyrmion state of Cu_2OSeO_3 has revealed relaxation processes that affect the intensity and scattering vector of the observed magnetic Bragg reflections as a function of the applied magnetic field and the temperature of the sample. The field dependence of the observed relaxation unveils two regimes of the relaxation lifetime: a constant lifetime was found in the magnetic field range or the spin-helical phase, while in the field range of the high-temperature skyrmion lattice, the lifetime follows an exponential decay as function of inverse field akin the Arrhenius law. Moreover, the temperature dependence of the relaxation lifetime follows three regimes characterised by a lower-temperature sub-Arrhenius behaviour attributed to quantum tunnelling across an energy gap, an Arrhenius regime in the

temperature range of the centre of the high-temperature skyrmion phase, and a super-Arrhenius behaviour at slightly higher temperatures as it has been observed in glass-forming liquids. Hence, we associate the field- and temperature-dependence of the relaxation lifetime with a predominant role of thermal fluctuations in the creation and annihilation of individual topological textures and their collective kinetics.

Additionally, we unearthed evidence of the effects of illuminating the sample with light in the visible region of the spectrum across the helical, low- and high-temperature skyrmion phases. The three magnetic phases investigated react differently to light stimuli. Here, the scattering intensity and scattering vector observed in the low-temperature skyrmion state remain approximately unaffected, the helical phase shows a linear wavelength dependent response in both observables, and the high-temperature skyrmion state exhibits a non-linear wavelength dependence. Furthermore, an irreversible optical-power behaviour was observed using violet and near infrared light. Therefore, we conclude that external light stimuli may manipulate the long-range magnetic order of Cu_2OSeO_3 akin the photomagnetic effect observed in other skyrmion materials and in Cu_2OSeO_3 using high-frequency laser pulses. Nonetheless, it is still unclear the degree in which the light-induced effects overlap with optical heating of the sample, and this question shall be addressed in the following experiments.

Finally, we observed that the field and temperature range in which the high-temperature skyrmion phase emerges seems to grow upon increasing tellurium concentrations. However, the effective level of tellurium doping remains to be confirmed, and it would be desirable to confirm these observations along preferential symmetry axes, which may also reveal the doping effects on the low-temperature skyrmion phase.

Raman scattering in Cu_2OSeO_3

In this chapter, we report the results of our Raman measurements performed on a series of randomly orientated tellurium-doped Cu_2OSeO_3 single crystals at different temperatures at zero magnetic field. The Raman spectra from these randomly orientated samples unveil some interesting details of the influence of applying chemical pressure through atomic substitution on the atomic and magnetic vibrations in the multiferroic skyrmion host Cu_2OSeO_3 . Finally, a few ideas for future experiments will be presented.

5.1 Precedents

Raman light scattering is a unique experimental technique since it offers detailed insights in the lattice dynamics and fundamental excitations such as magnons. While inelastic neutron scattering allows for the determination of the spin wave dispersion throughout the entire Brillouin zone, Raman light scattering can measure the two magnon density of states, but with a significantly higher energy resolution. First temperature dependent Raman light scattering experiments on pristine Cu_2OSeO_3 single crystals were performed by Gnezdilov *et al.*, who only investigated the helical and paramagnetic phases without an externally applied

magnetic field [328]. Their article reports Raman scattering on Cu_2OSeO_3 single crystals in a pseudo-backscattering geometry, using parallel- (XX) and cross- (XY) polarised green lasers ($\lambda = 514.5 \text{ nm}$ and $\lambda = 532.1 \text{ nm}$) to investigate the spectrum of Cu_2OSeO_3 orientated with the incident laser beam parallel to the $\langle 111 \rangle$ crystallographic axis upon no applied magnetic fields. They provide evidence of 53 phonons below 850 cm^{-1} in the paramagnetic phase, 56 peaks in the helical phase and 58 below $T^* = 20 \text{ K}$ (see figure 5.1), where T^* is the temperature at which the magnetic contribution to the dielectric constant changes sign [72]. Considering the 56 atoms in the unit cell, they predict a total of 168 phonon modes, of which 3 are acoustic and 84 are Raman active normal modes ($14A+14E_1+14E_2+42T$) of lattice oscillations in the paramagnetic state. Additionally, they predict 15 Raman active magnetic excitations in the helical phase. In addition, two-phonon and possibly two-magnon modes are present in the energy range between 850 and 2000 cm^{-1} . Furthermore, the excitation that emerge upon cooling below the paramagnetic phase transition temperature and below T^* were regarded by the authors as magnetic excitations. Moreover, Gnezdilov, *et al.* report the temperature dependence of the phonons lineshape that exhibits a set of anomalies associated by the authors with a strong spin-orbit coupling, which induces a strong Dzyaloshinskii-Moriya interaction.

Additionally, a sharp increase in the Raman intensity below $T_C = 58 \text{ K}$ has been reported for most phonon peaks. Since there is no structural phase transition known below the magnetic transition temperature, the authors associate this phenomenon to a jump in the dielectric constant in the magnetically ordered phase driven by a linear magnetoelectric effect.

An alternative spin cluster model of the magnetic excitations of Cu_2OSeO_3 was developed in the doctoral dissertation of Rolf Versteeg [329]. Here, six Raman active magnetic excitations in the spin helical phase were predicted and attributed to single-magnon (Elliot Loudon) modes, and one of the magnetic excitations was attributed to a two-magnon Raman mode [330]. However, only four magnetic excitations were experimentally observed in their data at $263, 273, 300$ and 425 cm^{-1} below the PM phase transition temperature upon no applied magnetic field – not including the 86 and 204 cm^{-1} magnetic modes reported in reference [328].

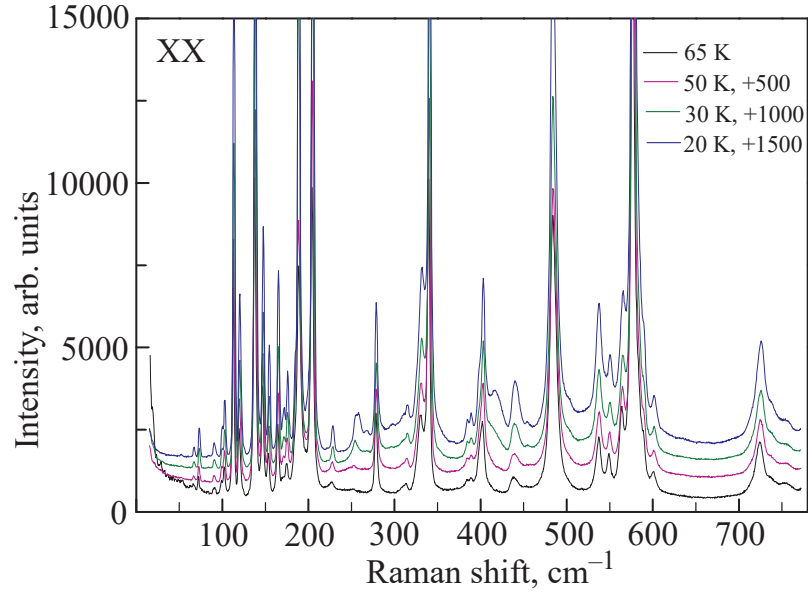


Figure 5.1: The temperature dependence of the Raman response of Cu_2OSeO_3 shows three additional peaks appear centred around 261 , 270 and 420 cm^{-1} below the paramagnetic transition temperature, $T_C \approx 58 \text{ K}$ (image taken from [328]).

Furthermore, time-resolved Raman scattering measurements of the magnetic excitations of the helical phase of Cu_2OSeO_3 single crystals have focused on the 260 cm^{-1} magnon branch [331]. Versteeg *et al.* studied the time-dependent behaviour of this Raman active magnetic excitation and found evidence of spin-light interactions in the helical magnetic order upon photo-excitation of this multiferroic material using pulses of monochromatic light at $\lambda = 570 \text{ nm}$ during 0.3 picoseconds. As a result of these excitations, the intensity of the magnon centred at $\sim 260 \text{ cm}^{-1}$ is temporarily quenched and builds up after $\sim 200 \text{ ps}$. The researchers associated this observation with a melting of the long-range magnetic order. However, Versteeg *et al.* did not report the ultra-fast time-dependent behaviour of the other magnons in the pico-second scale. Thus, they cannot rule out that the observed time-dependence of the 260 cm^{-1} magnon branch could point at the stimulation of further magnetic excitations that results in a momentary suppression of the 260 cm^{-1} feature. Hence, further investigations are required.

Inelastic Neutron Scattering (INS) experiments have been performed to identify magnetic excitations and their dispersion relation in the helical phase of Cu_2OSeO_3 [332, 333]. These studies used different models to determine the magnetic coupling constants of Cu_2OSeO_3 , namely, a coarse-grained approach

to the low-energy spin dynamics of Cu_2OSeO_3 published by Luo *et al.*, and a microscopic model of entangled copper tetrahedra by Portnichenko *et al.* [332–335]. Noticeably, no Raman- or inelastic neutron scattering studies of the skyrmion phase of Cu_2OSeO_3 have been published, to the best of our knowledge. Additional investigations of the Raman- and INS-spectra of Cu_2OSeO_3 across the low- and high-temperature skyrmion phases could provide further insight of the spin dynamics of this multiferroic.

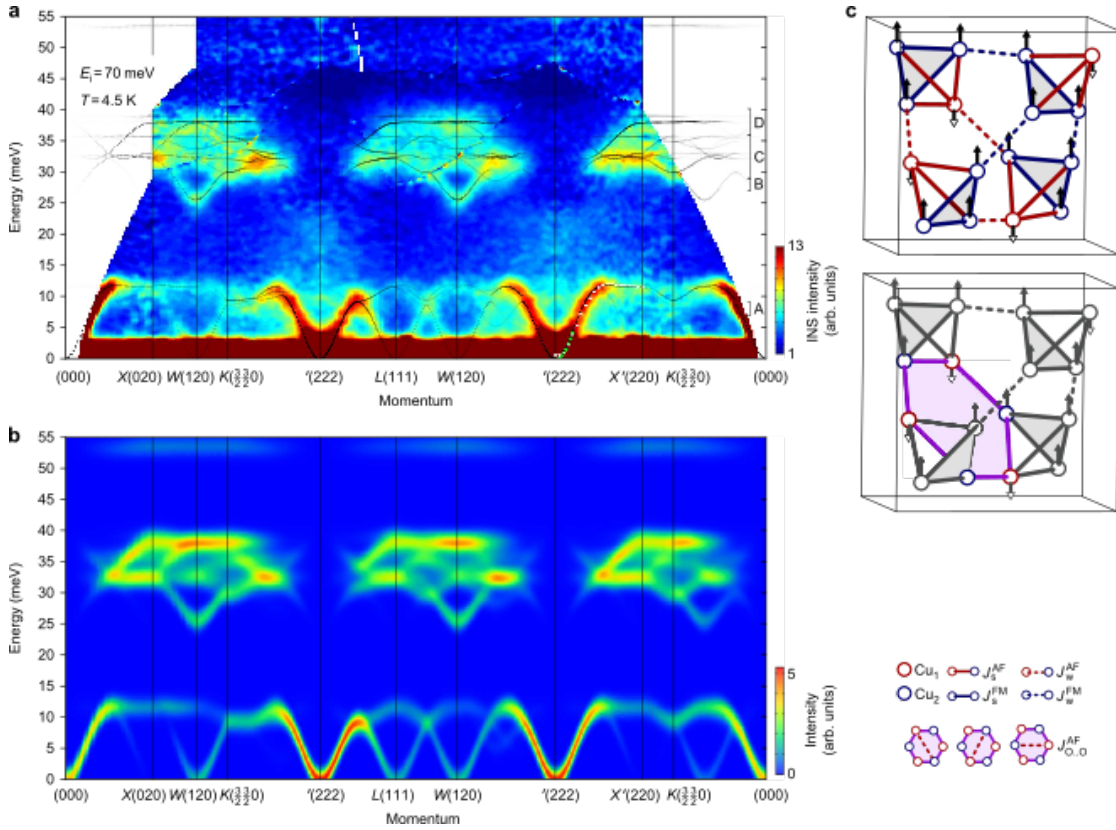


Figure 5.2: a) Dispersion relation of the magnetic excitations of Cu_2OSeO_3 in the helical phase measured using time of flight neutron spectroscopy, b) theoretical magnetic dispersion relation from spin-dynamical calculations, and c) illustration of the magnetic exchange paths of Cu_2OSeO_3 : on top the FM (solid blue) and AFM (solid red) couplings with dashed lines indicating weaker couplings, and below the $J_{O..O}^{AFM}$ interaction between further neighbours, *i.e.* among every second Cu₁ and Cu₂ atomic sites (image taken from [333]).

Figure 5.2 shows the agreement between the a) experimental and b) theoretical dispersion relation of the magnetic excitations of Cu_2OSeO_3 . This agreement enabled Portnichenko *et al.* to determine the strengths and symmetries of the

ferromagnetic and antiferromagnetic interactions between nearest and second-nearest neighbour copper atoms, as well as the weaker $J_{O..O}^{AFM}$ interaction of the further neighbours. The dispersion relations and the magnetic coupling values of Cu_2OSeO_3 may be used to determine the energy of the magnetic excitations observed via Raman scattering, for example, via the broken-bond model or micro-magnetic simulations.

5.2 Experimental results and discussion

We performed Raman scattering measurements on a series of four randomly orientated $\text{Cu}_2\text{OSe}_{1-x}\text{Te}_x\text{O}_3$ single crystals with nominal tellurium contents of $x = 0.00, 0.10, 0.30$ and 0.50 upon Zero Field Cooling/ Zero Field Heating in order to investigate the temperature- and tellurium-content-dependencies of the lattice and magnetic excitations across the spin helical and paramagnetic states of the samples at zero magnetic field (see the description of the experimental setup in section 2.5). Unless explicitly stated, all the Raman spectra shown and discussed in this chapter have been accumulated utilising unpolarised laser illumination of 10 mW at the sample position (in order to avoid sample heating) and their intensities have been corrected for detailed balance given by $1 + n(\omega)$, where $n(\omega)$ represents the Bose distribution function (see section 2.4) [210, 336].

As a first step in our Raman spectra investigation, we measured the Raman spectra of randomly orientated single crystals of $\text{Cu}_2\text{OSe}_{1-x}\text{Te}_x\text{O}_3$ with different doping levels at a constant temperature of $T = 85$ K, which was chosen because this temperature is slightly above the magnetic transition temperature, yet the intensity of the phonon modes is strongly increased as compared to the Raman spectrum taken at room temperature (see Raman data shown above from [328]).

Figure 5.3 highlights three selected phonon peaks that shift towards lower energies upon increasing tellurium concentrations at constant temperature. Here, we notice that the effect of tellurium doping in the energies of the selected peaks is within a few cm^{-1} . If we assume that the phonon centred at 218 cm^{-1} corresponds to a vibration of selenium atoms, then the effective tellurium content can be calculated. Notice that although infrared active phonon modes with energies

Nominal Te-content	x_{eff} calculated at 85 K (%)	x_{eff} calculated at 300 K (%)
0.00	0.00	0.00
0.05	–	1.0 ± 0.2
0.10	3.0 ± 0.6	4.1 ± 0.6
0.15	–	4.7 ± 0.5
0.20	–	5.2 ± 0.5
0.30	3.7 ± 0.5	–
0.50	4.5 ± 0.6	–

Table 5.1: Effective tellurium content of the $\text{Cu}_2\text{OSe}_{1-x}\text{Te}_x\text{O}_3$ single crystals calculated using the Raman scattering spectrum measured at $T = 85$ K and 300 K, and a first order approximation to the effects of atomic substitution in the energy of the phonon modes through changes in the reduced mass of the vibrating lattice (see discussion in the main text).

of 213.6, 557.4, and 830.7 cm^{-1} have been associated with the vibration of selenium atoms, a complex motion of oxygen atoms, and a radial breathing of the SeO_3 units, respectively (see tables 1 and 2 in [337]), the reduced mass of complex phonon modes such as the 588 cm^{-1} and 853.5 cm^{-1} modes involves several atoms and must be calculated according to their eigenvectors, *i.e.*, considering their relative displacements. In a first approximation, the frequency of a phonon is proportional to $\sqrt{1/m}$. Using such an approximation, we get the effective tellurium content values shown in table 5.1. These effective tellurium contents are in agreement with the assumption made in chapter 4.2 that only a fraction of the tellurium atoms are replacing the selenium atoms. Our EDX data gave a rough estimate that just 10 % of the Te-atoms are in the final crystal [76]. Therefore, Raman light scattering did provide a further, more accurate and contact free method to determine the effective Te-content in the $\text{Cu}_2\text{OSe}_{1-x}\text{Te}_x\text{O}_3$ crystals.

Let us discuss a series of measurements of the spectra Raman collected in the Raman shift range between 59 and 904 cm^{-1} and sample temperatures above 12 K and room temperature. Figure 5.4 shows the Raman spectrum at selected temperatures of the pristine Cu_2OSeO_3 single crystal. Here, a total of 87 Raman active modes were identified through peak fittings of the spectrum at $T = 12$ K

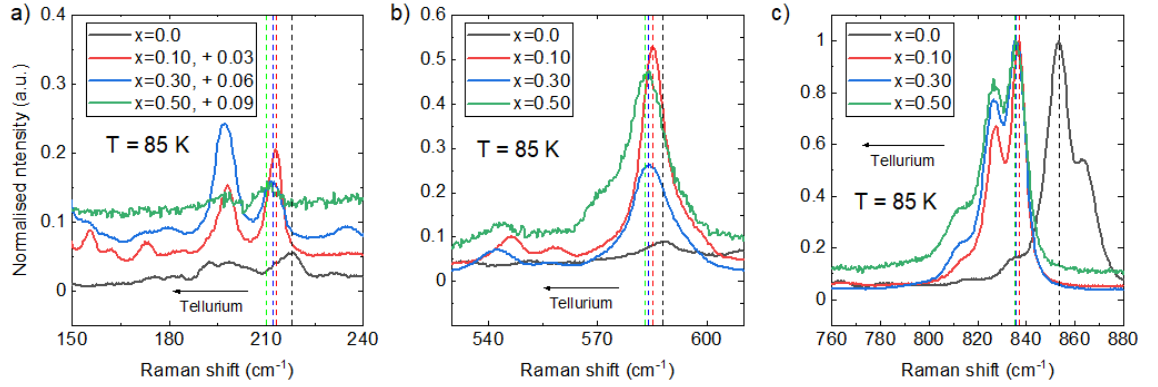


Figure 5.3: Raman scattering of selected doping levels of $\text{Cu}_2\text{OSe}_{1-x}\text{Te}_x\text{O}_3$ single crystals at a constant temperature of 85 K. In all three panels, we notice a subtle shift of selected phonon peaks towards lower energies as highlighted with vertical dashed lines across the centre of the peaks with an energy of a) 218 cm^{-1} , b) 588 cm^{-1} , and c) 853.5 cm^{-1} in the pristine sample.

centred at Raman shifts of 62.3, 66.8, 74.3, 78.6, 86.8*, 89.3, 94.9, 99.6, 103.0, 107.0, 110.7, 114.3, 117.7, 121.5, 127.3, 129.6, 135.0, 138.1, 142.3, 149.4, 155.3, 159.0*, 163.2, 169.3, 174.6, 178.12, 182.3, 188.5, 191.6, 195.4, 198.4, 204.5*, 212.9, 215.8, 218.7, 223.0, 231.4, 238.5, 259.2*, 265.6*, 274.8*, 279.2, 291.1, 297.1*, 316.0, 323.9, 328.8, 336.1, 345.5, 374.2, 375.0, 387.4, 392.5, 401.3, 401.7, 413.1, 428.5*, 447.2, 448.7, 457.1, 466.0, 480.8, 493.5, 508.8, 534.3, 551.0, 573.0, 587.9, 606.0, 613.0, 630.7, 658.2, 666.9, 722.5, 733.5, 744.0, 763.3, 781.1, 787.0, 797.8, 818.6, 835.9, 848.0, 853.7, 863.8, and 870.0 cm^{-1} .

Our discussion of the observed features will focus on a reduced number of dominant excitations. Before we discuss the temperature evolution of the scattering spectrum of two selected phonon modes (centred at 291.1, and 587.9 cm^{-1}) and one magnetic excitation (centred at 428.4 cm^{-1}) for the three different tellurium-doping levels under investigation, let us introduce the spectra of the other samples as function of temperature.

Figure 5.5 shows the temperature dependent Raman spectrum acquired from a single crystal of 5 % tellurium-doped Cu_2OSeO_3 . A total of 60 Raman active modes were identified at base temperature using curve fittings, which are centred around: 60.3, 68.0, 74.2, 80.8, 97.8, 107.9, 110.4, 121.3, 126.9, 128.7, 146.1,

*Previously identified as a magnon mode in the literature [328, 331]

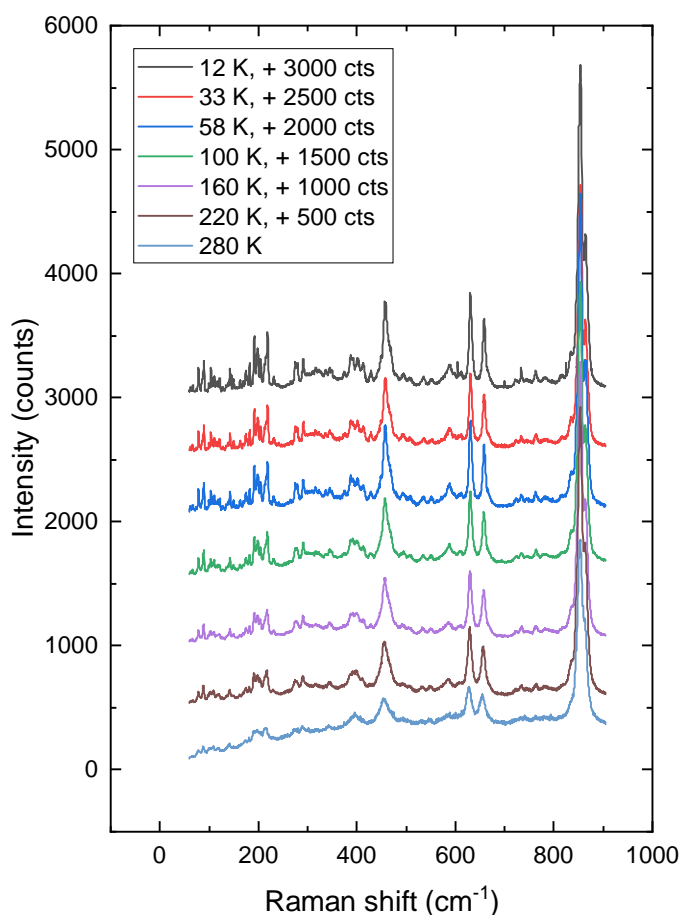


Figure 5.4: Raman spectrum from pristine Cu_2OSeO_3 were measured using a laser line of $\lambda = 514.32$ nm at selected temperatures. A total of 86 excitations were clearly identified (see main text).

155.4, 162.5, 173.0, 179.8, 184.2, 192.5, 197.0, 199.4, 207.5, 209.9, 213.0, 215.1, 219.3, 233.0, 236.7, 243.7, 250.4, 262.0, 268.7, 277.8, 287.3, 304.0, 319.3, 324.2, 342.0, 349.6, 361.0, 386.0, 397.9, 406.5, 411.9, 429.9, 449.5, 463.0, 491.0, 493.5, 509.9, 546.3, 559.7, 580.0, 586.2, 595.0, 611.0, 620.0, 725.0, 735.1, 746.7, 763.2, 820.0, 827.7, 837.6, and 860.0 cm^{-1} . Notice that the lineshapes of the observed excitations at base temperature do not always follow well-defined peaks, and a broad background appears at 411.9 cm^{-1} . Moreover, the number of observed peaks differs from those observed in the pristine sample, which may be consequence of the random sample alignment used according to symmetry selection rules.

Figure 5.6 shows the temperature dependent Raman spectrum acquired from a single crystal of 10 % tellurium-doped Cu_2OSeO_3 . A total of 66 Raman active modes were identified at base temperature using curve fittings, which are cen-

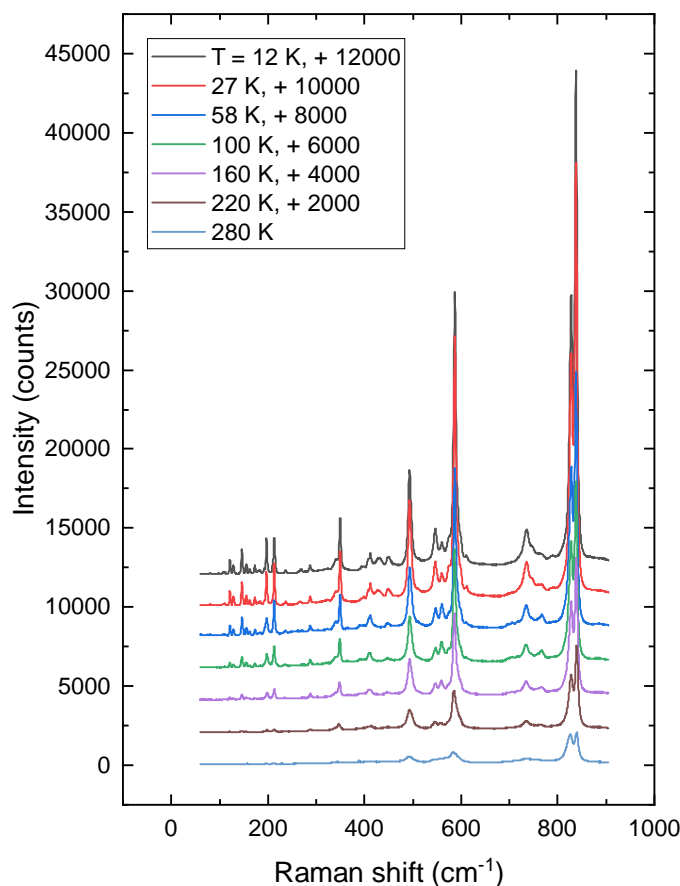


Figure 5.5: Raman spectrum from 5 % Te-doped Cu_2OSeO_3 were measured using a laser line of $\lambda = 514.32 \text{ nm}$ at selected temperatures. A total of 60 excitations were clearly identified (see main text).

tred around: 59.4, 66.5, 73.6, 80.1, 90.7, 97.4, 107.6, 109.9, 118.0, 120.8, 127.3, 129.3, 130.0, 145.4, 145.7, 154.6, 161.8, 171.9, 178.8, 183.4, 191.7, 196.1, 197.9, 207.0, 209.5, 212.4, 214.4, 217.0, 232.3, 236.0, 251.5, 261.0, 267.0, 275.9, 286.0, 300.1, 314.9, 322.0, 340.0, 348.2, 363.0, 395.0, 405.3, 411.0, 425.5, 448.1, 464.0, 482.0, 491.8, 506.0, 522.3, 544.9, 558.3, 573.0, 585.3, 592.0, 609.0, 625.2, 730.0, 734.3, 748.0, 763.0, 791.0, 818.6, 826.7, and 836.4 cm^{-1} . As in the case of the spectra from the 5 % tellurium-doped sample, the number of Raman peaks from the 10 % tellurium-doped sample differs from the number of excitations identified in the pristine and 5 % sample, which highlights once more the importance of measuring the Raman spectra from samples orientated along a well known crystallographic axis in order to be able to determine the effect of the Raman symmetry selection rules on the data.

After inspecting the spectra from the three samples, we notice that a number of excitations only appear below the paramagnetic transition temperature. In par-

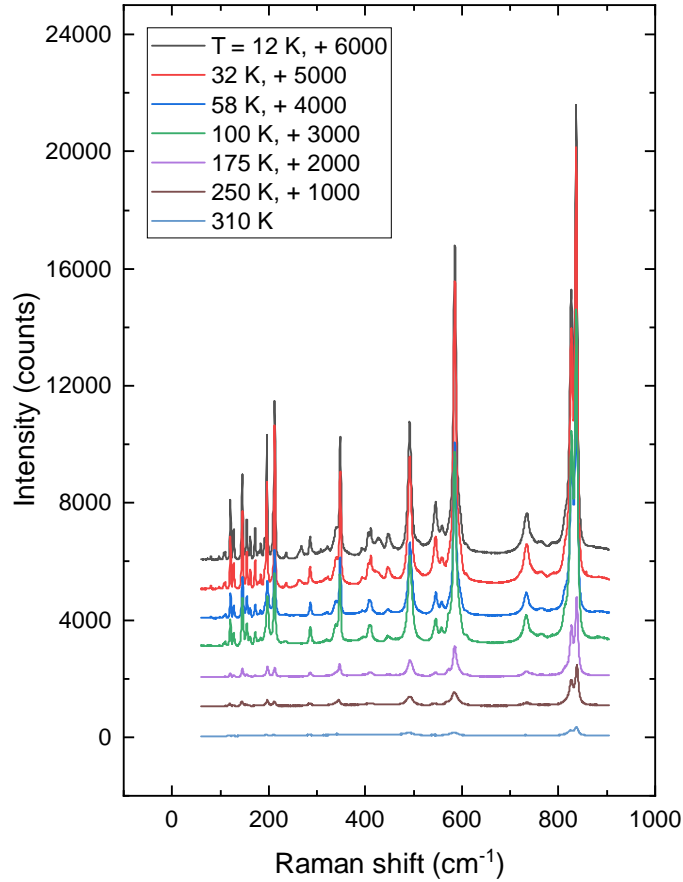


Figure 5.6: Raman spectrum from 10 % Te-doped Cu_2OSeO_3 were measured using a laser line of $\lambda = 514.32 \text{ nm}$ at selected temperatures. A total of 66 excitations were clearly identified (see main text).

ticular, the magnetic excitation centred around $428.4 \text{ cm}^{-1} \approx 53 \text{ meV}$ in pristine Cu_2OSeO_3 dominates the surrounding region of the spectra, and remains visible in the atomically substituted samples (centred at 430.3 and 428.0 cm^{-1} in the $x = 0.05$, and 0.10 samples, respectively). In his PhD thesis, Rolf B. Versteeg has associated this Raman peak with a 1-magnon mode using the Elliot-Loudon formalism (see table 5.3 and figure 8.2 [329]). Nonetheless, the energy of this magnetic excitation suggests that it could also be associated to a two-magnon mode, which would have an energy close to the weak signal at 53 meV measured and predicted by Portnichenko *et al.*, and to the sum of the maximum energies of the 12 meV acoustic- and the 38 meV optical- magnon branches shown in figure 5.2 [333, 334].

Figure 5.7 shows the temperature dependence of a) the scattering intensity, b) the energy of the centre of the peak, and c) the full width at half maximum from

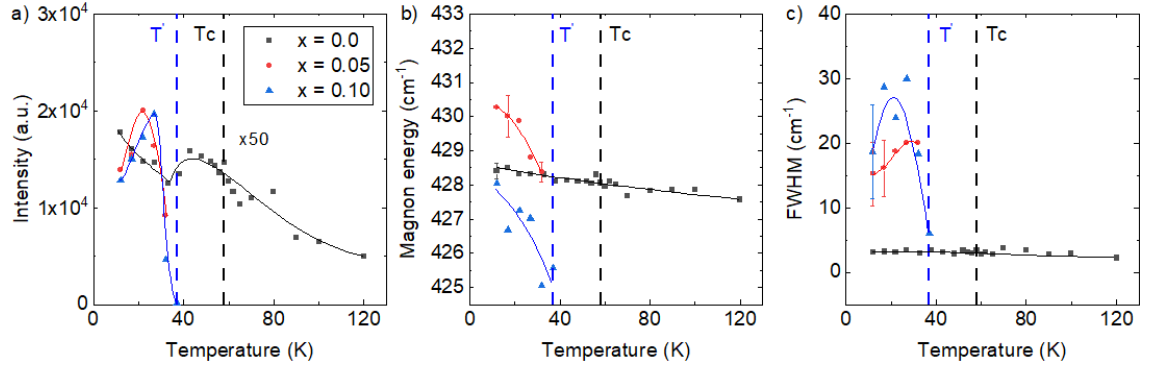


Figure 5.7: Temperature dependence of the a) scattering intensity, b) magnon energy, and c) linewidth of the 428.4 cm^{-1} magnon line in Te-doped Cu_2OSeO_3 . The solid lines are guides to the eye, and the dashed vertical lines show the PM phase transition temperature, $T_C = 58 \text{ K}$, and the temperature, T' , at which the observed magnon mode disappears in the Te-doped samples.

Lorentzian curve fittings of the temperature dependent data from the three selected tellurium doped samples. Here, we observe from the excitation prevails above the magnetic phase transition temperature, T_C , in the pristine sample. However, the excitation disappears at a lower temperature that we will refer to as $T' \approx 38 \text{ K}$, in the tellurium-doped samples. The emergence of magnetic excitations below T' in the tellurium-doped samples resembles the behaviour reported by Gnezdilov *et al.* in their Raman study, which was associated with changes in the dielectric constant magnetic contributions. Hence, the observed behaviour may suggest that atomic substitution could have an effect in the dielectric constant of Cu_2OSeO_3 . However, this has not been investigated yet, to the best of our knowledge.

Let us now focus in the dominant phonon mode centred around 291.1 cm^{-1} in pristine Cu_2OSeO_3 . This Raman peak has been associated with an internal in-plane vibration of CuO_5 units (see chapter 8 in the PhD thesis of Rolf B. Versteeg [329]). Figure 5.8 shows the temperature dependence of the Lorentzian curve fitting parameters from the selected samples. In panel a) we observe that additional contributions to the scattering intensity appear above T' and $T_C = 58 \text{ K}$ in the 5 % Te-doped sample and above T_C in the 10 % Te-doped sample, which exhibits anomalies in its temperature dependent Raman scattering intensity. Moreover, in panel b) we observe that energy of the centre of the peak exhibits deviations

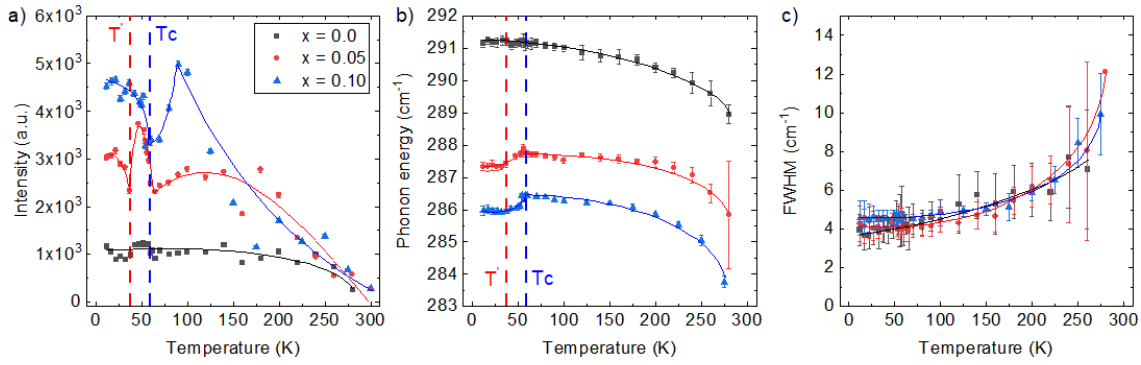


Figure 5.8: Temperature dependence of the a) scattering intensity, b) phonon energy, and c) linewidth of the 291.1 cm^{-1} phonon line in Te-doped Cu_2OSeO_3 . The solid lines are guides to the eye, and the dashed vertical lines show the PM phase transition temperature, $T_C = 58 \text{ K}$, and the temperature, $T' \approx 38 \text{ K}$, at which the 428.4 cm^{-1} magnon mode disappears in the Te-doped samples.

from a smooth anharmonic decay model (see figure 2.11) around both T' and T_C in the Te-doped samples investigated, whilst the FWHM in panel c) shows no deviations from the expected broadening of the Raman modes upon heating. Notice that this phonon mode shows a small energy shift below T_C in the undoped, while the same phonon mode exhibits pronounced phonon renormalizations below T_C in the tellurium doped samples. These observations suggest that the application of chemical pressure through atomic substitution may also have an effect in the behaviour of the lattice vibrations of Cu_2OSeO_3 , which may be related to a greater overlap of the electronic orbitals between copper ions and their subsequent influence on the magnitude of the magnon-phonon interactions. However, this remains unsolved. Let us briefly discuss the temperature dependence of the 588 cm^{-1} phonon line, which has been associated with the motion of oxygen atoms of Cu_2OSeO_3 whose eigenvector remains unsolved in the literature (see chapter 8 in the PhD thesis of Rolf B. Versteeg [329]).

Figure 5.9 shows a) that the intensity of the 588 cm^{-1} phonon displays a step increase for below T_C , as in the case of the 291 cm^{-1} phonon mode. Particularly below T' and $T_C = 58 \text{ K}$ for the $x = 0.05$ and 0.10 samples, respectively. Panel b) shows that the temperature dependence of the of the 588 cm^{-1} phonon energy differs from the anharmonic decay model with deviations arising above T' and T_C , in particular in the Te-doped samples. Moreover, panel c) shows that

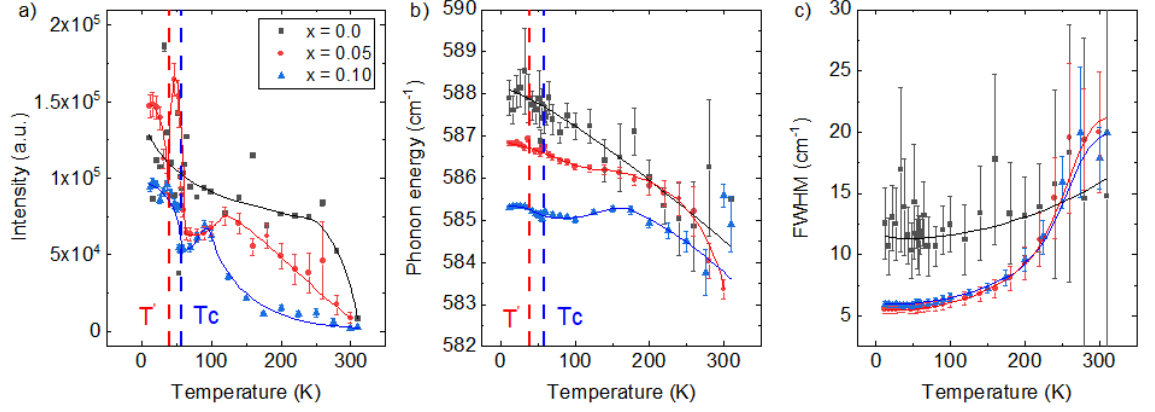


Figure 5.9: Temperature dependence of the a) scattering intensity, b) phonon energy, and c) linewidth of the 587.9 cm^{-1} phonon line in Te-doped Cu_2OSeO_3 . The solid lines are guides to the eye, and the dashed vertical lines show the PM phase transition temperature, $T_C = 58 \text{ K}$, and the temperature, T' , at which the 428.4 cm^{-1} magnon mode disappears in the Te-doped samples.

the width of the 588 cm^{-1} phonon line broadens following different patterns in the pristine and Te-doped samples, with the doped samples starting sharper at base temperature and broadening quicker than in the pristine sample. The observed temperature dependence suggests that additional contributions to the phonon decay may arise as a consequence of non-magnetic atomic substitutions in Cu_2OSeO_3 , due to changes in the dielectric constant of Cu_2OSeO_3 or caused by enhanced spin-phonon interactions (see for example [336]).

5.3 Conclusions

The emergence of magnetic excitations with an approximate energy of $428 \text{ cm}^{-1} \approx 53 \text{ meV}$ upon cooling the tellurium-doped samples below T' is a reminiscence of Gnezdilov *et al.*, and may indicate changes in the dielectric constant magnetic contributions upon increasing tellurium content. Moreover, the temperature dependence of the 291 and 588 cm^{-1} phonon modes suggest that additional contributions to the phonon decay may arise as a consequence of non-magnetic atomic substitutions in Cu_2OSeO_3 , due to changes in the dielectric constant of Cu_2OSeO_3 or caused by enhanced spin-phonon interactions as a consequence of applied chemical pressure through tellurium doping.

5.4 Perspective of future experiments

Our results on randomly orientated $\text{Cu}_2\text{OSe}_{1-x}\text{Te}_x\text{O}_3$ single crystals suggest that a systematic scrutiny of the Raman-active phonon and magnon selection rules along a well defined sample alignment of all samples is needed to guarantee that the data are comparable in number of Raman-active phonon modes and their corresponding scattering intensity. Therefore, it would be advisable to conduct measurements of the temperature dependence of the tellurium-doped samples along the $\langle 100 \rangle$ using the Raman setup at UNSW. Additionally, it would be interesting to investigate the magnetic excitations within the skyrmion phases of $\text{Cu}_2\text{OSe}_{1-x}\text{Te}_x\text{O}_3$ single crystals using Raman scattering, which has not been performed yet to the best of our knowledge, and could be performed upon FC/FH with the Raman setup and sample environment at the School of Physics at UNSW. Furthermore, external pressure could be applied to the tellurium-doped series of Cu_2OSeO_3 single crystals as a third experimental parameter using the Diamond Anvil Pressure cells for Raman scattering with a pressure range of up to 70 GPa and a temperature range from 1.7 to 300 K available in the research group of C. Ulrich at UNSW, which could provide additional information to the reports of a potential skyrmion phase transition upon applied pressure at room temperature [338]. Finally, a theoretical framework is needed to discern the influence of tellurium doping in the energy shift observed in the lattice vibrations and the unconventional temperature dependence of the magnetic excitations of the selected samples.

Bibliography

1. Skyrme, T. H. R. A unified field theory of mesons and baryons. *Nuclear Physics* **31**, 556–569 (1962).
2. Tokura, Y. & Kanazawa, N. Magnetic Skyrmion Materials. *Chemical Reviews* **121**, 2857–2897 (2021).
3. Das, S. *et al.* Observation of room-temperature polar skyrmions. *Nature* **568**, 368–372 (2019).
4. Flores-Alfonso, D. & Quevedo, H. Extended thermodynamics of self-gravitating skyrmions. *Classical and Quantum Gravity* **36**, 154001 (2019).
5. Seki, S., Yu, X. Z., Ishiwata, S. & Tokura, Y. Observation of Skyrmions in a Multiferroic Material. *Science* **336**, 198–201 (2012).
6. Nagaosa, N. & Tokura, Y. Topological properties and dynamics of magnetic skyrmions. *Nature Nanotechnology* **8**, 899–911 (2013).
7. Seki, S. & Mochizuki, M. Skyrmions in Magnetic Materials (Springer International Publishing, 2016).
8. Pfleiderer, C. Magnetismus mit Drehsinn. *Physik Journal* **9**, 25–30 (2010).
9. Muhlbauer, S. *et al.* Skyrmion Lattice in a Chiral Magnet. *Science* **323**, 915–919 (2009).
10. Seki, S. *et al.* Formation and rotation of skyrmion crystal in the chiral-lattice insulator Cu_2OSeO_3 . *Physical Review B* **85**, 220406(R) (2012).

11. Koshibae, W. & Nagaosa, N. Theory of current-driven skyrmions in disordered magnets. *Scientific Reports* **8**, 6328 (2018).
12. Seki, S. *et al.* Direct visualization of the 3D shape of skyrmion strings in a noncentrosymmetric magnet. *Nature Materials* (2021).
13. Tonomura, A. *et al.* Real-space observation of skyrmion lattice in helimagnet MnSi thin samples. *Nano Letters* **12**, 1673–1677 (2012).
14. Münzer, W. *et al.* Skyrmion lattice in the doped semiconductor $\text{Fe}_{1-x}\text{Co}_x\text{Si}$. *Physical Review B* **81**, 041203 (2010).
15. Yu, X. Z. *et al.* Real-space observation of a two-dimensional skyrmion crystal. *Nature* **465**, 901–904 (2010).
16. Kanazawa, N. *et al.* Large topological Hall effect in a short-period helimagnet MnGe. *Physical Review Letters* **106**, 156603 (2011).
17. Yu, X. Z. *et al.* Near room-temperature formation of a skyrmion crystal in thin-films of the helimagnet FeGe. *Nature Materials* **10**, 106–109 (2010).
18. Adams, T. *et al.* Long-wavelength helimagnetic order and skyrmion lattice phase in Cu_2OSeO_3 . *Physical Review Letters* **108**, 237204 (2012).
19. Giess, E. A. Magnetic bubble materials. *Science* **208**, 938–943 (1980).
20. Yu, X. *et al.* Magnetic stripes and skyrmions with helicity reversals. *Proceedings of the National Academy of Sciences* **109**, 8856–8860 (2012).
21. Yu, X. Z. *et al.* Biskyrmion states and their current-driven motion in a layered manganite. *Nature Communications* **5** (2014).
22. Heinze, S. *et al.* Spontaneous atomic-scale magnetic skyrmion lattice in two dimensions. *Nature Physics* **7**, 713–718 (2011).
23. Romming, N. *et al.* Writing and deleting single magnetic skyrmions. *Science* **341**, 636–639 (2013).
24. Tokunaga, Y. *et al.* A new class of chiral materials hosting magnetic skyrmions beyond room temperature. *Nature Communications* **6** (2015).
25. Fujishiro, Y., Kanazawa, N. & Tokura, Y. Engineering skyrmions and emergent monopoles in topological spin crystals. *Applied Physics Letters* **116**, 090501 (2020).

26. Qiang, B. W. *et al.* Room temperature magnetic skyrmion in epitaxial thin films of $\text{Fe}_{2-x}\text{Pd}_x\text{Mo}_3\text{N}$ with the filled β -Mn type chiral structure. *Applied Physics Letters* **117**, 142401 (2020).
27. Kézsmárki, I. *et al.* Néel-type skyrmion lattice with confined orientation in the polar magnetic semiconductor GaV_4S_8 . *Nature Materials* **14**, 1116–1122 (2015).
28. Timm, C. Theory of magnetism. Technische Universität Dresden, Institute for Theoretical Physics, 2015.
29. Nolting, W. Quantum theory of magnetism (Springer, Berlin London, 2008).
30. White, R. M. Quantum Theory of Magnetism. 362 pp. (Springer-Verlag GmbH, 2007).
31. Neil W. Ashcroft, N. M. Solid State Physics (Cengage Learning, Inc, 1976).
32. Sechovský, V. in Encyclopedia of Materials: Science and Technology, 5018–5032 (Elsevier, 2001).
33. Hofmann, P. Solid state physics : an introduction (Wiley-VCH, Weinheim, 2008).
34. Blundell, S. Magnetism in Condensed Matter (Oxford University Press, 2001).
35. Nolting, W. Theoretical Physics 3: Electrodynamics (Springer International Publishing, 2016).
36. Dzyaloshinskii, I. A thermodynamic theory of weak ferromagnetism of antiferromagnetics. *Journal of Physics and Chemistry of Solids* **4**, 241–255 (1958).
37. Moriya, T. Anisotropic superexchange interaction and weak ferromagnetism. *Physical Review* **120**, 91–98 (1960).
38. Khomskii, D. I. Transition Metal Compounds (Cambridge University Press, 2015).
39. Cheong, S.-W. & Mostovoy, M. Multiferroics: a magnetic twist for ferroelectricity. *Nature Materials* **6**, 13–20 (2007).

40. Rohart, S., Miltat, J. & Thiaville, A. Path to collapse for an isolated Néel skyrmion. *Physical Review B* **93**, 214412 (2016).
41. Fert, A., Reyren, N. & Cros, V. Magnetic skyrmions: advances in physics and potential applications. *Nature Reviews Materials* **2** (2017).
42. Göbel, B., Mertig, I. & Tretiakov, O. A. Beyond skyrmions: Review and perspectives of alternative magnetic quasiparticles. *Physics Reports* **895**, 1–28 (2021).
43. Metalidis, G. Electronic transport in mesoscopic systems. PhD thesis (Universitaet Halle, 2007).
44. Bruno, P., Dugaev, V. K. & Taillefer, M. Topological Hall Effect and Berry phase in magnetic nanostructures. *Physical Review Letters* **93**, 096806 (2004).
45. Ye, J. *et al.* Berry Phase Theory of the Anomalous Hall Effect: Application to Colossal Magnetoresistance Manganites. *Physical Review Letters* **83**, 3737–3740 (1999).
46. Berry, M. V. Quantal phase factors accompanying adiabatic changes. *Proceedings of the Royal Society of London. A. Mathematical and Physical Sciences* **392**, 45–57 (1984).
47. Neubauer, A. *et al.* Topological Hall Effect in the A phase of MnSi. *Physical Review Letters* **102**, 186602 (2009).
48. Raju, M. *et al.* Colossal topological Hall effect at the transition between isolated and lattice-phase interfacial skyrmions. *Nature Communications* **12** (2021).
49. Kurumaji, T. *et al.* Skyrmion lattice with a giant topological Hall effect in a frustrated triangular lattice magnet. *Science* **365**, 914–918 (2019).
50. Chen, J. *et al.* Evidence for Magnetic Skyrmions at the Interface of Ferromagnet - Topological Insulator Heterostructures. *Nano Letters* (2019).
51. Jiang, W. *et al.* Direct observation of the skyrmion Hall effect. *Nature Physics* **13**, 162–169 (2016).

52. Juge, R. *et al.* Current-Driven Skyrmion Dynamics and Drive-Dependent Skyrmion Hall Effect in an Ultrathin Film. *Physical Review Applied* **12**, 044007 (2019).
53. Rao, C. N. R. Transition metal oxides. *Annual Review of Physical Chemistry* **40**, 291–326 (1989).
54. Imada, M., Fujimori, A. & Tokura, Y. Metal-insulator transitions. *Reviews of Modern Physics* **70**, 1039–1263 (1998).
55. Tokura, Y. & Nagaosa, N. Orbital Physics in Transition-Metal Oxides. *Science* **288**, 462–468 (2000).
56. Shimamoto, K. *et al.* Tuning the multiferroic mechanisms of TbMnO₃ by epitaxial strain. *Scientific Reports* **7** (2017).
57. Bertinshaw, J. *et al.* Direct evidence for spin cycloid in strained nanoscale BiFeO₃ thin films. *Nature Communications* **7** (2016).
58. Matsubara, M. *et al.* Magneto-electric domain control in the multiferroic TbMnO₃. *Science* **348**, 1112–1115 (2015).
59. Bertinshaw, J. *et al.* Element-specific depth profile of magnetism and stoichiometry at the La_{0.67}Sr_{0.33}MnO₃/BiFeO₃ interface. *Physical Review B* **90**, 041113 (2014).
60. Khomskii, D. Classifying multiferroics: Mechanisms and effects. *Physics* **2**, 20 (2009).
61. Abe, N. *et al.* Polarization reversal in multiferroic TbMnO₃ with a rotating magnetic field direction. *Physical Review Letters* **99**, 227206 (2007).
62. Ramesh, R. & Spaldin, N. A. Multiferroics: progress and prospects in thin films. *Nature Materials* **6**, 21–29 (2007).
63. Scott, J. F. Multiferroic memories. *Nature Materials* **6**, 256–257 (2007).
64. Fiebig, M., Lottermoser, T., Meier, D. & Trassin, M. The evolution of multiferroics. *Nature Reviews Materials* **1** (2016).
65. Kang, W., Huang, Y., Zhang, X., Zhou, Y. & Zhao, W. Skyrmion-electronics: an overview and outlook. *Proceedings of the IEEE* **104**, 2040–2061 (2016).

66. Seki, S., Ishiwata, S. & Tokura, Y. Magnetolectric nature of skyrmions in a chiral magnetic insulator Cu_2OSeO_3 . *Physical Review B* **86** (2012).
67. Ruff, E., Lunkenheimer, P., Loidl, A., Berger, H. & Krohns, S. Magnetolectric effects in the skyrmion host material Cu_2SeO_4 . *Scientific Reports* **5**, 15025 (2015).
68. Hahn, T. International tables for crystallography (Published for the International Union of Crystallography by D. Reidel Pub. Co, Dordrecht, Holland Boston, 1983).
69. Momma, K. & Izumi, F. VESTA 3 for three-dimensional visualization of crystal, volumetric and morphology data. *Journal of Applied Crystallography* **44**, 1272–1276 (2011).
70. Meunier, G. & Bertaud, M. Constantes cristallographiques de CuSe_2O_5 , CuSeO_3 et Cu_2SeO_4 . *Journal of Applied Crystallography* **9**, 364–366 (1976).
71. Effenberger, H. & Pertlik, F. Die Kristallstrukturen der Kupfer(II) oxoselenite $\text{Cu}_2\text{O}(\text{SeO}_3)$ (kubisch und monoklin) und $\text{Cu}_4\text{O}(\text{SeO}_3)_3$ (monoklin und triklin). *Monatshefte für Chemie Chemical Monthly* **117**, 887–896 (1986).
72. Bos, J.-W. G., Colin, C. V. & Palstra, T. T. M. Magnetolectric coupling in the cubic ferrimagnet Cu_2OSeO_3 . *Physical Review B* **78**, 094416 (2008).
73. Kohn, K. A New Ferrimagnet Cu_2SeO_4 . *Journal of the Physical Society of Japan* **42**, 2065–2066 (1977).
74. Petford-Long, A. K. & Chapman, J. N. in *Magnetic Microscopy of Nanostructures* (eds Hopster, H. & Oepen, H. P.) 67–86 (Springer Berlin Heidelberg, Berlin, Heidelberg, 2005).
75. Bajt, S. *et al.* Quantitative phase-sensitive imaging in a transmission electron microscope. *Ultramicroscopy* **83**, 67–73 (2000).
76. Han, M.-G. *et al.* Scaling, rotation, and channeling behavior of helical and skyrmion spin textures in thin films of Te-doped Cu_2OSeO_3 . *Science Advances* **6**, eaax2138 (2020).

77. Qian, F. *et al.* New magnetic phase of the chiral skyrmion material Cu_2OSeO_3 . *Science Advances* **4**, eaat7323 (2018).
78. Chacon, A. *et al.* Observation of two independent skyrmion phases in a chiral magnetic material. *Nature Physics* **14**, 936–941 (2018).
79. Halder, M. *et al.* Thermodynamic evidence of a second skyrmion lattice phase and tilted conical phase in Cu_2OSeO_3 . *Physical Review B* **98**, 144429 (2018).
80. Bannenberg, L. J. *et al.* Multiple low-temperature skyrmionic states in a bulk chiral magnet. *npj Quantum Materials* **4** (2019).
81. Leonov, A. O. & Pappas, C. Skyrmion clusters and conical droplets in bulk helimagnets with cubic anisotropy. *Physical Review B* **99** (2019).
82. Bogdanov, A. N. & Yablonskii, D. A. Thermodynamically stable “vortices” in magnetically ordered crystals. The mixed state of magnets. *Zhurnal Eksperimentalnoi I Teoreticheskoi Fiziki* **95**, 178–182 (1989).
83. Janoschek, M. *et al.* Fluctuation-induced first-order phase transition in Dzyaloshinskii-Moriya helimagnets. *Physical Review B* **87**, 134407 (2013).
84. Desplat, L., Suess, D., Kim, J.-V. & Stamps, R. L. Thermal stability of metastable magnetic skyrmions: Entropic narrowing and significance of internal eigenmodes. *Physical Review B* **98**, 134407 (2018).
85. Oike, H. *et al.* Interplay between topological and thermodynamic stability in a metastable magnetic skyrmion lattice. *Nature Physics* **12**, 62–66 (2015).
86. Muckel, F. *et al.* Experimental identification of two distinct skyrmion collapse mechanisms. *Nature Physics* **17**, 395–402 (2021).
87. Legrand, W. *et al.* Room temperature stabilization of AFM skyrmions in synthetic antiferromagnets. *Nature Materials* **19**, 34–42 (2019).
88. Abanov, A. & Pokrovsky, V. L. Skyrmion in a real magnetic film. *Physical Review B* **58**, R8889–R8892 (1998).
89. Cai, L., Chudnovsky, E. M. & Garanin, D. A. Collapse of skyrmions in 2D ferromagnets and antiferromagnets. *Physical Review B* **86**, 024429 (2012).

90. Khomskii, D. I. *Basic Aspects of the Quantum Theory of Solids: Order and Elementary Excitations* (Cambridge University Press, 2010).
91. Bak, P. & Jensen, M. H. Theory of helical magnetic structures and phase transitions in MnSi and FeGe. *Journal of Physics C: Solid State Physics* **13**, L881–L885 (1980).
92. Nakanishi, O., Yanase, A., Hasegawa, A. & Kataoka, M. The origin of the helical spin density wave in MnSi. *Solid State Communications* **35**, 995–998 (1980).
93. Thessieu, C., Pfleiderer, C., Stepanov, A. N. & Flouquet, J. Field dependence of the magnetic quantum phase transition in MnSi. *Journal of Physics: Condensed Matter* **9**, 6677–6687 (1997).
94. Pfleiderer, C. Why first order quantum phase transitions are interesting. *Journal of Physics: Condensed Matter* **17**, S987–S997 (2005).
95. Huang, P. *et al.* Melting of a skyrmion lattice to a skyrmion liquid via a hexatic phase. *Nature Nanotechnology* **15**, 761–767 (2020).
96. Kosterlitz, J. M. & Thouless, D. J. Ordering, metastability and phase transitions in two-dimensional systems. *Journal of Physics C: Solid State Physics* **6**, 1181–1203 (1973).
97. Halperin, B. I. & Nelson, D. R. Theory of Two-Dimensional Melting. *Physical Review Letters* **41**, 121–124 (1978).
98. Nelson, D. R. & Halperin, B. I. Dislocation-mediated melting in two dimensions. *Physical Review B* **19**, 2457–2484 (1979).
99. Young, A. P. Melting and the vector Coulomb gas in two dimensions. *Physical Review B* **19**, 1855–1866 (1979).
100. Seagate. HAMR: the Next Leap Forward is Now. <https://blog.seagate.com/craftsman-ship/hamr-next-leap-forward-now/>.
101. Fert, A., Cros, V. & Sampaio, J. Skyrmions on the track. *Nature Nanotechnology* **8**, 152–156 (2013).

102. Göbel, B., Schäffer, A. F., Berakdar, J., Mertig, I. & Parkin, S. S. P. Electrical writing, deleting, reading, and moving of magnetic skyrmioniums in a racetrack device. *Scientific Reports* **9** (2019).
103. Sampaio, J., Cros, V., Rohart, S., Thiaville, A. & Fert, A. Nucleation, stability and current-induced motion of isolated magnetic skyrmions in nanostructures. *Nature Nanotechnology* **8**, 839–844 (2013).
104. Parkin, S. S. P., Hayashi, M. & Thomas, L. Magnetic Domain-Wall Racetrack Memory. *Science* **320**, 190–194 (2008).
105. Psaroudaki, C. & Panagopoulos, C. Skyrmion Qubits: A New Class of Quantum Logic Elements Based on Nanoscale Magnetization. *Physical Review Letters* **127**, 067201 (2021).
106. Binnewies, M., Glaum, R., Schmidt, M. & Schmidt, P. Chemical Vapor Transport Reactions - A Historical Review. *Zeitschrift für anorganische und allgemeine Chemie* **639**, 219–229 (2013).
107. Kumar, N., Guin, S. N., Manna, K., Shekhar, C. & Felser, C. Topological quantum materials from the viewpoint of chemistry. *Chemical Reviews* **121**, 2780–2815 (2020).
108. Aqeel, A. *et al.* Growth and Helicity of Noncentrosymmetric Cu_2OSeO_3 Crystals, 2100152 (2021).
109. Panella, J. R., Trump, B. A., Marcus, G. G. & McQueen, T. M. Seeded chemical vapor transport growth of Cu_2OSeO_3 . *Crystal Growth & Design* **17**, 4944–4948 (2017).
110. Ealdama-Camacho, L. M. A novel study on the characterisation and structure of multiferroics: the renaissance of magnetism. BA thesis (University of Auckland, 2017).
111. Ouladdiaf, B. *et al.* OrientExpress: A new system for Laue neutron diffraction. *Physica B: Condensed Matter* **385-386**, 1052–1054 (2006).
112. Ibach, H. Solid state physics: an introduction to theory and experiment (Springer, Berlin, Heidelberg, 1991).
113. J. R. Hook, H. E. H. Solid State Physics (Wiley, 1995).

114. Kittel, C. *Introduction to Solid State Physics* (Wiley, 2004).
115. Siegfried Hunklinger, C. E. *Solid State Physics* (Gruyter, Walter de GmbH, 2021).
116. Kuzmany, H. *Solid-State Spectroscopy* (Springer-Verlag GmbH, 2009).
117. Rutherford, E. Bakerian Lecture: Nuclear constitution of atoms. *Proceedings of the Royal Society of London. Series A, Containing Papers of a Mathematical and Physical Character* **97**, 374–400 (1920).
118. Rutherford, E. & Chadwick, J. Energy Relations in Artificial Disintegration. *Mathematical Proceedings of the Cambridge Philosophical Society* **25**, 186–192 (1929).
119. Chadwick, J., Constable, J. E. R. & Pollard, E. C. Artificial Disintegration by α -Particles. *Proceedings of the Royal Society of London. Series A, Containing Papers of a Mathematical and Physical Character* **130**, 463–489 (1931).
120. Institut Laue-Langevin. Neutron data booklet (eds Dianoux, A. J. & Lander, G.) (Old City Publishing Group, 2003).
121. Cameron, I. R. *Nuclear fission reactors* (Plenum Press, New York, 1982).
122. Squires, G. L. *Introduction to the Theory of Thermal Neutron Scattering* (Cambridge University Press, 2012).
123. Karl-Heinrich Beckurts, K. W. *Neutron Physics* (Springer Berlin Heidelberg, 2013).
124. Manning, G. Spallation neutron sources for neutron beam research. *Contemporary Physics* **19**, 505–529 (1978).
125. Carpenter, J. M. Pulsed spallation neutron sources for slow neutron scattering. *Nuclear Instruments and Methods* **145**, 91–113 (1977).
126. Knoll, G. F. *Radiation Detection and Measurement* (Wiley, 2010).
127. *Treatise on Heavy-Ion Science* (ed Bromley, D. A.) (Springer US, 2012).
128. Thomson, J. J. & Rutherford, E. XL. On the passage of electricity through gases exposed to Röntgen rays. *Philosophical Magazine* **42**, 392–407 (1896).

129. Kopp, M. K., Valentine, K. H., Christophorou, L. G. & Carter, J. G. New gas mixture improves performance of ^3He neutron counters. *Nuclear Instruments and Methods in Physics Research* **201**, 395–401 (1982).
130. Anger, H. O. Scintillation Camera. *Review of Scientific Instruments* **29**, 27–33 (1958).
131. Rausch, C., Dietze, M., Felber, J., Hofmann, J. & Schillinger, B. Position sensitive detectors for thermal neutrons using image intensifiers, CCDs and image plates. *Journal of Neutron Research* **3**, 171–191 (1996).
132. Cheng, Y. T., Mildner, D. F. R., Chen-Mayer, H. H., Sharov, V. A. & Glinka, C. J. An imaging-plate detector for small-angle neutron scattering. *Journal of Applied Crystallography* **33**, 1253–1261 (2000).
133. Van Eijk, C. W. E. Inorganic-scintillator development. *Nuclear Instruments and Methods in Physics Research Section A: Accelerators, Spectrometers, Detectors and Associated Equipment* **460**, 1–14 (2001).
134. Nunes, A. C. The converging-beam small-angle neutron diffractometer: calculated resolution. *Journal of Applied Crystallography* **11**, 460–464 (1978).
135. Glinka, C. J., Rowe, J. M. & LaRock, J. G. The small-angle neutron scattering spectrometer at the National Bureau of Standards. *Journal of Applied Crystallography* **19**, 427–439 (1986).
136. Wright, A. F., Berneron, M. & Heathman, S. P. Radial collimator system for reducing background noise during neutron diffraction with area detectors. *Nuclear Instruments and Methods* **180**, 655–658 (1981).
137. Bonse, U. & Hart, M. Tailless X-ray single-crystal reflection curves obtained by multiple reflection. *Applied Physics Letters* **7**, 238–240 (1965).
138. Zachariasen, W. *Theory of X-ray diffraction in crystals* (Dover Publications, Mineola, N.Y., 2004).
139. Maier-Leibnitz, H. Early neutron optics in Munich and in Grenoble. *Physica B+C* **151**, 3–6 (1988).

140. Freund, A. K. Cross-sections of materials used as neutron monochromators and filters. *Nuclear Instruments and Methods in Physics Research* **213**, 495–501 (1983).
141. Shapiro, S. M. & Chesser, N. J. Characteristics of pyrolytic graphite as an analyzer and higher order filter in neutron scattering experiments. *Nuclear Instruments and Methods* **101**, 183–186 (1972).
142. Lu, J., Sabharwall, P., Heidrich, B. & Christensen, R. Advanced Manufacturing and Instrumentation for Neutron Chopper Design. Tech. rep. (2020).
143. Ehlers, G., Podlesnyak, A. A. & Kolesnikov, A. I. The cold neutron chopper spectrometer at the Spallation Neutron Source – A review of the first 8 years of operation. *Review of Scientific Instruments* **87**, 093902 (2016).
144. Wagner, V., Friedrich, H. & Wille, P. Performance of a high-tech neutron velocity selector. *Physica B: Condensed Matter* **180-181**, 938–940 (1992).
145. Dash, J. G. & Sommers, H. S. A High Transmission Slow Neutron Velocity Selector. *Review of Scientific Instruments* **24**, 91–96 (1953).
146. Pynn, R. in *Yearbook of Science and Technology*, 252 (McGraw-Hill, 2009).
147. Lonsdale, K. Neutron diffraction by crystals. *Nature* **164**, 205–209 (1949).
148. Shull, C. G. & Smart, J. S. Detection of Antiferromagnetism by Neutron Diffraction. *Physical Review* **76**, 1256–1257 (1949).
149. Low, G. G. Investigation of magnetic structure and dynamics in solids with neutron beams. *Nature* **219**, 895–899 (1968).
150. Vaknin, D. *et al.* Antiferromagnetism in La_2CuO_{4-y} . *Physical Review Letters* **58**, 2802–2805 (1987).
151. *Strongly Correlated Systems – Experimental techniques* (eds Avella, A. & Mancini, F.) 302 pp. (Springer-Verlag GmbH, 2014).
152. Ratcliff, W., Lynn, J. W., Kiryukhin, V., Jain, P. & Fitzsimmons, M. R. Magnetic structures and dynamics of multiferroic systems obtained with neutron scattering. *npj Quantum Materials* **1** (2016).
153. Chatterji, T. *Neutron scattering from magnetic materials* (Elsevier, Amsterdam Boston, 2006).

154. Shirane, G., Shapiro, S. M. & Tranquada, J. M. Neutron scattering with a triple-axis spectrometer: basic techniques (Cambridge University Press, Cambridge, 2002).
155. Mühlbauer, S. *et al.* Magnetic small-angle neutron scattering. *Reviews of Modern Physics* **91** (2019).
156. Furrer, A. Neutron scattering. Lecture notes of the first summer school on neutron scattering. 1993.
157. Landau, L. D. Mecánica cuántica, no-relativista (Editorial Reverte, 1983).
158. Sakurai, J. J. Modern quantum mechanics (Addison-Wesley Pub. Co, Reading, Mass, 1994).
159. Merzbacher, E. Quantum Mechanics (John Wiley and Sons, 1997).
160. Shankar, R. Principles of Quantum Mechanics (Springer US, 2011).
161. Hassani, S. Mathematical Physics (Springer-Verlag GmbH, 2013).
162. George B. Arfken, H. J. W. Mathematical Methods for Physicists (Elsevier LTD, Oxford, 2012).
163. Boas, M. L. Mathematical Methods in the Physical Sciences (Wiley, 2005).
164. Szekeres, P. A course in modern mathematical physics: groups, Hilbert space, and differential geometry (Cambridge University Press, Cambridge, UK New York, 2004).
165. Jackson, J. D. Classical Electrodynamics (Wiley, 1998).
166. Griffiths, D. Introduction to electrodynamics (Prentice Hall, Upper Saddle River, N.J, 1999).
167. Reitz, J. Fundamentos de la teoría electromagnética (Prentice Hall Addison Wesley Longman, México, 1999).
168. Landau, L. D. Mechanics (Pergamon Press, Oxford New York, 1976).
169. Goldstein, H. Classical mechanics (Addison Wesley, San Francisco, 2002).
170. Taylor, J. R. Classical Mechanics (Univ Science Books, 2004).
171. Thornton, S. Classical dynamics of particles and systems (Brooks/Cole, Belmont, CA, 2004).

172. Steinsvoll, O. *et al.* Magnetic Form Factor of Terbium. *Physical Review* **161**, 499–506 (1967).
173. Marshall, W. & Lowde, R. D. Magnetic correlations and neutron scattering. *Reports on Progress in Physics* **31**, 705–775 (1968).
174. Marshall, W. & Lovesey, S. W. Theory of thermal neutron scattering : the use of neutrons for the investigation of condensed matter (Clarendon Press, Oxford, 1971).
175. Lovesey, S. W. Theory of neutron scattering from condensed matter (Clarendon Press, Oxford Oxfordshire, 1984).
176. Wood, K. *et al.* QUOKKA, the pinhole small-angle neutron scattering instrument at the OPAL Research Reactor, Australia: design, performance, operation and scientific highlights. *Journal of Applied Crystallography* **51**, 294–314 (2018).
177. Hamilton, W. A., Garrett, R. & Gilbert, E. P. Quokka: The Small-Angle Neutron Scattering Instrument. *Neutron News* **20**, 24–28 (2009).
178. Gilbert, E. P., Schulz, J. C. & Noakes, T. J. ‘Quokka’ – the small-angle neutron scattering instrument at OPAL. *Physica B: Condensed Matter* **385-386**, 1180–1182 (2006).
179. Australian Centre for Neutron Scattering. Sample environment equipment handbook. https://www.ansto.gov.au/sites/default/files/2021-01/se_manual_06_01_21-compressed.pdf.
180. Heer, H., Könnecke, M. & Maden, D. The SINQ instrument control software system. *Physica B: Condensed Matter* **241-243**, 124–126 (1997).
181. Koranne, S. in *Handbook of Open Source Tools*, 191–200 (Springer US, 2010).
182. Poinot, M. Five Good Reasons to Use the Hierarchical Data Format. *Computing in Science & Engineering* **12**, 84–90 (2010).
183. Habermann, T. & Folk, M. J. The Hierarchical Data Format (HDF): A Foundation for Sustainable Data and Software. in *AGU Fall Meeting Abstracts 2014* (2014), IN21D–07.

184. Lam, T., Götz, A., Franceschini, F. & Hauser, N. GumTree – a Java based GUI framework for beamline experiments. *Journal of Neutron Research* **14**, 167–175 (2006).
185. Lam, T. *et al.* GumTree – An integrated scientific experiment environment. *Physica B: Condensed Matter* **385-386**, 1330–1332 (2006).
186. Kline, S. R. Reduction and analysis of SANS and USANS data using IGOR Pro. *Journal of Applied Crystallography* **39**, 895–900 (2006).
187. WaveMetrics, Inc. 10200 SW Nimbus, G-7 Portland, OR 97223. Reduction and analysis of SANS, VSANS, and USANS data using Igor Pro. <https://www.wavemetrics.com/case-study/small-angle-very-small-and-ultra-small-neutron-scattering>.
188. ANSTO. SANS reduction macros for Igor. <http://www.nbi.ansto.gov.au/quokka/macros/IgorUserFilesSwitch.exe>.
189. ANSTO. QUOKKA User Guide. <https://archive.ansto.gov.au/cs/groups/corporate/documents/document/mdaw/mdm4/~edisp/acs079538.pdf>.
190. Jacob, L. *The solid state: X-ray spectroscopy* (Butterworths, London, 1974).
191. ANSTO. Joey - Neutron Laue Camera. <https://www.ansto.gov.au/our-facilities/facilities/australian-centre-for-neutron-scattering/joey-neutron-laue-camera>.
192. Gatta, G. D., Vignola, P., McIntyre, G. J. & Diella, V. On the crystal chemistry of londonite [(Cs,K,Rb)Al₄Be₅B₁₁O₂₈]: A single-crystal neutron diffraction study at 300 and 20 K. *American Mineralogist* **95**, 1467–1472 (2010).
193. Iles, G. & Schorr, S. The new single-crystal neutron Laue diffractometer in Berlin. in *Proceedings of the 21st Meeting of the International Collaboration on Advanced Neutron Sources* (2016).
194. Klose, F., Constantine, P., Kennedy, S. J. & Robinson, R. A. The Neutron Beam Expansion Program at the Bragg Institute. *Journal of Physics: Conference Series* **528**, 012026 (2014).

195. McIntyre, G. J. & Holden, P. J. Neutron scattering at the OPAL research reactor. *Journal of Physics: Conference Series* **746**, 012001 (2016).
196. National Institutes of Health (NIH). Image Processing and Analysis in Java. <https://imagej.nih.gov/ij/index.html>.
197. Neutron Optics Grenoble. Options for inexpensive x-ray and neutron CCD cameras. <http://www.neutronoptics.com/options.html>.
198. Lake Shore Cryotronics, Inc. Epoxy, grease and varnish. https://indico.fnal.gov/event/11540/contributions/8781/attachments/5872/7606/LSTC_epoxygv_1.pdf.
199. Montana Instruments. Cryogenics sample mounting guide. <https://www.montanainstruments.com/help/Sample-Mounting-Guide/>.
200. CMR-Direct. GE Varnish. <http://www.cmr-direct.com/en/ge-varnish>.
201. Photonic Science. Laue Crystal Orientation System. photonicsscience.com/products/laue-crystal-orientation-system/.
202. Avdeev, M. & Hester, J. R. ECHIDNA: a decade of high-resolution neutron powder diffraction at OPAL. *Journal of Applied Crystallography* **51**, 1597–1604 (2018).
203. Avdeev, M., Hester, J. R., Peterson, V. K. & Studer, A. J. Wombat and Echidna: The Powder Diffractometers. *Neutron News* **20**, 29–33 (2009).
204. Studer, A. J., Hagen, M. E. & Noakes, T. J. Wombat: The high-intensity powder diffractometer at the OPAL reactor. *Physica B: Condensed Matter* **385-386**, 1013–1015 (2006).
205. Auckett, J. E., Studer, A. J., Sharma, N. & Ling, C. D. Floating-zone growth of brownmillerite Sr₂Fe₂O₅ and the observation of a chain-ordered superstructure by single-crystal neutron diffraction. *Solid State Ionics* **225**, 432–436 (2012).
206. Edwards, A. J. Chemical crystallography with neutrons - KOALA capabilities. 2009.
207. Raman, C. V. & Krishnan, K. S. A New Type of Secondary Radiation. *Nature* **121**, 501–502 (1928).

208. Placzek, G. Rayleigh-Streuung und Raman-Effekt. in (1934).
209. Light scattering in solids (ed Cardona, M.) (Springer, 1982).
210. Devereaux, T. P. & Hackl, R. Inelastic light scattering from correlated electrons. *Reviews of Modern Physics* **79**, 175–233 (2007).
211. Campanella, B., Palleschi, V. & Legnaioli, S. Introduction to vibrational spectroscopies. *ChemTexts* **7**, 5 (2021).
212. Um, Y. A Study of Lattice Dynamics in Iron-based Superconductors by Inelastic Light Scattering. PhD thesis (University of Stuttgart, 2013).
213. Cardona, M., Chang, R. K., Güntherodt, G., Long, M. B. & Vogt, H. Light Scattering in Solids II: Basic Concepts and Instrumentation (Topics in Applied Physics) (eds Cardona, M. & Güntherodt, G.) (Springer, 1982).
214. Rahlenbeck, M. Raman light scattering study on phonon anomalies in unconventional superconductors. PhD thesis (Eberhard-Karls-University of Tübingen, 2010).
215. Yu, P. & Cardona, M. Fundamentals of semiconductors Fourth (Springer, 2010).
216. Klemens, P. G. Anharmonic Decay of Optical Phonons. *Physical Review* **148**, 845–848 (1966).
217. Menéndez, J. & Cardona, M. Temperature dependence of the first-order Raman scattering by phonons in Si, Ge, and α -Sn: Anharmonic effects. *Physical Review B* **29**, 2051–2059 (1984).
218. Fano, U. Effects of Configuration Interaction on Intensities and Phase Shifts. *Physical Review* **124**, 1866–1878 (1961).
219. Sigma Aldrich Solutions. Silver conductive paste. eprint: https://www.sigmaaldrich.com/specification-sheets/428/305/735825-BULK_____ALDRICH_.pdf.
220. TechInstro. Silver conductive paste technical specification sheet. eprint: <https://www.techinstro.com/wp-content/uploads/2019/03/Datasheet-Silver-Conductive-Paste-SILVERPASTE.pdf>.

221. Omega. PID & Process Temperature Controllers. <https://au.omega.com/prodinfo/temperaturecontrollers.html>.
222. Jaklevic, R. C., Lambe, J., Mercereau, J. E. & Silver, A. H. Macroscopic Quantum Interference in Superconductors. *Physical Review* **140**, A1628–A1637 (1965).
223. Simmonds, M., Fertig, W. & Giffard, R. Performance of a resonant input SQUID amplifier system. *IEEE Transactions Magnetics* **15**, 478–481 (1979).
224. Buckel, W. Superconductivity: fundamentals and applications (Wiley-VCH John Wiley, Weinheim Chichester, 2004).
225. Buchner, M., Höfler, K., Henne, B., Ney, V. & Ney, A. Tutorial: Basic principles, limits of detection, and pitfalls of highly sensitive SQUID magnetometry for nanomagnetism and spintronics. *Journal of Applied Physics* **124**, 161101 (2018).
226. Degen, C., Reinhard, F. & Cappellaro, P. Quantum sensing. *Reviews of Modern Physics* **89**, 035002 (2017).
227. Qian, F. *et al.* Phase diagram and magnetic relaxation phenomena in Cu_2OSeO_3 . *Physical Review B* **94**, 064418 (2016).
228. Levatić, I., Šurija, V., Berger, H. & Živković, I. Dissipation processes in the insulating skyrmion compound Cu_2OSeO_3 . *Physical Review B* **90**, 224412 (2014).
229. Quantum Design, Inc. <http://www.qdusa.com>.
230. Vergniory, M. G. *et al.* A complete catalogue of high-quality topological materials. *Nature* **566**, 480–485 (2019).
231. Tang, F., Po, H.-C., Vishwanath, A. & Wan, X. Comprehensive search for topological materials using symmetry indicators. *Nature* **566**, 486 (2019).
232. Chiu, C.-K., Teo, J. C. Y., Schnyder, A. P. & Ryu, S. Classification of topological quantum matter with symmetries. *Reviews of Modern Physics* **88**, 035005 (2016).
233. Xiao, J. & Yan, B. First-principles calculations for topological quantum materials. *Nature Reviews Physics* **3**, 283–297 (2021).

234. Everschor-Sitte, K., Masell, J., Reeve, R. M. & Kläui, M. Perspective: Magnetic skyrmions – Overview of recent progress in an active research field. *Journal of Applied Physics* **124**, 240901 (2018).
235. Wang, X.-G. *et al.* The optical tweezer of skyrmions. *npj Computational Materials* **6** (2020).
236. Paul Scherrer Institute. Software package SASfit for fitting small-angle scattering curves. <https://www.psi.ch/en/sinq/sansi/sasfit>.
237. National Institute for Standards and Technology. SasView. <https://www.sasview.org/>.
238. Advanced Photon Source. Irena: Small-Angle Scattering Data Analysis. <https://www.aps.anl.gov/Science/Scientific-Software/Irena>.
239. Irizarry, R. Introduction to Data Science (CRC Press, Boca Raton, 2019).
240. Stormy Attaway, D. C. A. MATLAB: A Practical Introduction to Programming and Problem Solving (Elsevier LTD, Oxford, 2018).
241. Martinez, W. Statistics in MATLAB: a primer (CRC Press, Boca Raton, 2015).
242. Schilling, R. Applied numerical methods for engineers using MATLAB and C (Brooks/Cole, Pacific Grove, CA, 2000).
243. Chapra, S. Applied numerical methods with MATLAB® for engineers and scientists (McGraw-Hill Education, New York, NY, 2018).
244. Burden, R. Numerical analysis (Brooks/Cole, Cengage Learning, Boston, MA, 2011).
245. Alfio Quarteroni, F. S. Scientific Computing with MATLAB and Octave (Springer-Verlag GmbH, 2007).
246. Pedersen, J. S., Posselt, D. & Mortensen, K. Analytical treatment of the resolution function for small-angle scattering. *Journal of Applied Crystallography* **23**, 321–333 (1990).
247. The HDF Group. HDF5 File Format Specification Version 3.0. <https://support.hdfgroup.org/HDF5/doc/H5.format.html>.

248. Hansen, E. *Fourier transforms: principles and applications* (Wiley, Hoboken, New Jersey, 2014).
249. Serov, V. *Fourier Series and Fourier Transform and Their Applications in Mathematical Physics* (Springer-Verlag GmbH, 2018).
250. Rzeszotarski, M. S., Royer, F. L. & Gilmore, G. C. Introduction to two-dimensional Fourier analysis. *Behavior Research Methods & Instrumentation* **15**, 308–318 (1983).
251. Boothroyd, A. T. *Principles of Neutron Scattering from Condensed Matter* (Oxford University Press, 2020).
252. Hirschberger, M. *et al.* Skyrmion phase and competing magnetic orders on a breathing kagomé lattice. *Nature Communications* **10**, 5831 (2019).
253. Zhang, S. L. *et al.* Multidomain Skyrmion Lattice State in Cu_2OSeO_3 . *Nano Letters* **16**, 3285–3291 (2016).
254. Wan, X., Hu, Y., Hou, Z. & Wang, B. Pinning effects of exchange and magnetocrystalline anisotropies on skyrmion lattice. *Frontiers in Physics* **9** (2021).
255. White, J. S. *et al.* Electric-Field-Driven Topological Phase Switching and Skyrmion-Lattice Metastability in Magnetoelectric Cu_2OSeO_3 . *Physical Review Applied* **10**, 014021 (2018).
256. Adams, T. *et al.* Long-range crystalline nature of the skyrmion lattice in MnSi. *Physical Review Letters* **107**, 217206 (2011).
257. Hammouda, B. Are Bragg peaks Gaussian? *Journal of Research of the National Institute of Standards and Technology* **119**, 15 (2014).
258. Tengdin, P. *et al.* Imaging the controllable rotation of a skyrmion crystal driven by femtosecond laser pulses. arXiv: 2110.04548 [cond-mat.str-el] (2021).
259. Hirosawa, T., Klinovaja, J., Loss, D. & Diaz, S. A. Laser-controlled real- and reciprocal-space topology in multiferroic insulators. arXiv: 2108.06535 [cond-mat.str-el] (2021).

260. Berruto, G. *et al.* Laser-induced skyrmion writing and erasing in an ultrafast cryo-Lorentz Transmission Electron Microscope. *Physical Review Letters* **120**, 117201 (2018).
261. Je, S.-G. *et al.* Creation of magnetic skyrmion bubble lattices by ultrafast laser in ultrathin films. *Nano Letters* **18**, 7362–7371 (2018).
262. Stepanov, E. A., Dutreix, C. & Katsnelson, M. I. Dynamical and reversible control of topological spin textures. *Physical Review Letters* **118**, 157201 (2017).
263. Ogawa, N., Seki, S. & Tokura, Y. Ultrafast optical excitation of magnetic skyrmions. *Scientific Reports* **5** (2015).
264. Finazzi, M. *et al.* Laser-induced magnetic nanostructures with tunable topological properties. *Physical Review Letters* **110**, 177205 (2013).
265. Winkler, T. B. *et al.* Skyrmion states in disk geometry. **16**, 044014 (2021).
266. Ba, Y. *et al.* Electric-field control of skyrmions in multiferroic heterostructure via magnetoelectric coupling. *Nature Communications* **12** (2021).
267. Wang, W. *et al.* Electrical manipulation of skyrmions in a chiral magnet. arXiv: 2108.06755 [cond-mat.mes-hall] (2021).
268. Huang, P. *et al.* In situ Electric Field Skyrmion Creation in Magnetoelectric Cu_2OSeO_3 . *Nano Letters* **18**, 5167–5171 (2018).
269. Kruchkov, A. J. *et al.* Direct electric field control of the skyrmion phase in a magnetoelectric insulator. *Scientific Reports* **8**, 10466 (2018).
270. Zhang, S. L. *et al.* Manipulation of skyrmion motion by magnetic field gradients. *Nature Communications* **9**, 2115 (2018).
271. Okamura, Y., Kagawa, F., Seki, S. & Tokura, Y. Transition to and from the skyrmion lattice phase by electric fields in a magnetoelectric compound. *Nature Communications* **7**, 12669 (2016).
272. White, J. *et al.* Electric-Field-Induced Skyrmion Distortion and Giant Lattice Rotation in the Magnetoelectric Insulator Cu_2OSeO_3 . *Physical Review Letters* **113**, 107203 (2014).

273. White, J. S. *et al.* Electric field control of the skyrmion lattice in Cu_2OSeO_3 . *Journal of Physics: Condensed Matter* **24**, 432201 (2012).
274. Khan, S. *et al.* Coupling microwave photons to topological spin textures in Cu_2OSeO_3 . *Physical Review B* **104**, 1100402 (2021).
275. Aqeel, A. *et al.* Microwave Spectroscopy of the Low-Temperature Skyrmion State in Cu_2OSeO_3 . *Physical Review Letters* **126**, 017202 (2021).
276. Okamura, Y. *et al.* Microwave magnetoelectric effect via skyrmion resonance modes in a helimagnetic multiferroic. *Nature Communications* **4**, 2391 (2013).
277. Wang, Y., Liu, Y. & Wang, B. Effects of light on quantum phases and topological properties of two-dimensional metal-organic frameworks. *Scientific Reports* **7**, 41644 (2017).
278. Owerre, S. A. Photoinduced topological phase transitions in topological magnon insulators. *Scientific Reports* **8**, 4431 (2018).
279. Birch, J. R. The absolute determination of complex reflectivity. *Infrared Physics* **18**, 613–620 (1978).
280. Oriel product training: Spectral irradiance. https://www.newport.com/medias/sys_master/images/images/hfb/hdf/8797196451870/Light-Sources.pdf.
281. Yoder, P. R. *Mounting Lenses in Optical Instruments* (SPIE, 1995).
282. Edmund Optics Inc. Optical filters. <https://www.edmundoptics.com.au/knowledge-center/application-notes/optics/optical-filters>.
283. Fastie, W. G. A Small Plane Grating Monochromator. *Journal of the Optical Society of America* **42**, 641 (1952).
284. Strong, J. Resolving Power Limitations of Grating and Prism Spectrometers. *Journal of the Optical Society of America* **39**, 320 (1949).
285. Keck, D. B., Schultz, P. C. & Zimar, F. Attenuation of multimode glass optical waveguides. *Applied Physics Letters* **21**, 215–217 (1972).
286. Kapron, F. P., Keck, D. B. & Maurer, R. D. Radiation losses in glass optical waveguides. *Applied Physics Letters* **17**, 423–425 (1970).

287. Cheng, O. H.-C., Son, D. H. & Sheldon, M. Light-induced magnetism in plasmonic gold nanoparticles. *Nature Photonics* **14**, 365–368 (2020).
288. Brinzari, T. V. *et al.* Light-induced magnetization changes in aggregated and isolated cobalt ferrite nanoparticles. *Journal of Applied Physics* **124**, 103904 (2018).
289. Ohkoshi, S.-i. *et al.* 90-degree optical switching of output second-harmonic light in chiral photomagnet. *Nature Photonics* **8**, 65–71 (2013).
290. Culp, J. T. *et al.* Magnetism of metal cyanide networks assembled at interfaces. *Coordination Chemistry Reviews* **249**, 2642–2648 (2005).
291. O'Connor, C. J. in *Molecular Magnetism: From Molecular Assemblies to the Devices*, 521–552 (Springer Netherlands, 1996).
292. Vakili, H. *et al.* Skyrmionics—computing and memory technologies based on topological excitations in magnets. *Journal of Applied Physics* **130**, 070908 (2021).
293. Demkov, A. A., Bajaj, C., Ekerdt, J. G., Palmstrøm, C. J. & Yoo, S. J. B. Materials for emergent silicon-integrated optical computing. *Journal of Applied Physics* **130**, 070907 (2021).
294. Yu, X. *et al.* Real-space observations of 60-nm skyrmion dynamics in an insulating magnet under low heat flow. *Nature Communications* **12**, 5079 (2021).
295. Sato, T., Takagi, S., Deledda, S., Hauback, B. C. & Orimo, S.-i. Extending the applicability of the Goldschmidt tolerance factor to arbitrary ionic compounds. *Scientific Reports* **6**, 23592 (2016).
296. Goldschmidt, V. M. Die Gesetze der Krystallochemie. *Naturwissenschaften* **14**, 477–485 (1926).
297. Berenov, A., Goupil, F. L. & Alford, N. Effect of ionic radii on the Curie temperature in $\text{Ba}_{1-x-y}\text{Sr}_x\text{Ca}_y\text{TiO}_3$ compounds. *Scientific Reports* **6**, 28055 (2016).

298. Wang, M. *et al.* Doping dependence of spin excitations and its correlations with high-temperature superconductivity in iron pnictides. *Nature Communications* **4**, 2874 (2013).
299. Park, P. *et al.* Spin texture induced by non-magnetic doping and spin dynamics in 2D triangular lattice antiferromagnet h-Y(Mn,Al)O₃. *Nature Communications* **12**, 2306 (2021).
300. Li, W., Qian, X. & Li, J. Phase transitions in 2D materials. *Nature Reviews Materials* **6**, 829–846 (2021).
301. Moody, S. H. *et al.* Experimental evidence of a change of exchange anisotropy sign with temperature in Zn-substituted Cu₂OSeO₃. arXiv: 2105.09273 [cond-mat.str-el] (2021).
302. Birch, M. T. *et al.* Anisotropy-induced depinning in the Zn-substituted skyrmion host Cu₂OSeO₃. *Physical Review B* **102**, 104424 (2020).
303. Birch, M. T. *et al.* Increased lifetime of metastable skyrmions by controlled doping. *Physical Review B* **100**, 014425 (2019).
304. Wilson, M. N. *et al.* Measuring the formation energy barrier of skyrmions in zinc-substituted Cu₂OSeO₃. *Physical Review B* **99**, 174421 (2019).
305. Štefančič, A. *et al.* Origin of skyrmion lattice phase splitting in Zn-substituted Cu₂OSeO₃. *Physical Review Materials* **2**, 111402 (2018).
306. Wu, H. C. *et al.* Unexpected observation of splitting of skyrmion phase in Zn doped Cu₂OSeO₃. *Scientific Reports* **5** (2015).
307. Crisanti, M. *et al.* Position-dependent stability and lifetime of the skyrmion state in nickel-substituted Cu₂OSeO₃. *Physical Review B* **102**, 224407 (2020).
308. Sukhanov, A. S. *et al.* Increasing skyrmion stability in Cu₂OSeO₃ by chemical substitution. *Physical Review B* **100**, 184408 (2019).
309. Wilson, M. N. *et al.* Stability and metastability of skyrmions in thin lamellae of Cu₂OSeO₃. *Physical Review Research* **2**, 013096 (2020).
310. Neves, P. M. *et al.* Effect of chemical substitution on the skyrmion phase in Cu₂OSeO₃. **102**, 134410 (2020).

311. Makino, K. *et al.* Thermal stability and irreversibility of skyrmion-lattice phases in Cu₂OSeO₃. *Physical Review B* **95**, 134412 (2017).
312. Reim, J. D. *et al.* Impact of minute-time-scale kinetics on the stabilization of the skyrmion lattice in Cu₂OSeO₃. *Journal of Physics: Conference Series* **828**, 012004 (2017).
313. Nakajima, T. *et al.* Skyrmion lattice structural transition in MnSi. *Science Advances* **3**, e1602562 (2017).
314. Birch, M. T. *et al.* Topological defect-mediated skyrmion annihilation in three dimensions. *Communications Physics* **4** (2021).
315. Esposito, V. *et al.* Skyrmion fluctuations at a first-order phase transition boundary. **116**, 181901 (2020).
316. Johnston, D. C. Stretched exponential relaxation arising from a continuous sum of exponential decays. *Physical Review B* **74**, 184430 (2006).
317. Hill, R. M. & Dissado, L. A. Debye and non-Debye relaxation. *Journal of Physics C: Solid State Physics* **18**, 3829–3836 (1985).
318. Havriliak, S. & Havriliak, S. J. Comparison of the Havriliak-Negami and stretched exponential functions. *Polymer* **37**, 4107–4110 (1996).
319. Zorn, R. Logarithmic moments of relaxation time distributions. *The Journal of Chemical Physics* **116**, 3204–3209 (2002).
320. Rosa, C. F. A. E. & Capelas de Oliveira, E. Relaxation Equations: Fractional Models. *Journal of Physical Mathematics* **06** (2015).
321. Górska, K., Horzela, A., Bratek, Ł., Dattoli, G. & Penson, K. A. The Havriliak-Negami relaxation and its relatives: the response, relaxation and probability density functions. *Journal of Physics A: Mathematical and Theoretical* **51**, 135202 (2018).
322. Zhang, S. *et al.* Reciprocal space tomography of 3D skyrmion lattice order in a chiral magnet. *Proceedings of the National Academy of Sciences* **115**, 6386–6391 (2018).
323. Hicken, T. J. *et al.* Megahertz dynamics in skyrmion systems probed with muon-spin relaxation. *Physical Review B* **103**, 024428 (2021).

324. Aquilanti, V., Coutinho, N. D. & Carvalho-Silva, V. H. Kinetics of low temperature transitions and a reaction rate theory from non-equilibrium distributions. *Philosophical Transactions of the Royal Society A: Mathematical, Physical and Engineering Sciences* **375**, 20160201 (2017).
325. Piskulich, Z. A., Mesele, O. O. & Thompson, W. H. Activation energies and beyond. *The Journal of Physical Chemistry A* **123**, 7185–7194 (2019).
326. Janson, O. *et al.* The quantum nature of skyrmions and half-skyrmions in Cu_2OSeO_3 . *Nature Communications* **5**, 5376 (2014).
327. Mohanta, N., Christianson, A. D., Okamoto, S. & Dagotto, E. Signatures of a liquid-crystal transition in spin-wave excitations of skyrmions. **3**, 229 (2020).
328. Gnezdilov, V. P. *et al.* Magnetoelectricity in the ferrimagnetic Cu_2SeO_4 : symmetry analysis and Raman scattering study. *Low Temperature Physics* **36**, 550–557 (2010).
329. Versteeg, R. B. Optically probed order and dynamics in the chiral cluster magnet Cu_2OSeO_3 . PhD thesis (Universität zu Köln, 2019).
330. Fleury, P. A. & Loudon, R. Scattering of light by one- and two-magnon excitations. **166**, 514–530 (1968).
331. Versteeg, R. B. *et al.* A tunable time resolved spontaneous Raman spectroscopy setup for probing ultrafast collective excitation and quasiparticle dynamics in quantum materials. *Structural Dynamics* **5**, 044301 (2018).
332. Luo, Y. *et al.* Low-energy magnons in the chiral ferrimagnet Cu_2OSeO_3 : A coarse-grained approach. *Physical Review B* **101**, 144411 (2020).
333. Portnichenko, P. Y. *et al.* Magnon spectrum of the helimagnetic insulator Cu_2OSeO_3 . *Nature Communications* **7** (2016).
334. Tucker, G. S. *et al.* Spin excitations in the skyrmion host Cu_2OSeO_3 . *Physical Review B* **93**, 054401 (2016).
335. Romhányi, J., van den Brink, J. & Rousochatzakis, I. Entangled tetrahedron ground state and excitations of the magnetoelectric skyrmion material Cu_2OSeO_3 . *Physical Review B* **90**, 140404 (2014).

336. Gretarsson, H. *et al.* Raman scattering study of vibrational and magnetic excitations in $\text{Sr}_{2-x}\text{La}_x\text{IrO}_4$. *Physical Review Letters* **96**, 115138 (2017).
337. Miller, K. H. *et al.* Magnetodielectric coupling of infrared phonons in single crystal Cu_2OSeO_3 . *Physical Review B* **82**, 144107 (2010).
338. Pal, S. *et al.* Tuning the structure of the skyrmion lattice system Cu_2OSeO_3 under pressure. *Physical Review B* **102**, 214107 (2020).